DISS. ETH NO. 27495

ELECTRICAL STIMULATION AND FUNCTIONAL
CHARACTERIZATION OF NEURONS USING HIGH-DENSITY
MICROELECTRODE ARRAYS

A thesis submitted to attain the degree of

DOCTOR OF SCIENCES of ETH ZURICH

(Dr. sc. ETH Zurich)

Presented by

SILVIA RONCHI

Laurea Magistrale in Ingegneria Biomedica,

Università degli studi di Roma La Sapienza

born on 09.06.1992

citizen of Italy

accepted on the recommendation of

Prof. Dr. Andreas Hierlemann

Prof. Dr. Ulrich Egert

Dr. Michele Fiscella

2021

CONTENTS

ABSTRACT

This thesis presents a comprehensive collection and analysis of multiple electrophysiology experiments using high-density microelectrode arrays (HD-MEAs). The motivation of this work was to explore the advantages, offered by high-resolution extracellular electrophysiology, and the use of HD-MEAs in the fields of (i) single-cell electrical stimulation, (ii) phenotype characterization of healthy and diseased cell lines and (iii) neural stem-cell maturation.

Compared to other state-of-the-art electrophysiology techniques, such as patch clamp, calcium imaging or the use of genetically-encoded voltage indicators, microelectrode arrays allow for long-term, non-invasive and non-phototoxic monitoring of single cells and entire neuronal networks. Additionally, the recent integration of microelectrode arrays in CMOS technology enables the simultaneous recording from thousands of closely-spaced electrodes so that action potentials of even subcellular compartments of neurons can be monitored. Moreover, new HD-MEA applications, such as single-cell electrical stimulation and detailed action-potential waveform and action-potential propagation analysis, became possible.

After an introduction (Chapter 1), this thesis presents new, optimized ways to perform single-neuron stimulation, relying on the 17.5 μm electrode center-to-center distance. This small electrode-to-electrode distance enables to find the most effective stimulation locations of the targeted neurons and to select low-amplitude and efficient stimulation waveforms, while reducing the stimulation artifact. In Chapter 2, multiple stimulus waveforms, durations and amplitudes were analyzed for both, voltage- and current-stimulation modes. The axon initial segment was demonstrated to be the most effective stimulation site and its maturation in culture over time correlated with a decrease of the stimulation amplitude that was necessary to elicit an action potential.

Chapters 3 and 4 of the thesis include two studies that present new electrophysiological parameters or metrics that can be used to assess phenotypes and maturation states of different cell lines and to analyze compound effects. To date, electrophysiological differences and drug effects are still mostly studied by using standard metrics, such as the number of recorded bursts or action potentials, which do not take full advantage of the available high resolution of CMOS-based HD-MEAs.

In Chapter 3, commonly used and new network, single-cell and subcellular electrophysiology parameters and metrics are presented. These metrics were used to successfully characterize and compare different human induced pluripotent-stem-cell (iPSC)-derived dopaminergic and motor neuron lines and the corresponding isogenic disease lines for Parkinson's disease (PD) and amyotrophic lateral sclerosis (ALS). Additionally, the metrics were used to analyze compound-dosage effects with high reproducibility.

In Chapter 4, neural stem cells were differentiated during 2, 4 and 7 months into mature neuronal networks and transferred simultaneously onto HD-MEAs. Additional metrics to the ones presented in Chapter 3, combined with single-cell RNA sequencing, allowed for successful distinction of the three maturation stages (2, 4 and 7 months) at network, single-cell and subcellular levels.

The thesis concludes with an outlook on potential applications of HD-MEAs in the field of high-content drug screening (Chapter 5).

RIASSUNTO

In questa tesi viene presentata un'esaustiva raccolta di vari esperimenti elettrofisiologici che fanno uso di array di microelettrodi ad alta risoluzione (dall'inglese *high-density microelectrode arrays*, HD-MEAs). L'obiettivo di questo lavoro è stato quello di voler esplorare i vantaggi offerti dall'elettrofisiologia extracellulare ad alta risoluzione e l'uso degli HD-MEAs nelle applicazioni di (i) stimolazione di singolo neurone, (ii) caratterizzazione del fenotipo di linee cellulari che presentano o meno una data manipolazione genetica correlata ad una patologia neurologica e (iii) studi sulla maturazione e lo sviluppo *in vitro* di colture cellulari neuronali.

Comparati con altre tecnologie di elettrofisiologia tipiche dello stato dell'arte, come il patch clamp, il calcium imaging e l'uso dei genetically-encoded voltage indicators, gli array di microelettrodi garantiscono il monitoraggio di singole cellule e interi network di neuroni per lungo tempo, in modo non invasivo e non fototossico. Inoltre, la recente integrazione degli array di microelettrodi nella tecnologia CMOS (complementary metal-oxide semiconductor) ha fatto sì che migliaia di elettrodi ravvicinati potessero registrare i potenziali d'azione neuronali anche da compartimenti subcellulari. Sono così divenute possibili nuove applicazioni nel campo degli HD-MEAs, come la stimolazione elettrica di singoli neuroni e lo studio dettagliato della forma d'onda e della propagazione del potenziale d'azione.

Dopo un'introduzione (Capitolo 1), vengono presentate modalità di stimolazione elettrica del singolo neurone nuove e ottimizzate, grazie ad una distanza di soli 17.5 μm tra gli elettrodi. Questa breve distanza permette di trovare il sito ottimale di stimolazione nel neurone e di selezionare ampiezze basse e forme d'onda efficaci, riducendo l'artefatto da stimolazione. Nel Capitolo 2, diverse forme d'onda, durate e ampiezze sono state analizzate sia per la stimolazione in tensione, che per quella in corrente. L'axon initial segment è stato dimostrato essere il sito di stimolazione più efficace e la sua maturazione nel tempo è andata di pari passo con il decremento dell'ampiezza necessaria per evocare un potenziale d'azione.

I Capitoli 3 e 4 della tesi presentano due studi su nuovi parametri elettrofisiologici, o metriche, che possono essere usati per determinare il fenotipo e gli stadi di maturazione di linee neuronali cellulari differenti e per analizzare gli effetti di farmaci. Ad oggi, differenze elettrofisiologiche e effetti di farmaci sono per lo più studiati facendo uso di metriche standard, come il numero delle oscillazioni di un network neuronale o il numero di potenziali d'azione registrati, che non

consentono analisi dettagliate come l'alta risoluzione fornita dagli HD-MEAs a tecnologia CMOS.

In particolare nel Capitolo 3 sono presentati parametri elettrofisiologici, sia nuovi che comunemente usati, per lo studio di network, singoli neuroni e compartimenti subcellulari. Queste metriche sono state usate per caratterizzare e comparare efficacemente linee cellulari umane di neuroni dopaminergici e motoneuroni, derivate da cellule staminali pluripotenti indotte (dall'inglese *induced.pluripotent stem cell*, iPSC). La stessa caratterizzazione è stata fatta per le corrispettive linee isogeniche che rappresentano il Parkinson e la sclerosi laterale amiotrofica. Le metriche sono state infine usate per caratterizzare gli effetti di diversi dosaggi di un farmaco in modo altamente riproducibile.

Nel Capitolo 4 è presentato lo studio di cellule staminali neurali differenziate per 2, 4 e 7 mesi fino a raggiungere lo stadio di network maturi di neuroni. Le cellule sono poi state traferite su HD-MEAs. Metriche aggiuntive, rispetto a quelle presentate nel Capitolo 3, sono state utilizzate per caratterizzare i tre stati di maturazione (2, 4 e 7 mesi) dal punto di vista del network, del singolo neurone e dei compartimenti subcellulari. La caratterizzazione è stata completata grazie a ulteriori analisi a mezzo del sequenziamento dell'RNA a singola cellula.

La tesi si conclude con prospettive future riguardanti l'utilizzo degli HD-MEAs nel campo dello screening di farmaci ad elevato contenuto di informazioni.

ACKNOWLEDGEMENTS

AUTHOR CONTRIBUTIONS

Dr. Alessio Paolo Buccino

Chapter 3: Contributed to spike sorting data and to the algorithm to compute the action potential propagation velocity.

Dr. Michele Fiscella

Chapter 2: Contributed to experimental design, technical support, manuscript revision and project supervision.

Chapter 3: Coordinated and conceived the project, contributed to work design and data interpretation and wrote the manuscript.

Dr. Urs Frey

Chapter 2: Contributed to experimental design and manuscript revision.

Prof. Dr. Andreas Hierlemann

Chapter 2: Contributed to experimental design, project idea, wrote the manuscript and supervised the project.

Chapter 3: Coordinated and conceived the project and contributed to writing the manuscript.

Chapter 4: Contributed to writing the manuscript.

Dr. Marian Hruska-Plochan

Chapter 4: Conceived the project, contributed to experimental design, performed and analyzed experiments, wrote the manuscript.

Dr. Sreedhar Saseendran Kumar

Chapter 3: Contributed to statistical analysis.

Camilla Marchetti

Chapter 2: Performed experiments and data analysis.

Dr. Jan Müller

Chapter 2: Contributed to experimental design, technical support, electrical stimulation scripts and manuscript revision.

Gustavo Prack

Chapter 3: Contributed to perform experiments and to action potential velocity computation.

Silvia Ronchi

Chapter 2: Contributed to experimental design, performed experiments and data analysis, wrote the manuscript.

Chapter 3: Contributed to the work design, performed and planned the experiments, analyzed and interpreted data, wrote the manuscript.

Chapter 4: Performed experiment, data analysis, statistical analysis and wrote the manuscript.

Dr. Manuel Schröter

Chapter 3: Contributed to writing the manuscript.

Dr. Vijay Viswam

Chapter 2: Contributed to experimental and technical support for the impedance measurements.

1 INTRODUCTION

1.1 Neuron and electrophysiology

The nervous system comprises of two broad categories of cells: neurons, which are specialized in electrical signal generation and processing, and neuroglia, which serve as support for nervous-system development and repair[1]. The neuron morphology features three main compartments: dendrites, soma and axon. Dendrites receive and process synaptic inputs from other neurons. The soma and the axon initial segment (AIS) are the neuron's signal integration sites. Axons conduct electrical signals to presynaptic terminals. Via chemical synapses the signals are then passed on to postsynaptic neurons[2]. The neuron membrane consists of a lipid bilayer[2]. The lipid bilayer is impermeable to ion movements. Ions can move across the lipid bilayer through ion channels, macromolecular pores made up of protein subunits that filter different ion types. Ions may move passively across the membrane via non-gated ion channels, which allow for ion movement at all times. Alternatively, ions can move across the membrane through either ligand- and signal-gated channels (molecule-induced opening) or voltage-gated ion channels, which open upon electric-potential differences[3]. Due to the always open potassium channels (potassium ions continuously diffuse down their concentration gradient out of the cell and leave behind negative uncompensated charges), there is a net positive charge in the extracellular space and a net negative charge in the cytosol, which gives rise to a resting membrane potential $V_m = V_{in} - V_{out} = -70\ mV$ (**Figure 1**). This potential opposes potassium diffusional efflux, and a dynamic equilibrium is established.

Figure 1. Membrane potential at resting conditions. The image, adapted from *Principles of Neural Science*, shows the net ion distribution across the neuron membrane.

Neurons generate electrical signals, through changes in ion densities across the neuron membrane. The electrical signal, called action potential (AP), is generated in proximity of the cell body, specifically at the AIS, a region of high ion-channel density. During the first AP

phase (**Figure 2**), the neuron membrane depolarizes, voltage-gated Na^+ channels open, and an inward Na^+ current results, which in turn causes further membrane depolarization. During the further course of depolarization, voltage-gated Na^+ channels are gradually inactivated, and voltage-gated K^+ channels open. The resulting outward K^+ current repolarizes the membrane. The repolarization phase is, in most cases, followed by a hyperpolarization phase with potential values lower than the resting membrane potential. Ion channel inactivation causes a refractory period during which no AP can be elicited. Initiated APs propagate unidirectionally along the axon[2].
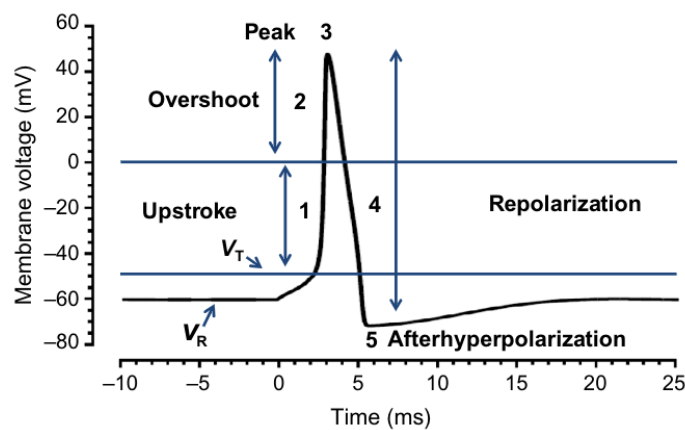
Figure 2. Action potential phases. The image shows the three phases: depolarization, repolarization and hyperpolarization, typical of an AP. The picture was adapted from Raghavan et al., 2019.

The arrangement of neurons in networks and their information processing characteristics have been intensely studied to understand how a human brain may function. Neuroscience seeks to understand physiological and pathological features of neurons and the respective networks. Electrophysiology studies the generation and propagation of electrical signals that are generated by neurons but also other cells like cardiomyocytes.

The electrophysiology techniques that allow for recording and studying neuronal activity can be classified in (i) intracellular recordings (e.g., patch clamp), (ii) extracellular recordings (e.g., microelectrode arrays), (iii) optical imaging (e.g., fluorescent indicators) and (iv) methods for large-scale recordings (e.g., electroencephalography)[4].

Patch clamp, the gold standard of intracellular recording techniques, includes a family of different approaches and recording scenarios, some of which include puncturing the neuron membrane with a glass micropipette, filled with an electrolyte solution. As the micropipette electrode is in direct contact with the cytosol, and as there is a reference electrode in the

surrounding buffer, it is possible to measure transmembrane potentials, currents mediated by ion channels and kinetics of ion channel gating[5]. Subthreshold events, such as excitatory and inhibitory postsynaptic potentials can also be recorded. Despite the big advantage of direct electrical coupling with the neuron, this technology has limitations concerning the invasive nature and associated low recording duration (max. ~2h), as well as low throughput[6], which render it unsuitable for signal-propagation and network-connectivity studies.

Genetically-encoded voltage indicators (GEVIs) are an optical technology that makes use of light-emitting protein sensors to monitor neuron membrane potentials[6–8]. Differently from patch clamp, GEVIs can be used to monitor entire neuronal networks, while the temporal resolution allows for detection of subthreshold events from dendritic spines and dendrites. GEVIs also overcome the time-resolution limitations of calcium imaging, as the membrane voltage deflections are faster than the calcium dynamics. However, GEVI application requires fluorescent indicators and exposure to intense light as well as extensive spatial and temporal averaging to detect associated signals. The resulting photodamage and phototoxic effects limit exposure times and observation frequency and intervals[7].

Microelectrode arrays (MEAs) comprise of small, densely-packed electrodes that record changes in extracellular ion concentrations, which result from electrical activity of neurons adjacent to the electrodes[4,6]. In contrast to intracellular recordings and optical techniques, MEAs offer access to entire neuronal networks over extended time periods (months), as they are not invasive. Additionally, high-density MEAs can also record APs of subcellular neuronal compartments and enable analysis of AP waveform and AP propagation.

1.2 High-density MEAs for electrical stimulation of neurons

In-vitro MEAs, first proposed in the 1970s[9–11] as arrangements of a few tens of thin-film metal electrodes, have seen rapid technology advances. Passive-transducer devices, silicon-based biosensors[12] and linear transistor arrays[13] opened the route for modern CMOS-based MEAs[14–20], which feature thousands of electrodes at high spatial density (pitch < 30μm). MEAs have been widely used to study the electrical activity of neurons in culture[21–23], brain slices[24,25], retina preparations[26] and organoids[27]. MEA technology is bi-directional and can be used for monitoring electrical neuronal signals and for manipulation of neurons via electrical stimulation[28].

Electrical stimulation has been extensively used to treat brain diseases[29,30], to study neuronal networks[28,31] and to enhance moto-rehabilitation[32,33]. Electrical stimulation initiates a

neuronal response by delivering charges via electrodes into the vicinity of neurons that then are depolarized[34]. The extracellular ion distribution changes upon application of a potential or a current through the stimulation electrode. The electrode-electrolyte interface can be schematically modeled as a capacitor (double layer capacitor) in parallel with a resistor (potential charge transfer). For example, a *negative* charge applied to the metal electrode would cause a redistribution of ions in the solution[35]. Positive ions would be attracted towards the electrode, and negative ions would be repelled. This ion redistribution would cause a change in the electrical potential, which - if large enough - could cause a depolarization of the neuron. If the electrical potential across the membrane $V_m = V_{in} - V_{out}$ reaches values of about -55 mV due to the ion redistribution, an AP is evoked in the neuron.

Taking advantage of thousands of electrodes at high spatial density, electrical stimulation performed with CMOS-based HD-MEA has reached unprecedented precision. In fact, thanks to the electrodes' small pitch, size and spacing, it is possible to stimulate individual axonal compartments[36,37]. However, a major limitation of HD-MEA electrical stimulation is the so-called *stimulation artifact*. As the stimulation amplitudes (mV) are three orders of magnitude larger than the extracellularly measured AP amplitudes (µV), the recording amplifiers may saturate upon stimulation, which may preclude AP readout. Optimization of the stimulation circuitry and experimental protocols [38,39] as well as signal post processing[40,41] are some of the currently used methodologies to reduce the stimulation artifact[42]. Still, many HD-MEA systems are unable to record neuronal responses from or near the stimulation electrode.

In this thesis, we tested multiple stimulation-signal durations, waveforms, and amplitudes, in voltage and current modalities to reduce the stimulation artifact. However, we did not aim at recovering the signal on the stimulation electrode itself. Optimizing the stimulation protocols, we were able to detect APs on the electrodes neighboring the stimulation electrode.

1.3 High-density MEAs for recording from iPSC-derived neurons and phenotyping

Induced pluripotent stem cells (iPSCs)[43] have revolutionized the field of stem-cell research, giving access to a large variety of human-derived cell types. As embryonic stem cells (ESCs), iPSC can differentiate into all derivatives of the three germ layers (mesoderm, ectoderm and endoderm)[44]. Induced pluripotent stem cells are generated from somatic cells by transient over-expression of transcription factors, which allows for developing models for diseases, drug screening and stem cell-based therapy. In fact, iPSCs offer the opportunity to integrate

genomics landscapes seen in humans that are often difficult to fully recapitulate in animals[45]. Additionally, owing to gene-editing techniques, it is possible to induce a disease phenotype by knocking out specific genes or to correct mutations that are causative to a disease[46].

The research in neurodegenerative diseases has been revolutionized by the advent of iPSCs and gene editing technologies. For example, iPSC-derived neurons from patients can be used to model neuronal disease degenerations, which would be impossible to study in a living patient. Studying neuronal electrophysiological properties is of great importance to understand neuronal disease mechanisms. In this context, HD-MEA electrophysiology offers the advantage of providing an *in-vitro* platform to investigate disease progression and phenotype over extended time.

In this thesis, we investigated the electrophysiology of iPSC-derived dopaminergic and motor neuronal lines and the corresponding isogenic lines modelling amyotrophic lateral sclerosis and Parkinson's disease. A set of network, single-cell and subcellular-resolution metrics were used to characterize and differentiate the cell lines. The high spatiotemporal resolution of CMOS-based HD-MEAs, enabled to establish new metrics, such as AP-propagation velocity, to characterize healthy and diseased lines. AP propagation velocity is difficult to extract using other electrophysiology techniques.

1.4 Scope and structure of the thesis

The focus of this thesis is on showing how the high-resolution of HD-MEAs opens a route to unprecedented extracellular-electrophysiology applications and readouts. First, we exploited the HD-MEA spatial resolution to perform precise single-cell stimulation. We optimized the stimulation parameters to minimize the stimulation artifact and to maximize the readout signal. Then, we used HD-MEAs to characterize the phenotypes of healthy and diseased iPSC-derived neuronal cell lines, exploring single-neuron and network metrics. Last, we describe an outlook to an application in the field of iPSC-derived neuron maturation, which relies on comparing the results of electrophysiology readouts and single-cell sequencing.

The thesis includes two publications (1, 2) and an extract of an article in preparation in collaboration with the Polymenidou group of University of Zurich (3):

1. Ronchi, S., Fiscella, M., Marchetti, C., Viswam, V., Müller, J., Frey, U., & Hierlemann, A. (2019). **Single-cell electrical stimulation using CMOS-based high-density microelectrode arrays**. *Frontiers in Neuroscience*, *13*, 208.

2. <u>Ronchi, S.</u>, Buccino, A. P., Prack, G., Kumar, S. S., Schröter, M., Fiscella, M., & Hierlemann, A. (2021). **Electrophysiological phenotype characterization of human iPSC-derived neuronal cell lines by means of high-density microelectrode arrays**. *Advanced Biology*, 2000223.

3. **TDP-43 proteinopathy in human neural networks explored at the single-cell level**, *in preparation*.

1.5   Summary of major results

Optimized single-cell-resolution stimulation

Different stimulation waveforms, durations and amplitudes were tested in voltage and current modes. Upon optimization of the stimulation parameters, individual-neuron stimulation was achieved and confirmed by combining high-density electrical recordings of single-neuron APs with immunostaining and confocal microscopy. Efficient stimulation amplitudes of few picoCoulombs of charge and the possibility of targeting the AIS helped to improve single-cell stimulation.
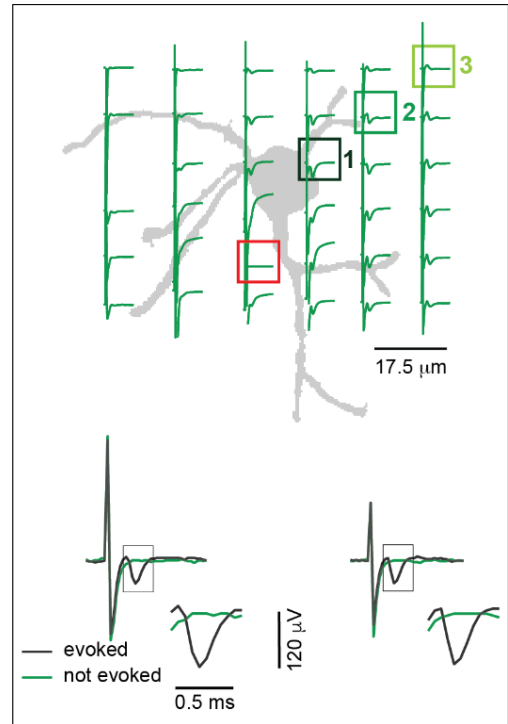
Electrical stimulation and dependence on maturation

We studied the correlation of the axon initial segment maturation with the neuron stimulability during cell development. Identified isolated neurons were followed optically and electrophysiologically over several days by combining live-staining, confocal microscopy and HD-MEA readouts. Results showed a decrease in stimulation amplitudes, needed to evoke APs, which was correlated to AIS growth.
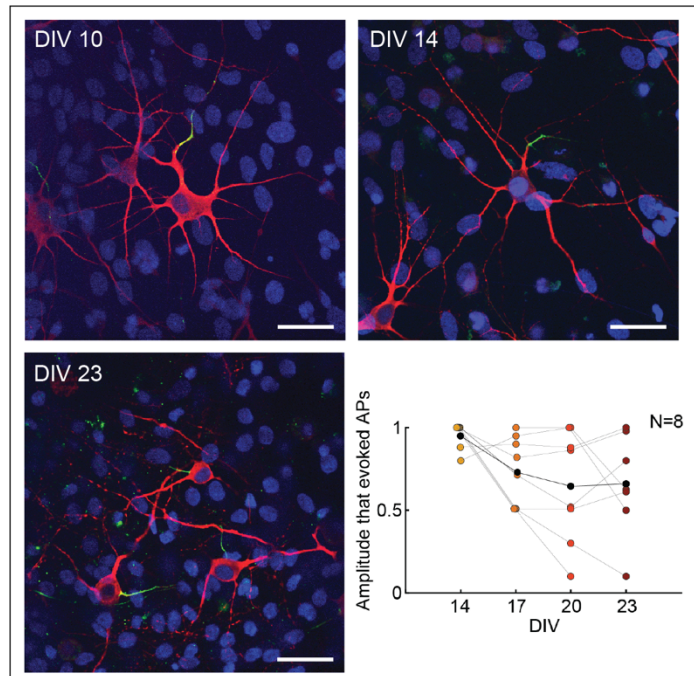
Phenotypic characterization of healthy and diseased human iPSC-derived neuronal cell lines

We studied electrophysiological properties and functional phenotypes of human iPSC-derived neuronal lines (motor neurons and dopaminergic neurons) and related disease-model lines (amyotrophic lateral sclerosis and Parkinson's disease). We recorded from hundreds of neurons simultaneously. Single-neuron metrics (e.g., spike rate, AP amplitude, AP velocity) and network metrics (e.g., burst rate) were analyzed and compared. Results showed significant differences between the respective cell lines for many of the analyzed metrics. HD-MEA technology was demonstrated to hold great potential for studying disease mechanisms and performing functional characterization.
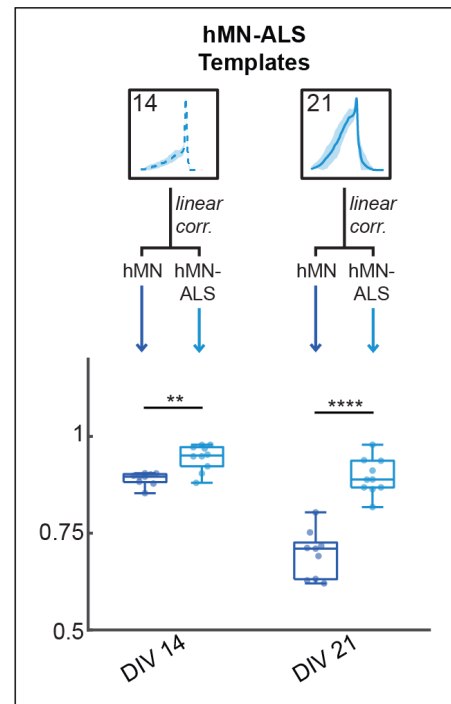
Characterization of drug effects at high resolution

Retigabine, a potassium channel opener, is known to decrease neural activity. Here, electrophysiology metrics were analyzed to evaluate compound effects. The percentage of active electrodes, the number of spikes per minute, or the inter-burst intervals were significantly altered upon administration of different retigabine doses. The large number and high spatial density of electrodes, and the possibility to select the location of the 1'024 simultaneously recorded electrodes entailed higher reliability and precision in monitoring retigabine effects.

Effects of differentiation time and maturation of neural stem cells on their electrophysiological properties

Neural stem cells, differentiated during 2, 4 and 7 months and cultured into mature neuronal networks, were plated on the HD-MEAs and recorded from simultaneously. 15 network, single-cell and subcellular-resolution metrics were used to successfully discriminate the different maturation times. Differences in the electrophysiological characteristics were then compared with results from single-cell RNA sequencing.
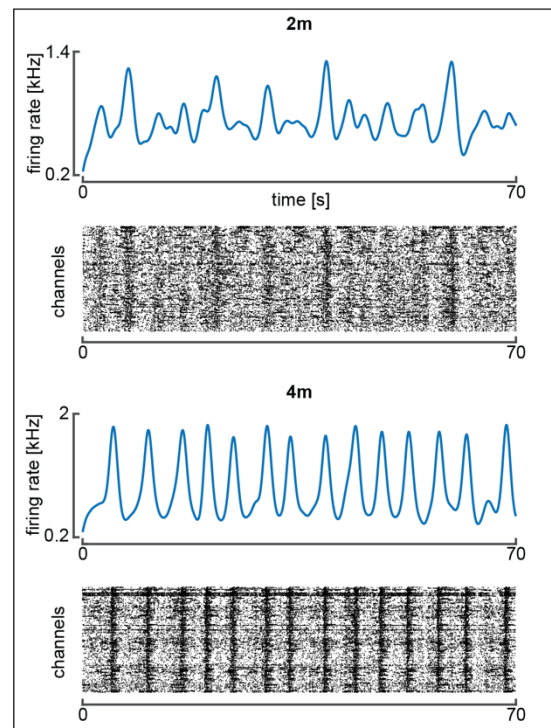
1.6   References

[1]   L. E. Purves, D., Augustine, G. J., Fitzpatrick, D., Hall, W. C., LaMantia, A.-S., McNamara, J. O., & White, *Neuroscience (4th Ed.)*, Sinauer Associates, **2008**.

[2]   T. M. Kandel, E. R., Schwartz, J. H., & Jessell, McGraw-Hill, Health Professions Division, New York, **2000**.

[3]   M. Raghavan, D. Fee, P. E. Barkhaus, **2019**, pp. 3–22.

[4]   M. E. Spira, A. Hai, *Nat. Nanotechnol.* **2013**, *8*, 83.

[5]   A. Molleman, *Patch Clamping*, Wiley, **2002**.

[6]   V. Emmenegger, M. E. J. Obien, F. Franke, A. Hierlemann, *Front. Cell. Neurosci.* **2019**, *13*, 1.

[7]   D. S. Peterka, H. Takahashi, R. Yuste, *Neuron* **2011**, *69*, 9.

[8]   H. H. Yang, F. St-Pierre, *J. Neurosci.* **2016**, *36*, 9977.

[9]   C. A. Thomas Jr, P. A. Springer, G. E. Loeb, Y. Berwald-Netter, L. M. Okun, *Exp. Cell Res.* **1972**, *74*, 61.

[10] G. W. Gross, E. Rieske, G. W. Kreutzberg, A. Meyer, *Neurosci. Lett.* **1977**, *6*, 101.

[11] J. Pine, *J. Neurosci. Methods* **1980**, *2*, 19.

[12] P. Bergveld, *IEEE Trans. Biomed. Eng.* **1970**, *BME-17*, 70.

[13] B. Besl, P. Fromherz, *Eur. J. Neurosci.* **2002**, *15*, 999.

[14] B. Eversmann, M. Jenkner, F. Hofmann, C. Paulus, R. Brederlow, B. Holzapfl, P. Fromherz, M. Merz, M. Brenner, M. Schreiter, R. Gabl, K. Plehnert, M. Steinhauser, G. Eckstein, D. Schmitt-Landsiedel, R. Thewes, *IEEE J. Solid-State Circuits* **2003**, *38*, 2306.

[15] L. Berdondini, K. Imfeld, A. Maccione, M. Tedesco, S. Neukom, M. Koudelka-Hep, S. Martinoia, *Lab Chip* **2009**, *9*, 2644.

[16] G. Bertotti, D. Velychko, N. Dodel, S. Keil, D. Wolansky, B. Tillak, M. Schreiter, A. Grall, P. Jesinger, S. Rohler, M. Eickenscheidt, A. Stett, A. Moller, K.-H. Boven, G. Zeck, R. Thewes, in *2014 IEEE Biomed. Circuits Syst. Conf. Proc.*, IEEE, **2014**, pp. 304–307.

[17] U. Frey, J. Sedivy, F. Heer, R. Pedron, M. Ballini, J. Mueller, D. Bakkum, S. Hafizovic, F. D. Faraci, F. Greve, K.-U. Kirstein, A. Hierlemann, *IEEE J. Solid-State Circuits* **2010**, *45*, 467.

[18] M. Ballini, J. Muller, P. Livi, Yihui Chen, U. Frey, A. Stettler, A. Shadmani, V. Viswam, I. Lloyd Jones, D. Jackel, M. Radivojevic, M. K. Lewandowska, Wei Gong, M. Fiscella, D. J. Bakkum, F. Heer, A. Hierlemann, *IEEE J. Solid-State Circuits* **2014**, *49*, 2705.

[19] V. Viswam, J. Dragas, A. Shadmani, Y. Chen, A. Stettler, J. Muller, A. Hierlemann, in *2016 IEEE Int. Solid-State Circuits Conf.*, IEEE, **2016**, pp. 394–396.

[20] D. Tsai, D. Sawyer, A. Bradd, R. Yuste, K. L. Shepard, *Nat. Commun.* **2017**, *8*, 1802.

[21] E. Cotterill, D. Hall, K. Wallace, W. R. Mundy, S. J. Eglen, T. J. Shafer, *J. Biomol. Screen.* **2016**, *21*, 510.

[22] A. M. Tukker, F. M. J. Wijnolts, A. de Groot, R. H. S. Westerink, *Neurotoxicology* **2018**, *67*, 215.

[23] S. Ronchi, M. Fiscella, C. Marchetti, V. Viswam, J. Müller, U. Frey, A. Hierlemann, *Front. Neurosci.* **2019**, *13*, DOI 10.3389/fnins.2019.00208.

[24] M. E. J. Obien, A. Hierlemann, U. Frey, *Sci. Rep.* **2019**, *9*, 788.

[25] X. Yuan, M. Schröter, M. E. J. Obien, M. Fiscella, W. Gong, T. Kikuchi, A. Odawara, S. Noji, I. Suzuki, J. Takahashi, A. Hierlemann, U. Frey, *Nat. Commun.* **2020**, *11*, 4854.

[26] M. Fiscella, F. Franke, K. Farrow, J. Müller, B. Roska, R. Azeredo da Silveira, A. Hierlemann, *J. Neurophysiol.* **2015**, *114*, 2485.

[27] A. S. Monzel, L. M. Smits, K. Hemmer, S. Hachi, E. L. Moreno, T. van Wuellen, J. Jarazo, J. Walter, I. Brüggemann, I. Boussaad, E. Berger, R. M. T. Fleming, S. Bolognin, J. C. Schwamborn, *Stem Cell Reports* **2017**, *8*, 1144.

[28] S. S. Kumar, J. Wülfing, S. Okujeni, J. Boedecker, M. Riedmiller, U. Egert, *PLOS Comput. Biol.* **2016**, *12*, e1005054.

[29] J. S. Perlmutter, J. W. Mink, *Annu. Rev. Neurosci.* **2006**, *29*, 229.

[30] A. L. Benabid, S. Chabardes, J. Mitrofanis, P. Pollak, *Lancet Neurol.* **2009**, *8*, 67.

[31] J. Wülfing, S. S. Kumar, J. Boedecker, M. Riedmiller, U. Egert, *Proc. ESANN 2018* **2018**.

[32] S. Raspopovic, M. Capogrosso, F. M. Petrini, M. Bonizzato, J. Rigosa, G. Di Pino, J. Carpaneto, M. Controzzi, T. Boretius, E. Fernandez, G. Granata, C. M. Oddo, L. Citi, A. L. Ciancio, C. Cipriani, M. C. Carrozza, W. Jensen, E. Guglielmelli, T. Stieglitz, P. M. Rossini, S. Micera, *Sci. Transl. Med.* **2014**, *6*, 222ra19.

[33] M. Armenta Salas, L. Bashford, S. Kellis, M. Jafari, H. Jo, D. Kramer, K. Shanfield, K. Pejsa, B. Lee, C. Y. Liu, R. A. Andersen, *Elife* **2018**, *7*, e32904.

[34] S. F. Cogan, *Annu. Rev. Biomed. Eng.* **2008**, *10*, 275.

[35] D. R. Merrill, M. Bikson, J. G. R. Jefferys, *J. Neurosci. Methods* **2005**, *141*, 171.

[36] M. Radivojevic, D. Jäckel, M. Altermatt, J. Müller, V. Viswam, A. Hierlemann, D. J. Bakkum, *Sci. Rep.* **2016**, *6*, 31332.

[37] D. J. Bakkum, U. Frey, M. Radivojevic, T. L. Russell, J. Müller, M. Fiscella, H. Takahashi, A. Hierlemann, *Nat. Commun.* **2013**, *4*, 2181.

[38] Y. Jimbo, N. Kasai, K. Torimitsu, T. Tateno, H. P. C. Robinson, *IEEE Trans. Biomed. Eng.* **2003**, *50*, 241.

[39] P. Livi, F. Heer, U. Frey, D. J. Bakkum, A. Hierlemann, *IEEE Trans. Biomed. Circuits Syst.* **2010**, *4*, 372.

[40] C. Sekirnjak, P. Hottowy, A. Sher, W. Dabrowski, A. M. Litke, E. J. Chichilnisky, *J. Neurophysiol.* **2006**, *95*, 3311.

[41] D. A. Wagenaar, S. M. Potter, *J. Neurosci. Methods* **2002**, *120*, 113.

[42] P. Hottowy, A. Skoczeń, D. E. Gunning, S. Kachiguine, K. Mathieson, A. Sher, P. Wiącek, A. M. Litke, W. Dąbrowski, *J. Neural Eng.* **2012**, *9*, 066005.

[43] K. Takahashi, S. Yamanaka, *Cell* **2006**, *126*, 663.

[44] H. M. Blau, G. Q. Daley, *N. Engl. J. Med.* **2019**, *380*, 1748.

[45]   P. Clerc, S. Lipnick, C. Willett, *Drug Discov. Today* **2016**, *21*, 939.

[46]   Y. Shi, H. Inoue, J. C. Wu, S. Yamanaka, *Nat. Rev. Drug Discov.* **2017**, *16*, 115.

2 Single-Cell Electrical Stimulation Using CMOS-Based High-Density Microelectrode Arrays

Silvia Ronchi[1*], Michele Fiscella[1,2], Camilla Marchetti[1], Vijay Viswam[1,2], Jan Müller[1,2], Urs Frey[1,2] and Andreas Hierlemann[1]

[1]Department of Biosystems Science and Engineering, ETH Zürich, Basel, Switzerland
[2]MaxWell Biosystems AG, Basel, Switzerland

* Correspondence:
Silvia Ronchi
silvia.ronchi@bsse.ethz.ch

2.1 Abstract

Non-invasive electrical stimulation can be used to study and control neural activity in the brain or to alleviate somatosensory dysfunctions. One intriguing prospect is to precisely stimulate individual targeted neurons. Here, we investigated single-neuron current and

voltage stimulation *in vitro* using high-density microelectrode arrays featuring 26'400 bidirectional electrodes at a pitch of 17.5 μm and an electrode area of 5×9 μm². We determined optimal waveforms, amplitudes and durations for both stimulation modes. Owing to the high spatial resolution of our arrays and the close proximity of the electrodes to the respective neurons, we were able to stimulate the axon initial segments (AIS) with charges of less than 2 picoCoulombs. This resulted in minimal artifact production and reliable readout of stimulation efficiency directly at the soma of the stimulated cell. Stimulation signals as low as 70 mV or 100 nA,with pulse durations as short as 18 μs, yielded measurable action potential initiation and propagation. We found that the required stimulation signal amplitudes decreased with cell growth and development and that stimulation efficiency did not improve at higher electric fields generated by simultaneous multi-electrode stimulation.

2.2 Introduction

Electrical stimulation[1,2] is a consolidated technique that has been widely used to study neuronal networks[3,4], to treat brain diseases[5,6] and somatosensory dysfunctions[7–13], and to enhance moto-rehabilitation[14,15]. Electrical stimulation was combined with prosthetic implants in a variety of *in vivo* applications[16,17]. For example, epiretinal implants feature electrodes that deliver an electric signal to neurons located in the retina, in close proximity to the optic nerve. The purpose of eye implants is to artificially substitute non-functional retina layers that fail to transduce light into electrical signals for the brain[7–11]. Electrical stimulation is employed as well in cochlear implants, where electrodes are used for hearing restoration by stimulating specific cochlear areas depending on sound frequency[12,13,18]. Neural stimulation has been used in the field of prosthesis embodiment for paralyzed patients to restore sensations in upper and lower limbs[14,15]. Furthermore, deep brain electrical stimulation of the subthalamic nucleus is used in Parkinson's treatment[5,6] to reliably suppress and control the patients' tremor.

Although a large variety of electrical stimulation-based prostheses exists, a major limitation of these devices is their low spatial resolution in delivering stimulation signals and the difficulty to locally constrain the electrical field to attain accurate and precise stimulation of preferably

28

individual single cells. Indeed, blurred images, low sound resolution, inaccurate proprioceptive sensations, and adverse neurocognitive effects may be the results of imprecise electrical stimulation. The described shortcomings motivated us to explore stimulation parameters and regimes and to develop methods for accurate and precise charge injection. *In vitro* technologies enable to explore a large set of parameters to electrically stimulate neurons in cultures and 3D tissues or slices. Results and findings of *in vitro* studies of electrical stimulation can potentially be translated and optimized for *in vivo* applications (e.g., epiretinal implants and cochlear implants).

In vitro high-density microelectrode arrays (HD-MEAs) facilitate electrical-signal readout and stimulation of multiple neurons simultaneously at high-spatiotemporal resolution[19]. Traditional microelectrode arrays have been used since 1970s[20] for extracellular electrophysiology. Several studies have been carried out to investigate electrical stimulation parameters in neuronal cultures with the aim to find the most efficient way to elicit neuronal responses[9,21,22]. Although the principles of electrical stimulation have been established, the large electrode size and pitch did not allow to perform stimulation at subcellular resolution and to demonstrate reliable single-neuron targeting.

The introduction of HD-MEAs in complementary-metal-oxide-semiconductor (CMOS) technology for *in vitro* applications[23–29] enabled to obtain high spatial resolution and a large overall sensing area. Hundreds of researchers worldwide at universities, research institutes and pharmaceutical industry are currently using different CMOS-based HD-MEAs for their studies. CMOS-based HD-MEAs are also commercially available from several suppliers, including Multichannel Systems (Germany), 3Brain (Switzerland) or MaxWell Biosystems (Switzerland). With the advent of neurons derived from human induced pluripotent stem cells (hiPSCs), the interest in HD-MEAs is rapidly growing, as such devices are suitable to assess hiPSC functionality of healthy and disease phenotypes. In this study, we used a 26'400-electrode CMOS chip[23], with a sensing area of 3.85×2.10 mm², an electrode pitch of 17.5 μm and an electrode size of 5×9 μm², which provided subcellular resolution for readout and stimulation. The device enabled targeting of the axon initial segment (AIS) for stimulation, which was demonstrated to ensure efficient and accurate stimulation[30,31], and the device enabled signal readout upon stimulation in direct proximity to the cell soma of the very same cell.

An important issue with electrical stimulation through microelectrodes in densely packed arrays is the so-called "stimulation artifact", which is characterized by saturation of the recording amplifiers that are connected to the stimulation electrode itself and the surrounding

electrodes during hundreds of μs or longer. This saturation is a consequence of the large stimulation signal amplitudes, ~50-100 mV, while the readout amplifiers feature microVolt sensitivity. Different from other approaches[32], we did not aim at recovering the signal on the stimulation electrode itself, as the large density of electrodes, present in our array, allows for recording from different electrodes, still spanning under the same neuron of interest. Moreover, we did not use any strategy to suppress artifacts in this study, as our interest was to compare the different stimulation strategies and parameters also with respect to artifact generation. Electrodes at a distance of only 17.5 μm from the stimulation electrode were already available for readout in all cases, partially due to the comparably low stimulation-signal amplitudes that we could afford owing to accurate targeting of the stimulation-sensitive AIS[30]. The artifact depends on the stimulation signal amplitude, the applied waveform, and its duration. Therefore it is crucial to identify the stimulation signal that produces the lowest artifact while still reliably inducing an action potential (AP).

This study was targeted at finding optimal stimulation modalities, i.e., to achieve the most efficient stimulation of neurons with our HD-MEAs at minimal artifacts, by comparing different stimulation waveforms, amplitudes and durations, both in voltage and current mode. We used biphasic and monophasic rectangular waveforms for stimulation in voltage mode[22], and charge-balanced biphasic and triphasic rectangular waveforms for stimulation in current mode[9,22,32]. We compared the efficacy of the voltage and current stimulation regimes, characterized the influence of the electrode impedance, and measured stimulability during cell growth and development in culture. Finally, we simulated and tested different multi-electrode configurations and compared the obtained results.

2.3   Materials and Methods

2.3.1   Animal use

All experimental protocols were approved by the Basel Stadt veterinary office according to Swiss federal laws on animal welfare and were carried out in accordance with the approved guidelines.

2.3.2   High-density microelectrode arrays

A CMOS-based HD-MEA[23] was used for *in vitro* stimulation and recording. The device features 26'400 Pt electrodes (each 5×9 μm² at a pitch of 17.5 μm) occupying a sensing area of 3.85×2.10 mm². The HD-MEA system includes 1'024 configurable readout channels that

can be used to record simultaneously. The readout-channel noise is 2.4 μV_{rms} in the band between 300 Hz and 10 kHz and 5.4 μV_{rms} in the band between 1 Hz and 300 Hz. The readout channels' gain is programmable up to 78 dB, depending on the application. Additionally, the device features 32 stimulation units that can be used in both, current or voltage mode. The sampling frequency is 20 kSamples/s, and the overall power consumption is 75 mW. Gold bond wires connect the chips to printed circuit boards (PCBs) and are protected from saline solutions (e.g., culture medium) using epoxy (Epo-Tek 353ND, 35ND-T, Epoxy Technology Inc., Billerica, MA, USA). The electrodes were coated with Pt-black, the chips were then sterilized for 40 min in 70% ethanol and rinsed 3 times with deionized (DI) water before every cell plating.

2.3.3 Platinum black deposition

A porous Pt-black layer was deposited on the electrodes to increase the surface area and decrease the electrode impedance, which improves the signal-to-noise ratio (SNR) of recorded signals. A 2 mL solution of chloroplatinic acid hexahydrate (7 mM, Sigma Aldrich, Saint Louis, MO, USA) and lead acetate (0.3 mM, Honeywell, Morris Plains, NJ, USA) in DI water was pipetted onto the exposed region of the HD-MEA chip. A Pt reference electrode was immersed in the solution and current of 550 μA was applied to the array electrodes for 1.30 min.

2.3.4 Cell cultures

Prior to culturing cells, the HD-MEA electrode area was treated with 20 µL of 0.05% (v/v) poly(ethyleneimine) (Sigma Aldrich) in borate buffer (Thermo Fisher Scientific, Waltham, MA, USA) at 8.5 pH, for 40 min at room temperature. This step improves cell adhesion and makes the substrate more hydrophilic. We rinsed the chips three times with DI water. Next, we added 8 µL of 0.02 mg ml^{-1} laminin (Sigma Aldrich) in Neurobasal medium (Gibco, Thermo Fisher Scientific) to support the growth and differentiation of the cells. The chips were incubated with laminin for 30 minutes at 37 °C. During this time, we dissociated cortices of Wistar rats at embryonic day 18 in trypsin with 0.25% EDTA (Gibco). After 20 minutes of digestion, the cortices were washed twice with plating medium, then triturated, and the cells were counted. We counted with a hemocytometer by diluting the cells in 0.4% Trypan blue stain solution (Gibco). We then seeded between 15'000 to 25'000 cells over an active area of approx. 8 mm^2. The chips were afterwards incubated at 37 °C for 30 min before adding 1.5 mL

of plating medium. The plating medium consisted of 450 mL Neurobasal (Invitrogen, Carlsbad, CA, USA), 50 mL horse serum (HyClone, Thermo Fisher Scientific), 1.25 mL Glutamax (Invitrogen), and 10 mL B-27 (Invitrogen). After 76 h, we changed 50% of the plating medium to growth medium, which consisted of 450 mL D-MEM (Invitrogen), 50 mL Horse Serum (HyClone), 1.25 mL Glutamax (Invitrogen) and 5 mL sodium pyruvate (Invitrogen). The procedure was repeated twice a week. The chips were kept inside an incubator at 37 °C and 5% CO_2. Every chip was equipped with a lid, and additional DI water in a 35-mm-Ø petri-dish was added to prevent evaporation. All the experiments were conducted between days in vitro (DIVs) 10 and 30.

2.3.5 Microscopy and stainings

We used NeuroFluor NeuO (Stemcell Technologies, Vancouver, Canada) live staining to locate neurons on the array before the stimulation experiments. The cells were incubated for 1 h at 37 °C with 2 mL growth medium containing 0.15% NeuO. The chips were then washed 2 times with growth medium.

We also performed neuron fixation after stimulation experiments by using 4% paraformaldehyde (Life Technologies, Thermo Fisher Scientific). Sample permeabilization and blocking of non-specific antibody binding were done using a PBS 1X solution containing: 10% normal donkey serum (NDS) (Sigma Aldrich), 1% bovine serum albumin (BSA) (Sigma Aldrich), 0.02% Na-Az (Sigma Aldrich), 0.5% Triton X (Sigma Aldrich). Primary and secondary antibodies were diluted in a PBS 1X solution containing: 3% normal donkey serum (NDS), 1% bovine serum albumin (BSA), 0.02% Na-Az, 0.5% Triton X. We used antibodies against MAP2 (Abcam, Cambridge, UK), Ankyrin G (Santa Cruz Biotechnology, Dallas, TX, USA), and the fluorescent dye Hoechst (Invitrogen) to stain neurons, axonal initial segments (AIS), and nuclei. We imaged cells on the HD-MEA chip with a Nikon NiE upright confocal microscope, with a Yokogawa W1 spinning disk scan head, 6 laser lines and a fluorescence recovery after photobleaching (FRAP) unit.

2.3.6 Stimulation and data analysis

Electrical stimulation was controlled via an on-chip digital analog converter (DAC) and software programmable through a Python application programming interface (API).

We used both, voltage and current stimulation modalities. In both, a charge is applied to the stimulation electrode. Ideally, only charge redistribution in the double-layer capacitor, formed

at the electrode/electrolyte interface, occurs and charge transfer and redox reactions involving electron transfer at the electrode surface (Faradaic processes) are avoided. Using current stimulation, the charge can directly be controlled, while the voltage may assume large values depending on the specific current path. High electrode voltages may produce unwanted electrochemistry (Faradaic processes), tissue damage, or electrode degradation. In the case of voltage stimulation, one can control the voltage, while the injected current depends on the electrode impedance (**Figure S1**), which may vary considerably due to fabrication variation or aging. Precisely controlling the applied voltage helps to prevent electrolysis, which may occur outside the water window and may damage the electrodes or cause cell death.

We used a randomized voltage stimulation protocol including four different waveforms: biphasic cathodic-anodic, biphasic anodic-cathodic, monophasic anodic, monophasic cathodic, see also **Figure 2A**[22]. The protocol included four durations of 50, 100, 150 and 200 μs per phase and six stimulation signal amplitudes (40, 80, 120, 160, 200 and 240 mV peak-to-peak). For current stimulation, we applied a randomized protocol of two waveforms, biphasic anodic-cathodic and triphasic anodic-cathodic-anodic, both charge balanced[9], five durations of 10, 15, 18, 20 and 50 μs per phase, and eight stimulation signal amplitudes (42, 63, 84, 105, 126, 147, 168 and 189 nA). Every individually shaped stimulation pulse of both modalities was repeated 30 times during the entire protocol in a randomized way in order not to evoke neuronal plasticity processes. The stimulation frequency was 1 Hz for both modalities, as stimulation in the frequency band between 0.2 and 1 Hz was reported not to entail significant changes in the AIS position[33]. We selected 1 Hz, the upper bound, to limit overall time needed for the stimulation experiments.

A custom-made software was used to visualize and record the extracellular signals from the electrodes. The extracellular action potential (EAP) spatial distribution or "electrical footprint" of a neuron, which is the voltage-signal distribution over the multiple electrodes, was reconstructed using spike sorting algorithms (UltraMegaSort, [34]). The software identifies the spikes with a threshold of 4.5 times the standard deviation of the noise. Using this software, we then could identify and select the stimulation electrodes based on the EAP amplitudes.

The collected data was analyzed in MATLAB. To verify the presence of an evoked APs, we set a threshold of four times the standard deviation of the noise, together with a temporal window of 1.5 ms. An automatic script registered the EAPs for the 30 repetitions of every sent waveform, and rendered a visual record that could be inspected to verify the counting. Cases where the artifact partially covered the EAPs were classified as "missing EAP" during

automatic registration. In these cases, we applied visual inspection and manual correction as appropriate.

2.3.7 Impedance characterization

To characterize electrode impedances, we applied a readout gain of 2 and 20 repetitions of a biphasic anodic-cathodic current stimulation pulse with a duration of 1 ms per phase and an amplitude of 140 nA to bright Pt electrodes and with a duration of 2.5 ms per phase and an amplitude of 560 nA to Pt-black electrodes. Such low gain in the readout channels avoided DC voltage saturation of the stimulation channel. The lower waveform durations and amplitudes avoided channel saturation in case of bright Pt, because of the higher impedance.

To determine the electrode impedance, we fitted the voltage readout on the stimulation electrode with equations derived from the Gouy-Chapman-Stern model of an electrode[35] (**Figure S2**). We added a constant equivalent input impedance Z_{in} for the recording channel input impedance in parallel to the electrode equivalent circuit. The electrode equivalent circuit had two unknown values, the charge transfer resistance, R_{ct}, and the double layer capacitance, C_{dl}. These values were computed by fitting the obtained experimental data in MATLAB using the following equation:

$$V(t) = \frac{I_{stim}R_{ct}\left(1 - e^{-\frac{t}{C_{dl}R_{ct}}}\right)}{1 + \frac{R_{ct}}{Z_{in}}\left(1 - e^{-\frac{t}{C_{dl}R_{ct}}}\right)} \tag{1}$$

In this equation V is the readout voltage and I_{stim} the applied stimulation current. We defined initial values for C_{dl} and R_{ct} by referring to values reported in literature[35–40].

To confirm the simulation results with a larger number of electrodes, we applied a sine-wave voltage stimulation on the reference electrode surrounding the array and recorded the corresponding signals through electrode sets of the array. The sine wave had a frequency of 1 kHz and an amplitude of 50 mV$_{pp}$ (peak-to-peak). The recording channels and circuits are characterized by a finite and constant input impedance, which should ideally be high for neural applications and higher than the electrode impedance to ensure signal integrity [19]. We compared the obtained electrode impedances with the input impedances of the recording channels for the whole array to characterize impedance homogeneity across the array. We also performed impedance measurements on three stimulation electrodes in PBS, before and after conducting a full set of stimulation experiments in current and voltage mode. After the

experiment, the impedance varied in average by 0.07 nF (~ 5% of the average electrode impedance value for Pt black).

2.3.8 COMSOL simulations

We simulated the stimulation pulse extension across the array of the used multi-electrode configurations in **COMSOL Multiphysics 5.3a**. The model includes 4 main components (libraries): geometry, materials, electric currents, and mesh. For the geometry, we used a configuration of 36 planar electrodes, with a 5×9 µm² surface area for each electrode and a pitch of 17.5 µm, which is consistent with the HD-MEA electrode characteristics. An external block of $500 \times 500 \times 100$ µm³ was added as the electrolyte solution. Four reference electrodes (dimensions of 5×245 µm²) were placed around the electrode array. The electrodes were simulated assuming platinum as electrode material, while the electrolyte solution was a saline solution with an electrical conductivity of 0.7 Sm^{-1}. For the electrical characterization, we simulated voltage stimulations. We used a biphasic anodic-cathodic waveform with an amplitude of 100 mV and a duration of 100 µs per phase. The electric-current library was used to simulate the voltage and electric field distributions upon voltage stimulation.

2.3.9 Multi-electrode stimulation

To implement multi-electrode stimulations in voltage mode, we used a custom-made Python script to control two DACs to stimulate two electrodes at the same time. In a first configuration, we applied a biphasic waveform on one electrode and the same waveform but with opposite sign on a neighboring electrode. This configuration limited the charge flow across the array, which decreased the artifact extension and spreading. In a second configuration, we applied a biphasic waveform to one electrode and connected the neighboring electrode to ground with the intention to limit the electric field and artifact extension. External reference electrodes remained always connected.

2.3.10 Availability of materials

Adapted MATLAB scripts and COMSOL model scripts, used for the analysis of the data in Figs. 2, 3, 4, 5 and 6 are available at the following repository: [link]. Moreover, we can provide raw data sets (total of 10 TB) at reasonable request.

2.4 Results

2.4.1 Artifacts of current and voltage stimulation

A major limitation of any electrical stimulation is the resulting artifact, which obscures the EAP readout likewise in current and voltage modes. To compare artifacts generated during voltage and current stimulation of cortical neurons, we plated ~ 15,000 cortical neurons on the array and labeled them neurons with NeuroFluor NeuO live-staining (**Figure 1A**) to identify individual neurons. We determined the most suitable electrode and the smallest stimulation signal amplitude that could evoke EAPs with 90% success rate over 30 repetitions. We used biphasic waveforms in both modalities and compared cases with similar artifact shapes. The duration was set to 100 and 20 µs per phase for voltage and current stimulation, respectively. The different durations were a consequence of the high efficiency of the stimulation buffers in current mode, which showed a reliable charge injection for durations longer than 18 µs (Figures S3, S4). In current mode, the stimulation buffers could deliver a sharp charge injection regardless of the electrode impedance. In voltage mode, however, the shortest efficient pulse duration was found to be > 50 µs (Paragraph 2.4.2, **Figure S4**), due to the different stimulation buffers' design[23].

Since the artifact duration is governed primarily by the stimulation pulse duration, shorter current pulses produced shorter, more easily detectable and distinguishable AP artifacts than the voltage pulses. This is shown in Figures 1B and C. For the latter, not only were the nearby extracellular APs obscured, but the artifact amplitudes were also significantly larger. In voltage mode, the evoked EAPs were shifted with respect to the baseline, in comparison to spontaneous EAP activity, so that they could not always be easily detected by using a negative amplitude threshold (four times the standard deviation of the noise) for spike detection. Only the neurons producing high-amplitude EAPs could be detected by using a negative voltage threshold while the other neurons were not used for analysis.

Owing to the high-density electrodes, the short current stimulation pulse enabled a signal readout and determination of stimulation success already on the next neighboring electrode, 17.5 µm away from the stimulation site (Figures 1B-1C, center and right). Upon stimulating axonal compartments, like the AIS, it was possible to measure signals at the corresponding cell soma of the same neuron, which enabled to unambiguously determine stimulation success.
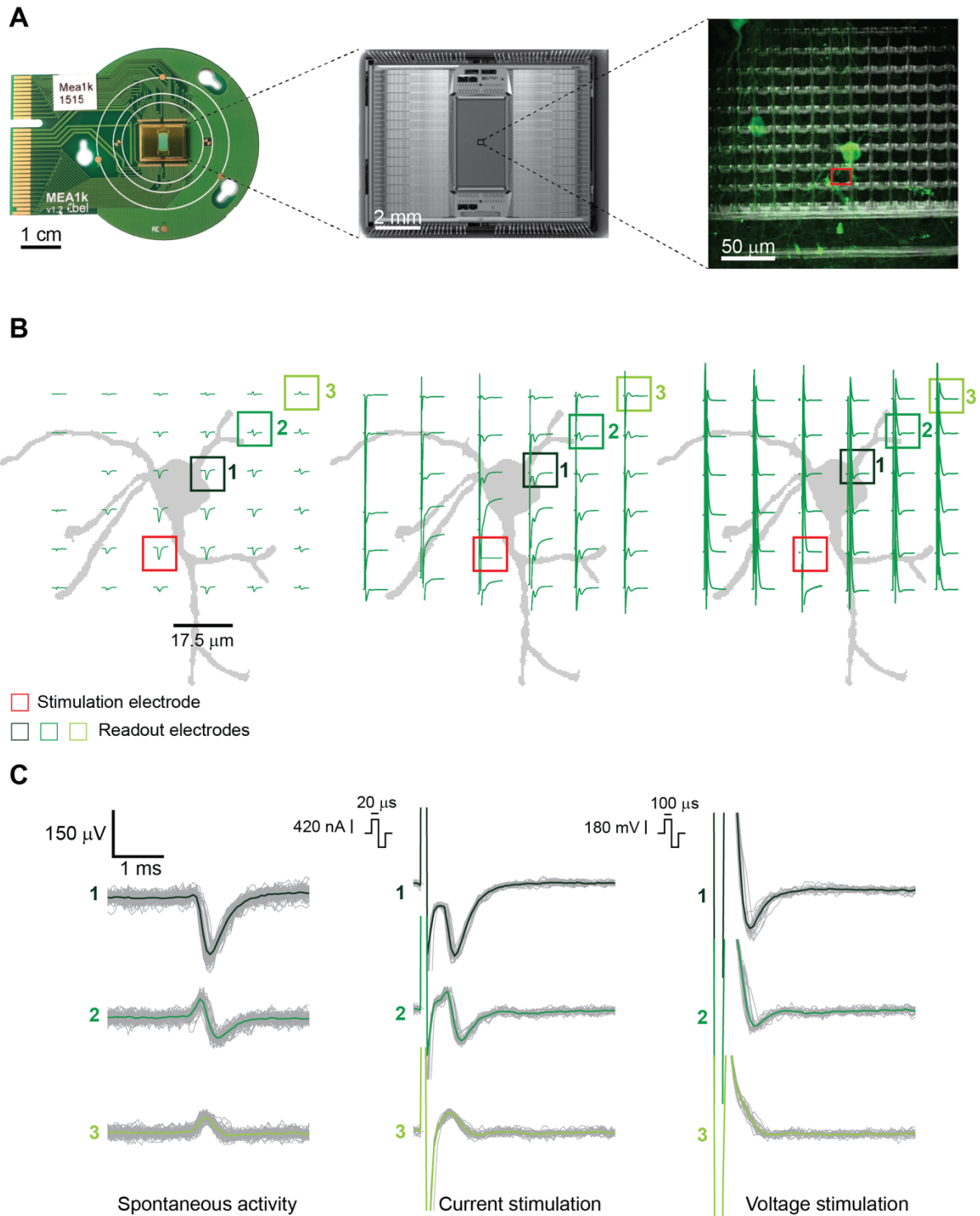
Figure 1. (A) (from left to right) PCB-mounted HD-MEA chip, photomicrograph of the chip, and enlargement of a subsection of the array including about 100 electrodes with live-stained neurons highlighted in green. The stimulation electrode used in B is highlighted in red. The picture was taken using an immersion 60X-magnification lens at the periphery of the array, where the cell density is lower. **(B)** Illustration of the neuron, labeled in A, and corresponding electrode locations, with superimposed measured signals. (Left) Spontaneous EAPs obtained after spike sorting. (Center) EAPs after current stimulation of the selected neuron. (Right) EAPs after voltage stimulation. Current stimulation entailed a biphasic anodic-cathodic waveform of 20 µs per phase. Voltage stimulation entailed a biphasic anodic-cathodic waveform of 100 µs per phase. The smallest stimulation signal amplitudes that still evoked

APs 27 times during 30 repetitions (90% efficiency) were used. **(C)** Signals from three of the readout electrodes in A and B (numbered boxes). (Left) Extracellular signals recorded during spontaneous neuronal activity composed of >100 detected EAPs. (Center and right) Extracellular signals recorded from the same electrodes during 30 repetitions of current and voltage stimulation.

2.4.2 Effect of durations, amplitudes and waveforms, in voltage and current stimulation modes

Although we noticed that the HD-MEA produced smaller artifacts in current mode, we wanted to study the relevant parameters to efficiently evoke APs in both, current and voltage modes. Current stimulation is preferred and used for many *in vivo* applications[15], due to the fact that the injected charge can be determined independently of the impedance. However, voltage stimulation offers the advantage to precisely control the voltage and avoid electrode or cell/tissue damage as a consequence of electrolysis (for a more detailed discussion see Section 2.3.6). In line with previous electrical-stimulation studies *in vitro* (Wagenaar, Pine, and Potter 2004; Grosberg et al. 2017; Hottowy et al. 2012), we investigated different parameters for both, current and voltage modes. Our strategy was to efficiently stimulate neurons in the region of the AIS and to then read out the corresponding evoked action potentials at the cell soma and several other locations, which was possible due to the availability of a large number of electrodes at high density, the small signal amplitudes needed to stimulate at the AIS, and the possibility to deliver short and efficient stimulation pulses (≥ 18 µs). For voltage stimulation, we used biphasic cathodic-anodic, biphasic anodic-cathodic, monophasic anodic and monophasic cathodic waveforms. The stimulation protocol included four durations for every waveform and six amplitudes in a randomized sequence (40, 80, 120, 160, 200 and 240 mV peak to peak). Neurons were stimulated between DIV 10 and 30. Stimulation electrodes were selected after identifying the spatial distribution or electrical footprint of extracellular EAPs of individual neurons. Electrodes recording the highest amplitudes of single-neuron action potentials were selected as stimulation electrodes, as they were presumably located under the neuronal compartments that are most sensitive to stimulation[30,31]. The compartment producing the largest-amplitude extracellular action potentials and being most sensitive to stimulation has been recently identified as the AIS (Radivojevic et al. 2016; Bakkum et al. 2018). The results are displayed in Figure 2A: The stimulation results of two different neurons upon applying four stimulation voltage waveforms with different amplitudes and waveform durations are shown. The monophasic cathodic waveform was found to be the most efficient waveform in evoking APs in the voltage mode, followed by the biphasic anodic-cathodic waveform. The monophasic

anodic and the biphasic cathodic-anodic waveform featured lower efficiency. Another result we observed is that a phase duration of 50 μs was not sufficient to reliably evoke APs, whereas there was no major difference for phase durations longer than 100 μs. In Figure 2B, recorded voltage waveforms and close-ups of successful (AP was elicited, black) and unsuccessful (no AP, green) stimulations are shown to demonstrate how EAPs look like in the presence of stimulation artifacts. To consolidate the stimulation results in 2A, we repeated the randomized protocols with 16 additional neurons (Figure 2C). We determined the peak-to-peak voltage (V_{pp}), which was needed to evoke APs in 90% of the stimulations over 30 repetitions for those cells. Two phase durations, 50 μs (gray) and 100 μs (green), were used and compared. At the top of the graph, the percentages of failure in evoking APs, while using the 4 waveforms up to a maximum amplitude of 240 mV are given for the 2 different durations. The obtained results confirmed the aforementioned low efficacy of 50 μs phase duration. For using a phase duration of 50 μs, one should, for a successful stimulation, deliver the same charge as for using 100 μs, but the settling time of the stimulation buffers and the electrode impedance imposed limits on the stimulation efficacy with such short phase durations (see Figure S4).

To confirm that the selected neurons were effectively stimulated, we superimposed the "electrical footprints" of spontaneous activity after spike sorting (using UltraMegaSort) with the spatial distribution of stimulation-evoked extracellular action potentials. The spontaneous activity was recorded using a high-density block of electrodes in the region of interest during at least one minute (> 100 EAP). The superposition shows a spatial and temporal match of spontaneous and stimulation-triggered EAPs. However, the amplitudes of the superimposed EAPs are not so easy to compare as a consequence of the stimulation artifact (Figure 2D). A clear identification of the neuron could be performed by using its electrical "footprint", the spatial distribution of extracellular APs in conjunction with upright confocal microscopy. Using these features and methods, we could prove that, indeed, the neuron of interest was stimulated in its perisomatic region as EAP readout of the very same neuron was possible, e.g., in an axonal branch nearby. Stimulation was very selective, and individual neurons could be stimulated without eliciting EAPs in neighboring neurons.

After execution of the electrical stimulation protocols, selected neurons were stained for correlating neuron morphologies with their EAP spatial distribution, recorded through the electrodes. In particular, we investigated which neuronal compartment was closest to the stimulation electrode. We observed that the most efficient stimulation electrode was located in close proximity to the AIS (green AnkyrinG staining), confirming previous reports[30,31] (Figure 2E).
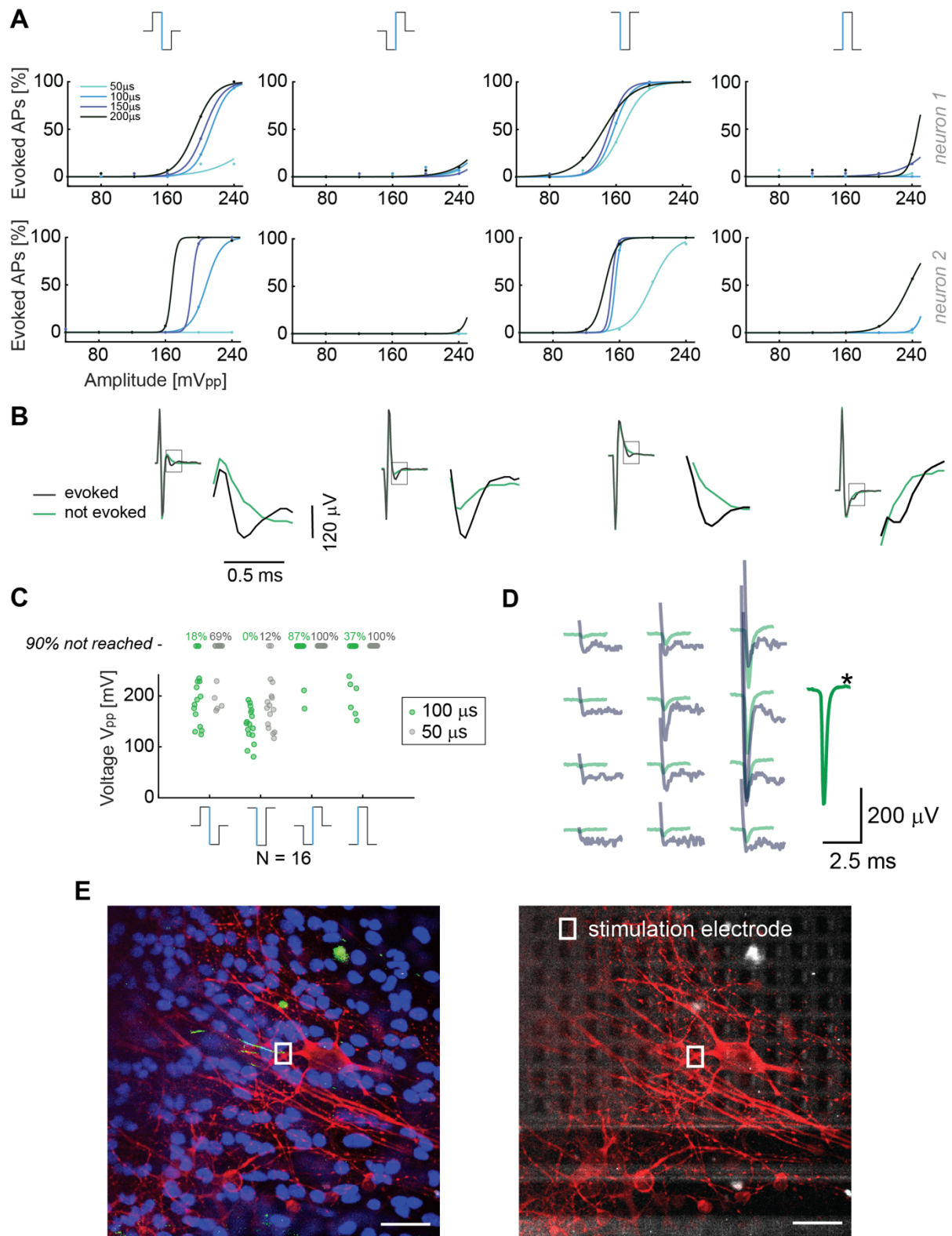
Figure 2. (A) Results from voltage stimulation of two neurons. At the top, the four different waveforms that were used are displayed. The figure shows that lower voltage amplitudes are sufficient to evoke APs when using monophasic cathodic and biphasic anodic-cathodic waveforms. A phase duration of 50 µs was less efficient than phase durations of 100, 150 and 200 µs. We applied 30 repetitions for every waveform, duration and amplitude in a randomized manner. **(B)** Recorded voltage signals including stimulation artifact for successful and non-successful voltage stimulations are displayed for the four stimulation waveforms in A. No

measures were taken to suppress the artifact. The close-ups show the region, in which the neuron's response eventually occurred. The voltage signal (artifact only) recorded during/after a stimulation that did not evoke an AP is displayed in green, voltage signals (artifact plus superimposed neuronal response) recorded during a successful stimulation are displayed in black. **(C)** Voltage stimulation results of 16 neurons. The points represent the smallest voltages (Vpp) that evoked APs in 90% of the stimulations during 30 repetitions; the signal duration was 100 µs per phase (green dots) or 50 µs per phase (gray dots). At the top, the percentages of failure in evoking APs upon using the 4 waveforms with amplitudes of up to 240 mV are given for the 2 different durations. **(D)** Overlay of the spike-sorted spontaneous activity of a neuron (green) and its response (grey) upon voltage stimulation through the electrode marked with a black star (*). **(E)** Neuron stainings; nuclei were stained in blue (Hoechst), neuronal structures in red, (anti-MAP2) and the AIS in green (Ankyrin G). The stimulation electrode is indicated with a rectangle (white). In the right picture, the electrode array is visible below the stimulated neurons. Scale bar: 35 µm.

In a second set of experiments, we used similar protocols for the current stimulation mode, where we investigated the effect of two different waveforms, namely biphasic anodic-cathodic, and triphasic anodic-cathodic-anodic (amplitude ratio 2:3:1). We used five phase durations and eight signal amplitudes in a randomized sequence (42, 63, 84, 105, 126, 147, 168 and 189 nA). Monophasic waveforms were not used to not compromise charge balancing. The results of two different stimulated neurons in **Figure 3A** show that the two waveforms provide similar efficiency in stimulating the targeted neurons for different phase durations and amplitudes. In Figure 3B, recorded voltage waveforms and close-ups of successful (AP was elicited, black) and unsuccessful (no AP, red) stimulations are shown to demonstrate how EAPs look like in the presence of stimulation artifacts. The results can be compared with panel 2B, showing the signals for the voltage stimulation mode. For the voltage stimulation mode, the AP always is superimposed on the artifact, whereas, in current mode, the evoked EAP is temporally more clearly separated from the artifact and much easier to detect. This better detectability is, to some extent, a consequence of the shorter duration of the stimulation signal in the current mode. To consolidate the stimulation results, we repeated the same randomized protocol with 20 additional neurons with a phase duration of 20 µs. Several HD-MEAs were used in parallel to speed up experiments. The obtained results are shown in Figure 3C. All current stimulation events delivering charges of up to 3 pC were successful.

As in the case of voltage stimulation, an overlay of the spatial distribution of spontaneous-activity EAP signals and the current stimulation-induced EAP was used to confirm the identity and successful stimulation of the targeted neurons. Spontaneous and stimulated EAPs match temporally, spatially and amplitude-wise (Figure 3D). Additionally, readout electrodes very close to the stimulation electrode also provided clearly detectable signals. The result in Figure

3D can be compared to Figure 2D for voltage mode, where an amplitude comparison was not possible as a consequence of the large artifact.
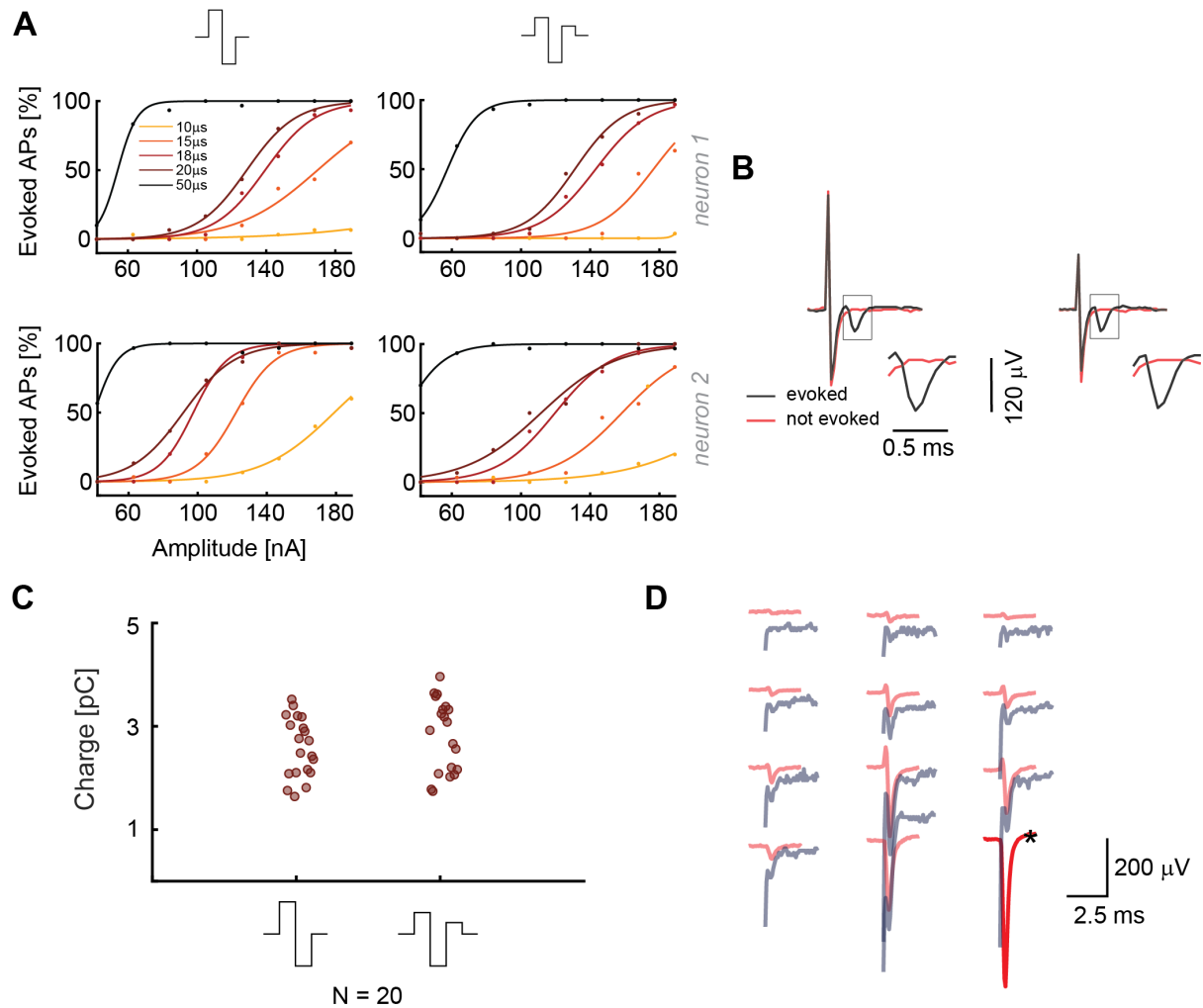
Figure 3. (A) Results from current stimulation of two neurons. At the top, the two waveforms that were used are displayed. The efficacy in evoking APs is almost the same for both waveforms. 30 repetitions were used for every waveform, phase duration and stimulation signal amplitude in a randomized manner. **(B)** Recorded voltage signals including stimulation artifacts for successful and non-successful current stimulations are displayed for the two stimulation waveforms in A. No measures were taken to suppress the artifact. The close-ups show the region, in which the neuron's response eventually occurred. The voltage signal (artifact only) recorded during/after a stimulation that did not evoke an AP is displayed in red, voltage signals (artifact plus superimposed neuronal response), recorded during a successful stimulation, are displayed in black. **(C)** The current stimulation results of 20 neurons are displayed. The points represent the smallest charges that evoked APs in 90% of the stimulations during 30 repetitions; the signal duration was 20 µs per phase. **(D)** Overlay of the spike-sorted spontaneous activity of a neuron (red) and its response (grey) upon current stimulation through the electrode marked with a black star (*).

To summarize, the most efficient stimulation in voltage mode can be achieved by using monophasic cathodic and biphasic anodic-cathodic waveforms with a duration of 100 µs per

phase. In current mode, biphasic and triphasic waveforms show the same efficacy, but the biphasic waveform is shorter than the triphasic waveform, which facilitates EAP readout. Durations of 18-20 µs per phase have proven to be efficient (**Figure S3**). Additionally, we noticed that artifact amplitudes are larger for monophasic voltage stimulation and biphasic current stimulation waveforms. In the case of the commonly used voltage stimulation mode, a biphasic anodic-cathodic waveform should be used, as it represents a good combination of stimulation efficacy and artifact duration.

2.4.3 Impedance measurements to compare voltage and current stimulation

As mentioned in Section 3.2, both voltage and current stimulation are widely used to stimulate neuron. Voltage stimulation offers the advantage to reliably obviate Faradaic processes by precisely controlling the electrode voltage and keeping it significantly below 0.8 - 1 V to obviate water electrolysis and cell and electrode damage (Weiland, Anderson and Humayun 2002; Wagenaar, Pine, and Potter 2004). However, the injected charge cannot be controlled and is a function of the electrode impedance. On the other hand, the voltage cannot be controlled upon using current stimulation, so that high electrode voltages can occur in case of high impedance, which may entail unwanted electrochemistry, tissue damage, or electrode degradation. Yet, the charge delivered by the electrode (not the charge path in the preparation) can be precisely controlled, and potentially short current stimulation durations entail short artifacts and fast recovery to baseline values.

To better compare efficacies and differences of current- and voltage-controlled stimulation modes in depolarizing neuronal membranes (from -70 mV to ∼ -55 mV) and evoking APs, it is necessary to also consider the delivered charge. To this end, we established a method to determine electrode impedances, so that charge injection of voltage and current pulses could be calculated and compared.

We applied a biphasic current pulse to an electrode and used a low gain (G = 2) for reading out the voltage signals of the same electrode (see Paragraph 2.3.7). We then fitted the voltage readout from the stimulating electrode with a theoretical electrode model (Figure S2, **Figure 4A**) by using only the first half of the biphasic anodic-cathodic waveform. The charge transfer resistance, *Rct*, and the double layer capacitance, *Cdl*, were kept as unknown values. After examining (n=10) bright Pt and Pt-black electrodes, we found that the *Cdl* was 0.077 ± 0.0138 nF for bright Pt electrodes and 1.44 ± 0.15 nF for Pt-black electrodes (Figure 4B). The results were obtained with an electrode area of 5×9 µm².
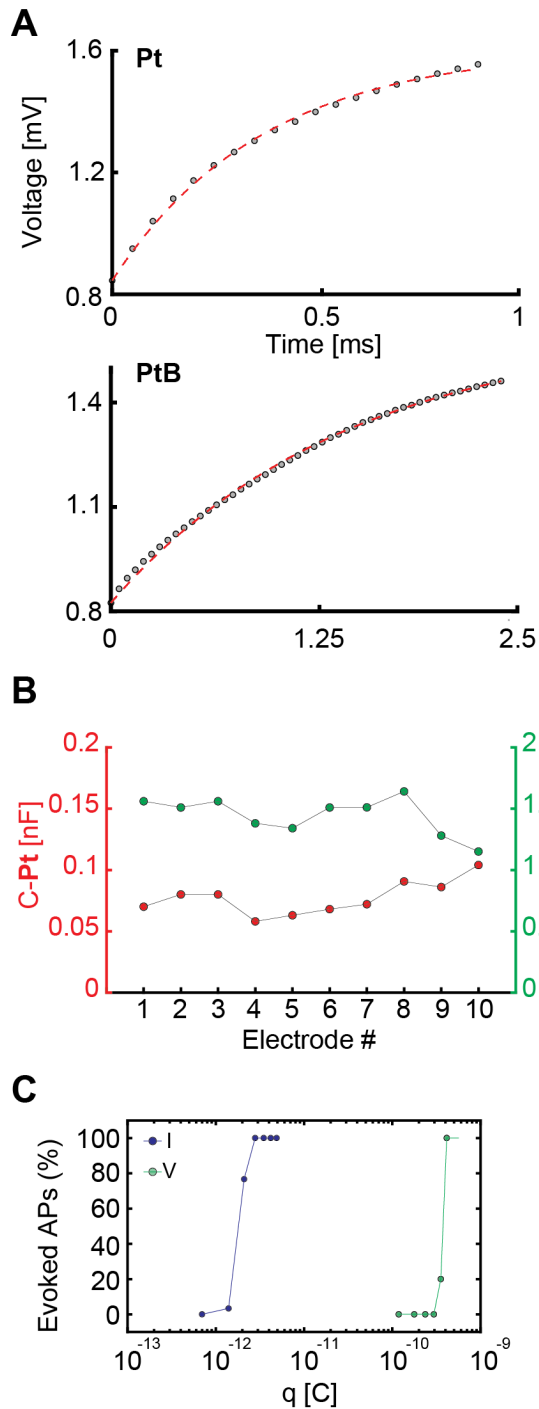
Figure 4. (A) Fitting of an electrode model to the experimental data of measured voltage values upon applying a current stimulus to an electrode. For bright Pt (Pt), a current stimulation was performed with a biphasic anodic-cathodic waveform with an amplitude of 140 nA, a duration of 1 ms per phase and a readout amplifier gain of 2. For Pt-black (PtB) the amplitude was 560 nA, the duration 2.5 ms per phase, and the readout amplifier gain was equal to 2. The different waveforms durations and amplitudes are due to the readout channel saturation in case of bright Pt as a consequence of the higher impedance. In both cases, only the first half of the waveform, i.e., the positive part was used for the fits and is displayed. **(B)** Capacitance values of 10 Pt and PtB electrodes are presented. The values were computed as a result of the fitting in A by setting the capacitance as an unknown value. **(C)** Charges required for efficient voltage and current stimulation of the same neuron. For current stimulation, the waveform had a duration of 20 µs per phase, while the duration for voltage stimulation was 100 µs per phase. The stimulation protocol included 30 repetitions of every stimulation amplitude in a randomized manner. For current stimulation, the charge was computed as $q = I \times t$, i.e., the product of applied current and time. For voltage stimulation, the charge was computed as $q = C \times \Delta V$, i.e., the product of the computed capacitance and the voltage change upon stimulation.

To extend these results to a larger number of electrodes, we applied a sine-wave stimulation to 26'400 electrodes and proved that their impedance (in terms of voltage readout) was homogeneous over the array (see histograms in **Figure S5**). This allowed us to use the mean capacitance value of 1.44 nF for Pt-black to compare current and voltage stimulation. Based on the obtained capacitance values, we calculated the charge associated with voltage stimulation and compared it to current stimulation for the same neuron (Figure 4C). We used biphasic waveforms in both modalities, with a duration of 20 µs per phase in current mode and 100 µs per phase in voltage mode. We used a

randomized stimulation protocols including 30 repetitions of every stimulation signal amplitude. Using the common capacitor formula $C=\frac{q}{\Delta V}$, we found that, for the very same neuron, the charge delivered through voltage stimulation is two orders of magnitude larger than the one needed to achieve the same results or stimulation efficiency in current stimulation mode (Figure 4C). Our results show that current stimulation, characterized by a constant rate of charge injection, displays higher efficiency in eliciting neuronal responses with respect to voltage stimulation, which is characterized by an exponential decrease in charge injection (see also Figure S1). Results of 3 more neurons confirm the same orders of magnitudes and charge differences for current and voltage stimulation (**Figure S6**). The stimulation efficacy in current and voltage mode is also largely depending on the stimulation buffer implementation[23].

2.4.4 Multi-electrode stimulation

An array of densely distributed electrodes enables to apply different stimulation configurations, either by using the standard single-electrode stimulation approach, or by selecting several electrodes at the same time for applying signals or for grounding. Normally, all unused array electrodes are left floating and do not have a defined potential. The use of neighboring electrodes as stimulation and reference or ground electrodes can produce a locally larger electric field strength, which, in turn, could lead to lower voltages required for stimulation in voltage mode. Moreover, it is possible to stimulate with opposite-sign waveforms on adjacent electrodes to reduce and limit stimulation artifacts.

Using COMSOL Multiphysics, we simulated the voltage and electric field distribution on the array for different candidate electrode configurations to see if an increase in electric field strength could increase neuron stimulability and decrease the artifact lateral extension. Three configurations were selected (Figures 5A, B): (i, iv) stimulation with a biphasic voltage waveform (±100 mV) through one electrode against a global reference electrode in solution; (ii, v) stimulation with two neighboring electrodes, using biphasic voltage waveforms (±100 mV) with opposite signs; (iii, vi) stimulation with a biphasic waveform (±100 mV) applied to one electrode, while the neighboring electrode was grounded. All other array electrodes were left floating.

To assess if one of the two chosen configurations with local ground or opposite-sign stimulation signal could improve stimulation efficiency by entailing higher local voltage drops or electric-field strengths, we simulated two probe locations at the right and left side of electrode E1 (**Figure 5A**), at a height of 1μm above the electrode plane. For configuration (i),

one stimulation electrode against a global reference electrode, the voltage drop left and right of the electrode was identical, because the global reference electrode is far away and positioned outside the electrode array. In configuration (iii), the grounded neighboring electrode slightly modified the voltage drop at the right probe location. In configuration (ii), however, the application of a signal to the neighboring second electrode induced a voltage drop decrease at the location of the right probe, as a result of the applied opposite-sign voltages (Figure 5C). However, the electric field between the two electrodes was increased (v) (Figure 5C). Nevertheless, looking at the voltage distribution around the stimulation electrodes suggests comparable results for all configurations, with even a possible decrease in stimulation efficacy for axons that would run through the center region between the two electrodes with opposite-sign waveforms.

To verify the simulation, we then tested the efficacy of these three configurations in evoking APs in neuronal cultures on the HD-MEA. We stimulated six different neurons, after having determined the most reliable electrodes in evoking APs at the respective AISs. First, a randomized voltage stimulation protocol was applied to one electrode, using the global reference electrode at the periphery of the array. A biphasic anodic-cathodic voltage stimulation waveform, evidenced to be efficient (Section 2.4.2), was used with a phase duration of 100 µs and an amplitude range between 40 and 160 mV. We then repeated the same stimulation protocol by using a grounded reference electrode close to the stimulation electrode to increase the electric field. Finally, we used two electrodes delivering opposite waveforms for stimulation, which further increased the local electric field and, additionally, reduced the lateral extension of the artifact (**Figure S7**). In all the modalities, also the reference electrodes at the sides of the array were left connected. We found differences in the voltage required to evoke activity in the different neurons (range between 60-120 mV, Figure 5D), however, we did not find major differences for using the three stimulation scenarios explained, simulated and displayed in Figures 5B, C.

This experimental result is in line with the simulations in Figure 5C, which shows comparable extracellular voltage levels for all three configurations. Consequently successful stimulation and APs initiation is not much influenced by applying the three different configurations.
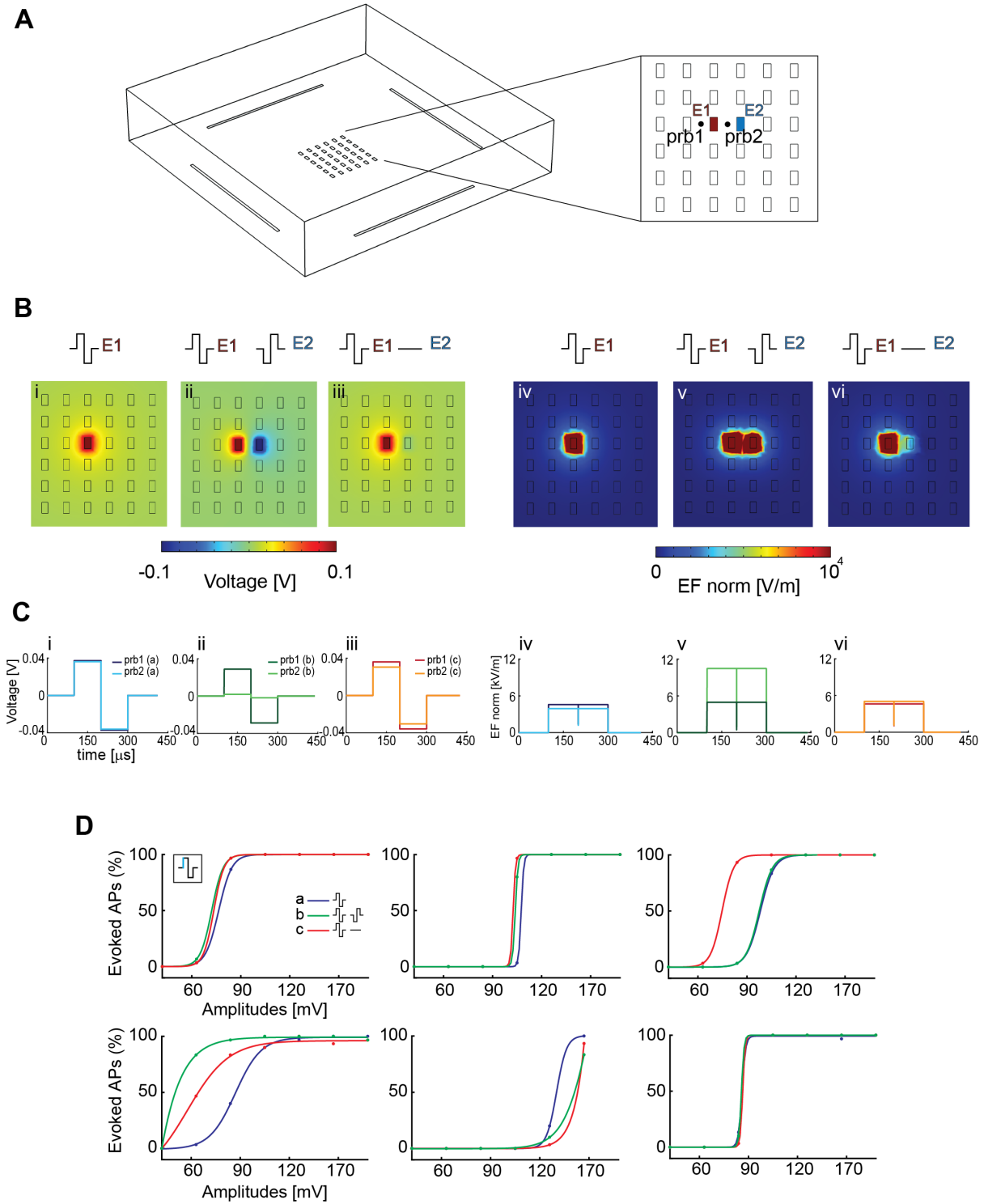
Figure 5. (A) Simplified HD-MEA geometry for COMSOL simulations: 36 planar electrodes at a pitch of 17.5 µm and featuring an area of 5 × 9 µm²; 4 reference electrodes were placed at the borders of the array. E1 and E2 denote the electrodes that were used for the simulations in panel B. prb1 and prb2 denote two probe locations, at the right and at the left side of electrode E1, that were used to compute the voltage and the electric-field values for the three configurations in B. The two probe locations were chosen so as to compare the effect of using a second array electrode. **(B)** The simulation was performed in voltage mode, and an amplitude of ±100 mV was used. The voltage and electric field distributions after stimulating with one

47

electrode against a global reference electrode in solution are represented in panels (i) and (iv), those for a stimulation with two neighbored electrodes with synchronized waveforms of opposite signs are represented in (ii) and (v), and those for applying a biphasic waveform to one electrode, while the neighboring electrode was grounded are represented in (iii) and (vi). The electric field (EF norm) was calculated as $\sqrt{E_x^2 + E_y^2 + E_z^2}$. **(C)** Voltage (i, ii, iii) and electric-field (iv, v, vi) distributions at the probe locations in the respective configurations (i-vi) of B. The voltage drop, which is responsible for the AP initiation by electrical stimulation, is comparable in all the cases, except for the two-electrode stimulation (ii), where it is somewhat decreased. The electric field is stronger in the case of the two-electrode stimulation (v). **(D)** Stimulation with a biphasic voltage waveform of six different neurons using the three configurations simulated in COMSOL in B. There were differences in the voltage required to evoke activity in the different neurons (range between 60-120 mV), however, there were no major differences for using the three stimulation scenarios explained and displayed in B.

2.4.5 Stimulability across cell development increases in early stages of neuronal growth and development

To assess if the ability to stimulate neurons is correlated to cell culturing time and AIS growth, we observed and stimulated single neurons during different DIVs. The experimental time points were 14, 17, 20 and 23 DIV. We used NeuroFluor NeuO to do live-staining of neurons (**Figure 6A**). To ensure staining effectiveness, we repeated the staining before every experiment. Isolated cells were identified and three to six stimulation electrodes were used for stimulation. We chose the most efficient stimulation electrode, which was the electrode with the highest extracellular voltage readout (AIS), to execute the stimulation protocol. We used a randomized current stimulation protocols to avoid neuronal adaptation [33]. The use of current stimulation was motivated by the reduced artifact (Paragraph 2.4.1) and the more reliable AP readout (Paragraph 2.4.2). A biphasic anodic-cathodic waveform was used with a duration of 20 µs per phase. We observed that, over 10 DIVs, the neurons moved by a maximum of two electrode distances, which is equal to 35 µm. In case that the neurons moved by one electrode distance or more, the stimulation electrode was also changed. If the neurons did not move, the most efficient stimulation electrode remained the same (Figure 6A). The movement was evaluated by using the electrical "image and simultaneous upright confocal imaging. We monitored the soma position with respect to the stimulation electrode position during the experiment days. The results show that the stimulation amplitudes, required to evoke APs, decreased during the first half of the experiment (from DIV 14 to DIV 20), and stabilized around DIV 20 and 23 (Figures 6B-C). An increase in stimulation amplitudes was mostly due to neuron movement and change of the relative position with respect to the stimulation electrode as evident, e.g., in Figure S8 for day 20.
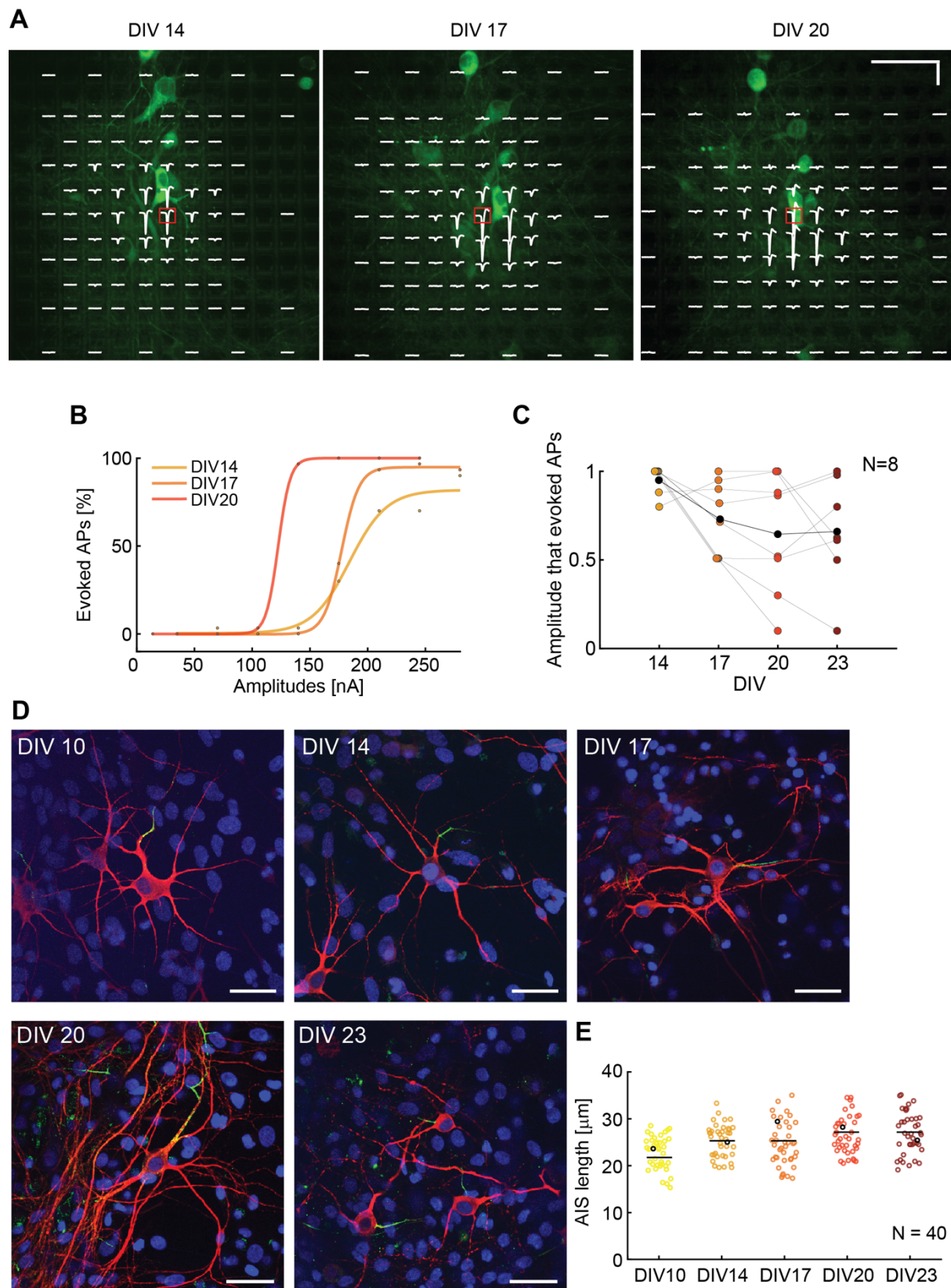
Figure 6. (A) Superimposed fluorescence image and electrical footprint of the same neuron at DIVs 14, 17, 20. The stimulation electrodes used for the analysis are indicated with a red box. The stimulation electrode changed position with the neuron movements during the experiment. The signals recorded on the different electrodes are displayed in white (electrical footprint). Horizontal scale bar: 50 μm, vertical scale bar: 100 μV. **(B)** Current stimulation activation

curves of the neuron in A over time (DIVs). The stimulation amplitudes necessary to evoke APs decreased between DIV 14 and 20. **(C)** Stimulability experiments for N=8 neurons. For every neuron, the stimulation amplitudes were normalized to the highest amplitude that was necessary to evoke APs 90% of times over 30 repetitions during the DIVs 14-23. The stimulability varied from neuron to neuron. We observed a trend of decreased stimulation amplitudes between DIV 14 and 20 that then stabilization between DIV 20 and 23. The average relative stimulation current amplitude is represented with black dots. **(D)** Sample microscopy stainings showing fixed neurons at DIV 10, 14, 17, 20, 23. The nuclei are represented in blue, the neurons in red and the AISs in green. The 5 neurons are represented as black dots in panel E. Scale bar 35 μm. **(E)** AIS lengths and length distribution over time: DIVs 10, 14, 17, 20, 23. The average length tends to slightly increase over time in vitro (N=40).

We also recorded and compared the EAPs of spontaneous neuronal activity over the different DIVs so as to ensure the identity of the respective neurons. To verify if the increase in stimulability was correlated with an AIS growth, we stained neurons at DIV 10, 14, 17, 20 and 23 and we computed the length of N=40 AIS. We found that there is the tendency of an AIS-average-length increase with increasing DIVs (Figure 6D).

2.5   Discussion

In this study we showed that it is possible to selectively and reliably stimulate individual neurons by applying current and voltage pulses through the 26'400 electrodes of an HD-MEA. We tested different stimulation waveforms, durations and amplitudes in voltage and current mode. We demonstrated that we were able to stimulate individual neurons by combining high-density recording of single-neuron action potentials with immunostaining and confocal microscopy. Previous studies (Wagenaar, Pine, and Potter 2004) reported that, in voltage mode, the biphasic anodic-cathodic waveform was most efficient for selective stimulation, followed by the cathodic-anodic one. We found that the most efficient stimulation waveform is the monophasic cathodic waveform, followed by the biphasic anodic-cathodic, by comparing the V_{pp} for the same pulse width (Figure 2). It is, however, important to note that we used significantly lower stimulation voltages (80 mV_{pp}), as we could target the most sensitive region of a neuron, the AIS, for stimulation. Moreover, we used much smaller electrodes with respect to the 30 μm diameter electrodes in the study by Wagenaar et al, 2005. In current mode, we confirmed that the triphasic waveform is an efficient stimulation signal that produces a comparably smaller artifacts than the biphasic one[9]. In comparison to previous findings, we were able to improve selectivity due to the high electrode density and the inherent possibility of directed targeting of neurons and their AISs[30]. We, hence, could stimulate with comparably

low charges of a few picoCoulombs (Figure 3). Moreover, the small electrodes provided sufficient stimulation charge density also for small applied voltages.

In comparing current and voltage stimulation parameters for our HD-MEA, we found that a waveform duration of 100 µs per phase was required to efficiently evoke EAPs in voltage mode. In current mode, instead, a duration of only 20 µs per phase was required, which entailed a shorter artifact duration. However, it needs to be mentioned that the possible shorter signal duration in current mode was also a consequence of the settling time of our stimulation buffers. According to our measurements, current stimulation is the preferable stimulation modality, which is in line with reports in literature[8,9]. By using current stimulation it was possible to use already the next neighboring electrodes, at 17.5 µm pitch from the stimulation electrode, for EAP recording (Figure 1, 2). Owing to the high spatial resolution and dense electrode packing of the array, it was possible to read out electrical activity at the cell soma while stimulating the axon initial segment of the very same cell, so that it was possible to accurately estimate stimulation success and efficiency.

Based on our experiments, we estimated current stimulation to be more efficient than voltage stimulation in evoking APs using our HD-MEA. To further test this assumption, we determined the electrode impedances by measuring and modeling the voltage readout upon applying current stimulation[35]. The fit of the measurement data to the model returned capacitance values of ~1.4 nF for Pt-black and ~0.07 nF for bright Pt electrodes. We used these capacitance values to compare voltage and current activation curves, and found that the charge needed to evoke APs in current mode is, indeed, by two orders of magnitude lower than in voltage mode (Figure 4). The stimulation efficacy in current and voltage mode is also depending on the stimulation buffer implementation[23].

We then compared different electrode configurations, which provided increased electric field strengths, as compared to using a single electrode against a global reference electrode in solution. As shown in Figure 5D, the stimulation efficacy, however, was found to be in the same range for different neurons.

Capitalizing on the short artifact duration upon using current mode, we finally studied neuron stimulability during cell development and growth. Our hypothesis was that the AIS development over time would increase neuron stimulability. We combined live stainings and electrical recordings/stimulation to follow neuronal development over several days. The most challenging procedure during the experiments was to identify more or less isolated neurons on the array and in the culture and to then track them over several days during the experiments. Several neurons had to be discarded as a consequence of cell death during the experiments or

because we could not track them over the experiment time. Nevertheless, we observed a decrease in stimulation amplitudes to evoke APs, which was correlated to AIS growth in length (Figure 6).

In summary, this work presents a comprehensive study on electrical stimulation with microelectrodes of HD-MEAs and shows ways to realize single-neuron stimulation. Selecting optimal stimulation parameters could prove to be powerful for other *in vitro* applications, such as the control of neural-network bursting through electrical stimulation[42], or for *ex vivo* stimulations, for example, in retinal preparations or brain slices. We think that *in vivo* stimulation methods (epiretinal implants) could also benefit from findings of this paper in order to implement targeted stimulation of individual neurons. The delivered charges to depolarize neuronal membranes amounted to 0.02 pC/μm² with our HD-MEA, while, for example, retinal implants currently work with 3.5 pC/μm²[43]. A small size of electrodes and their dense packing may prove beneficial to stimulate neurons and could improve stimulation accuracy of prosthetic implants while enabling lower power consumption.

2.6 Acknowledgements

2.7 Author Contributions

Experimental design was performed by SR, MF, JM, VV, UF, AH; SR and CM performed experiments and data analysis; technical support was provided by MF, JM, VV; SR and AH wrote the manuscript; MF, CM, VV, JM and UF reviewed the manuscript; the project supervision was coordinated by AH.

2.8 Conflict of Interest

MF, JM and UF are co-founders of MaxWell Biosystems AG, which commercializes HD-MEA technology. All other authors declare no competing financial interests.

2.9 References

[1] F. Rattay, *Neuroscience* **1999**, *89*, 335.

[2] D. R. Merrill, *Implantable Neural Prostheses 2*, Springer New York, New York, NY, **2010**.

[3] S. S. Kumar, J. Wülfing, S. Okujeni, J. Boedecker, M. Riedmiller, U. Egert, *PLOS Comput. Biol.* **2016**, *12*, e1005054.

[4] J. Wülfing, S. S. Kumar, J. Boedecker, M. Riedmiller, U. Egert, *Proc. ESANN 2018* **2018**.

[5] A. L. Benabid, S. Chabardes, J. Mitrofanis, P. Pollak, *Lancet Neurol.* **2009**, *8*, 67.

[6] J. S. Perlmutter, J. W. Mink, *Annu. Rev. Neurosci.* **2006**, *29*, 229.

[7] G. S. Brindley, W. S. Lewin, *J. Physiol.* **1968**, *196*, 479.

[8] V. H. Fan, L. E. Grosberg, S. S. Madugula, P. Hottowy, W. Dabrowski, A. Sher, A. M. Litke, E. Chichilnisky, *J. Neural Eng.* **2019**, *16*, 025001.

[9] L. E. Grosberg, K. Ganesan, G. A. Goetz, S. S. Madugula, N. Bhaskhar, V. Fan, P. Li, P. Hottowy, W. Dabrowski, A. Sher, A. M. Litke, S. Mitra, E. J. Chichilnisky, *J. Neurophysiol.* **2017**, *118*, 1457.

[10] C. Sekirnjak, P. Hottowy, A. Sher, W. Dabrowski, A. M. Litke, E. J. Chichilnisky, *J. Neurosci.* **2008**, *28*, 4446.

[11] D. Tsai, S. Chen, D. A. Protti, J. W. Morley, G. J. Suaning, N. H. Lovell, *PLoS One* **2012**, *7*, e53357.

[12] R. V. Shannon, *Hear. Res.* **1983**, *11*, 157.

[13] R. V. Shannon, *Hear. Res.* **1985**, *18*, 135.

[14] M. Armenta Salas, L. Bashford, S. Kellis, M. Jafari, H. Jo, D. Kramer, K. Shanfield, K. Pejsa, B. Lee, C. Y. Liu, R. A. Andersen, *Elife* **2018**, *7*, e32904.

[15] S. Raspopovic, M. Capogrosso, F. M. Petrini, M. Bonizzato, J. Rigosa, G. Di Pino, J. Carpaneto, M. Controzzi, T. Boretius, E. Fernandez, G. Granata, C. M. Oddo, L. Citi, A. L. Ciancio, C. Cipriani, M. C. Carrozza, W. Jensen, E. Guglielmelli, T. Stieglitz, P. M. Rossini, S. Micera, *Sci. Transl. Med.* **2014**, *6*, 222ra19.

[16] E. A. Woodson, L. A. J. Reiss, C. W. Turner, K. Gfeller, B. J. Gantz, in *Cochlear*

Implant. Hear. Preserv., KARGER, Basel, **2009**, pp. 125–134.

[17] G. Dagnelie, *Curr. Opin. Neurol.* **2012**, *25*, 67.

[18] *Greenberg_2018.Pdf*, **n.d.**

[19] M. E. J. Obien, K. Deligkaris, T. Bullmann, D. J. Bakkum, U. Frey, *Front. Neurosci.* **2015**, *8*, 423.

[20] C. A. Thomas Jr, P. A. Springer, G. E. Loeb, Y. Berwald-Netter, L. M. Okun, *Exp. Cell Res.* **1972**, *74*, 61.

[21] Y. Ahmadian, A. M. Packer, R. Yuste, L. Paninski, *J. Neurophysiol.* **2011**, *106*, 1038.

[22] D. A. Wagenaar, J. Pine, S. M. Potter, *J. Neurosci. Methods* **2004**, *138*, 27.

[23] M. Ballini, J. Muller, P. Livi, Yihui Chen, U. Frey, A. Stettler, A. Shadmani, V. Viswam, I. Lloyd Jones, D. Jackel, M. Radivojevic, M. K. Lewandowska, Wei Gong, M. Fiscella, D. J. Bakkum, F. Heer, A. Hierlemann, *IEEE J. Solid-State Circuits* **2014**, *49*, 2705.

[24] L. Berdondini, K. Imfeld, A. Maccione, M. Tedesco, S. Neukom, M. Koudelka-Hep, S. Martinoia, *Lab Chip* **2009**, *9*, 2644.

[25] G. Bertotti, D. Velychko, N. Dodel, S. Keil, D. Wolansky, B. Tillak, M. Schreiter, A. Grall, P. Jesinger, S. Rohler, M. Eickenscheidt, A. Stett, A. Moller, K.-H. Boven, G. Zeck, R. Thewes, in *2014 IEEE Biomed. Circuits Syst. Conf. Proc.*, IEEE, **2014**, pp. 304–307.

[26] B. Eversmann, M. Jenkner, F. Hofmann, C. Paulus, R. Brederlow, B. Holzapfl, P. Fromherz, M. Merz, M. Brenner, M. Schreiter, R. Gabl, K. Plehnert, M. Steinhauser, G. Eckstein, D. Schmitt-landsiedel, R. Thewes, **2003**, *38*, 2306.

[27] U. Frey, J. Sedivy, F. Heer, R. Pedron, M. Ballini, J. Mueller, D. Bakkum, S. Hafizovic, F. D. Faraci, F. Greve, K.-U. Kirstein, A. Hierlemann, *IEEE J. Solid-State Circuits* **2010**, *45*, 467.

[28] D. Tsai, D. Sawyer, A. Bradd, R. Yuste, K. L. Shepard, *Nat. Commun.* **2017**, *8*, 1802.

[29] V. Viswam, J. Dragas, A. Shadmani, Y. Chen, A. Stettler, J. Muller, A. Hierlemann, in *2016 IEEE Int. Solid-State Circuits Conf.*, IEEE, **2016**, pp. 394–396.

[30] M. Radivojevic, D. Jäckel, M. Altermatt, J. Müller, V. Viswam, A. Hierlemann, D. J. Bakkum, *Sci. Rep.* **2016**, *6*, 31332.

[31] D. J. Bakkum, M. E. J. Obien, M. Radivojevic, D. Jäckel, U. Frey, H. Takahashi, A. Hierlemann, *Adv. Biosyst.* **2018**, *1800308*, 1800308.

[32] P. Hottowy, A. Skoczeń, D. E. Gunning, S. Kachiguine, K. Mathieson, A. Sher, P. Wiącek, A. M. Litke, W. Dąbrowski, *J. Neural Eng.* **2012**, *9*, 066005.

[33] M. S. Grubb, J. Burrone, *Nature* **2010**, *465*, 1070.

[34] D. N. Hill, S. B. Mehta, D. Kleinfeld, *J. Neurosci.* **2011**, *31*, 8699.

[35] W. Franks, I. Schenker, P. Schmutz, A. Hierlemann, *IEEE Trans. Biomed. Eng.* **2005**, *52*, 1295.

[36] A. Héduit, I. Quinio, D. Stadmuller, D. R. Thévenot, *Water Sci. Technol.* **1996**, *34*, 143.

[37] N. Joye, A. Schmid, Y. Leblebici, in *2008 30th Annu. Int. Conf. IEEE Eng. Med. Biol. Soc.*, IEEE, **2008**, pp. 559–562.

[38] N. Joye, A. Schmid, Y. Leblebici, *Neurocomputing* **2009**, *73*, 250.

[39] K. B. Oldham, *J. Electroanal. Chem.* **2008**, *613*, 131.

[40] P. Sharma, T. S. Bhatti, *Energy Convers. Manag.* **2010**, *51*, 2901.

[41] J. D. Weiland, D. J. Anderson, M. S. Humayun, *IEEE Trans. Biomed. Eng.* **2002**, *49*, 1574.

[42] D. A. Wagenaar, *J. Neurosci.* **2005**, *25*, 680.

[43] A. K. Ahuja, J. Yeoh, J. D. Dorn, A. Caspi, V. Wuyyuru, M. J. McMahon, M. S. Humayun, R. J. Greenberg, L. DaCruz, Argus II Study Group, *Transl. Vis. Sci. Technol.* **2013**, *2*, 1.

2.10 Supplementary Material

Voltage stimulation

Injected charge

Current stimulation

Injected charge

Resulting voltage
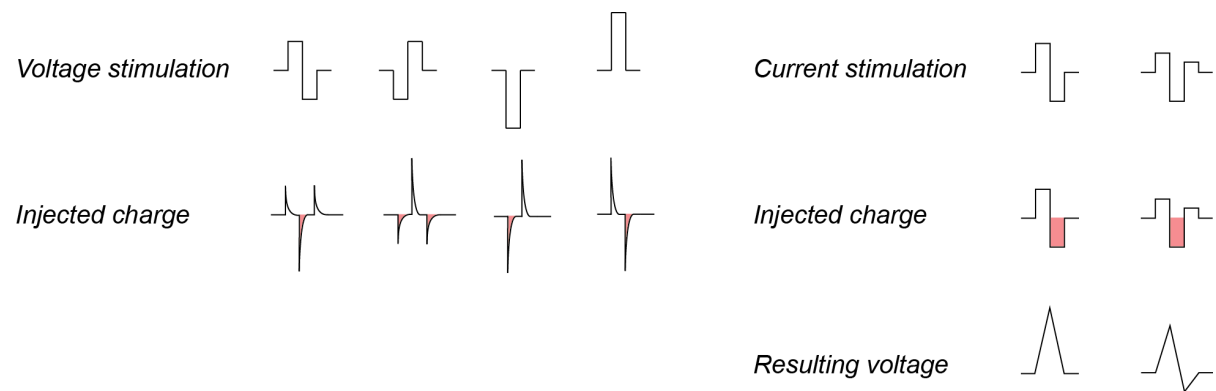
Figure S1. Stimulation pulses used for voltage (left) and current (right) mode are shown in the top row. Below a representation of the injected charges in voltage (left) and current (right) mode. The negative charge that evokes APs is displayed in red. In voltage mode, the charge features exponential decays and is a function of the electrode impedance, while it stays constant in current mode.
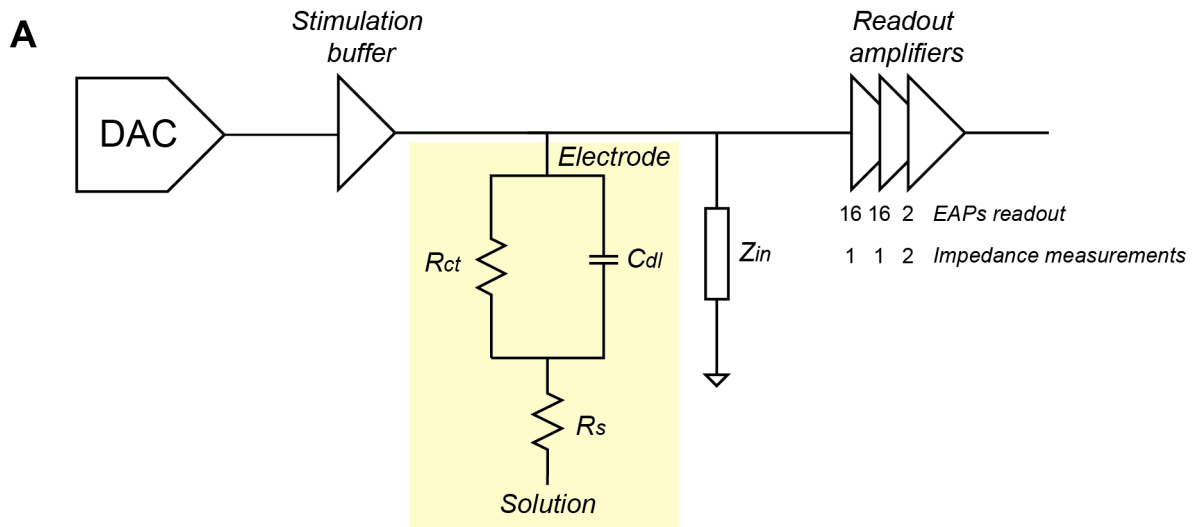
Figure S2. Equivalent circuit model of the stimulation and readout channel. In yellow, the electrode equivalent circuit including the double-layer capacitance C_{dl} and the charge transfer resistance R_{ct} is shown along with the solution resistance R_s. Z_{in} represents the input resistance to the readout amplifiers. To read out extracellular APs, a gain of 512 was used (3 gain stages: 16×16×2). For impedance measurements, instead, the first two amplifier stages were bypassed, while the third one was set to a gain of 2. The low gain enabled a voltage readout on the stimulation electrode.
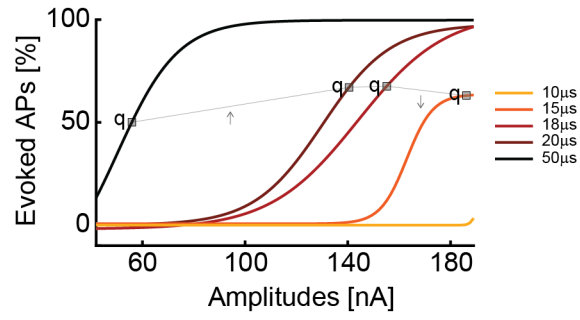
Figure S3. Activation curves as a result of current stimulation with a biphasic waveform. The label *q* indicates the points, where the delivered overall charge is the same. While the efficacy is almost the same for 20 and 18 μs phase duration, for 15 μs it starts to decrease. This behavior can be explained with the fact that the stimulation buffers cannot efficiently deliver signals of very short duration.
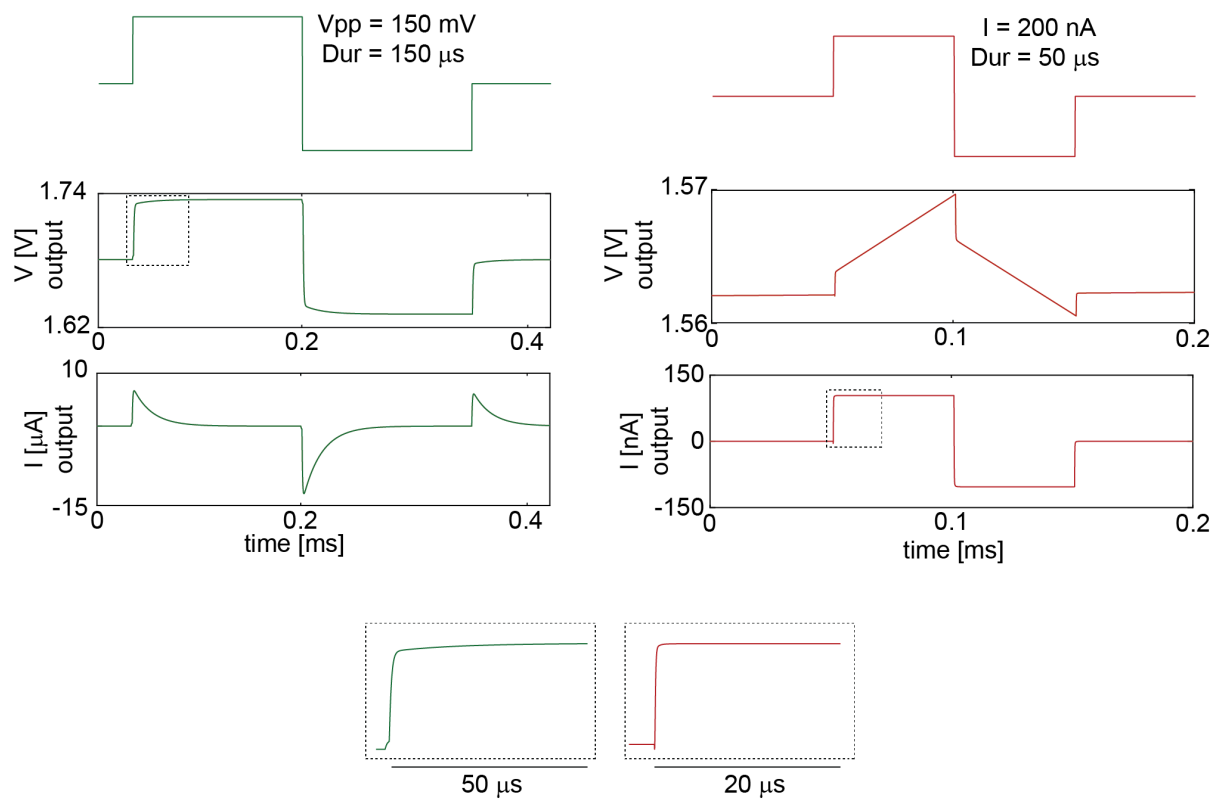
Figure S4. Simulated voltage (green) and current (red) output signals of the stimulation buffers. The settling time of the stimulation buffers in voltage mode is ~50 µs to reach the applied voltage value, while in current mode, the applied value is reached almost instantaneously. The difference is due to the different stimulation buffers' design. The simulations were performed considering an equivalent electrode model with C_{dl} = 1.5 nF, R_{ct} = 100 MΩ and R_s = 10 kΩ.
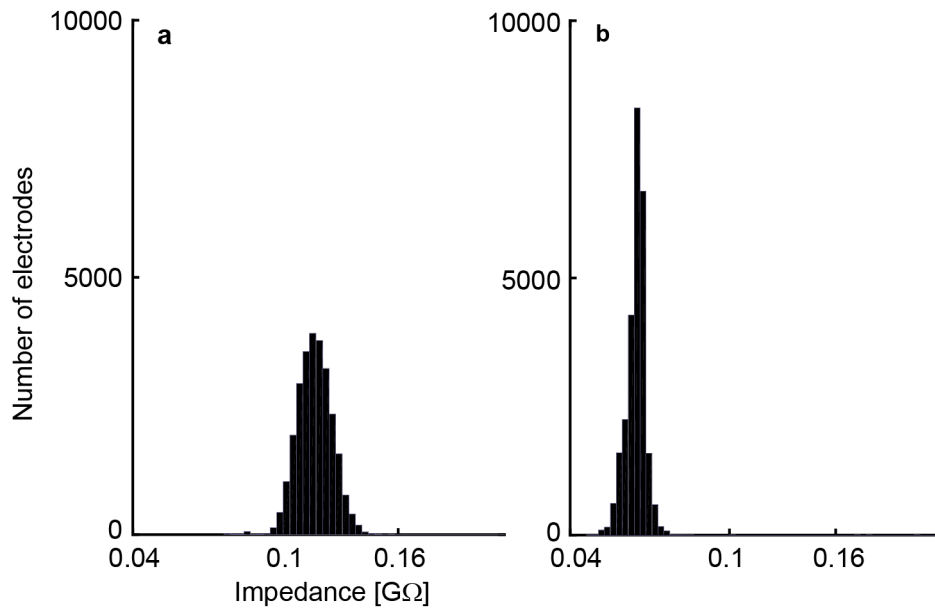
Figure S5. Histograms of the impedance distribution of all 26'400 electrodes to demonstrate the impedance homogeneity (a bright Pt, b Pt-black). A sinusoidal waveform was used for stimulation.
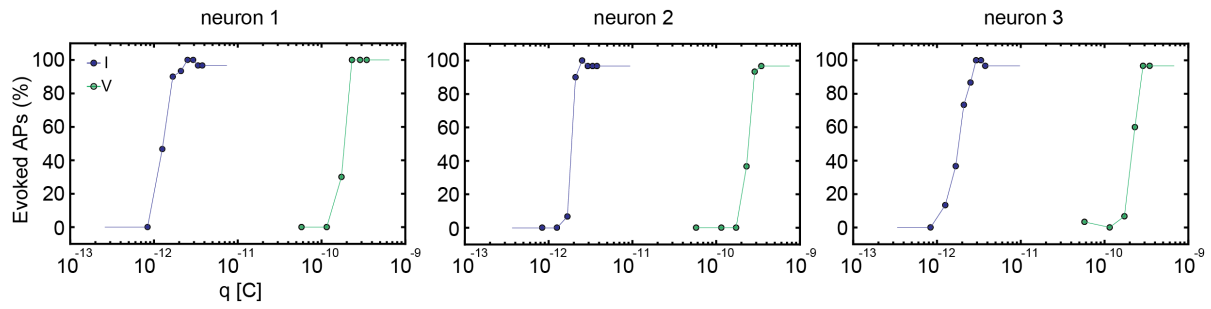
Figure S6. Charges required for efficient voltage and current stimulation of three different neurons. For current stimulation, the waveform had a duration of 20 µs per phase, while it was 100 µs per phase for voltage stimulation. The stimulation protocol included 30 repetitions of every stimulation-signal amplitude in a randomized manner.
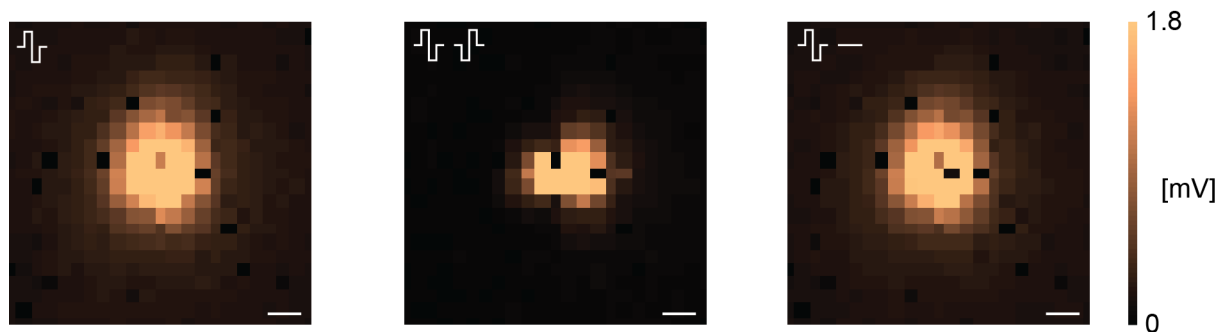
Figure S7. Recordings from high-density blocks of electrodes to compare the stimulation artifact spread in cell-culture medium. Three configurations were used: one stimulation electrode against a global reference electrode in solution (left), two neighboring electrodes with opposite-sign waveforms (center), and one stimulation electrode, while the neighboring electrode was grounded (right). The configuration with two electrodes delivering waveforms of opposite signs seemingly produced the smallest artifact on the array. The artifact was computed as the peak-to-peak voltage readout of every electrode. The measurements were done in growth medium. The voltage stimulation amplitude was 140 mV, and the duration 100 µs per phase. N=1. Scale bar 50 µm.
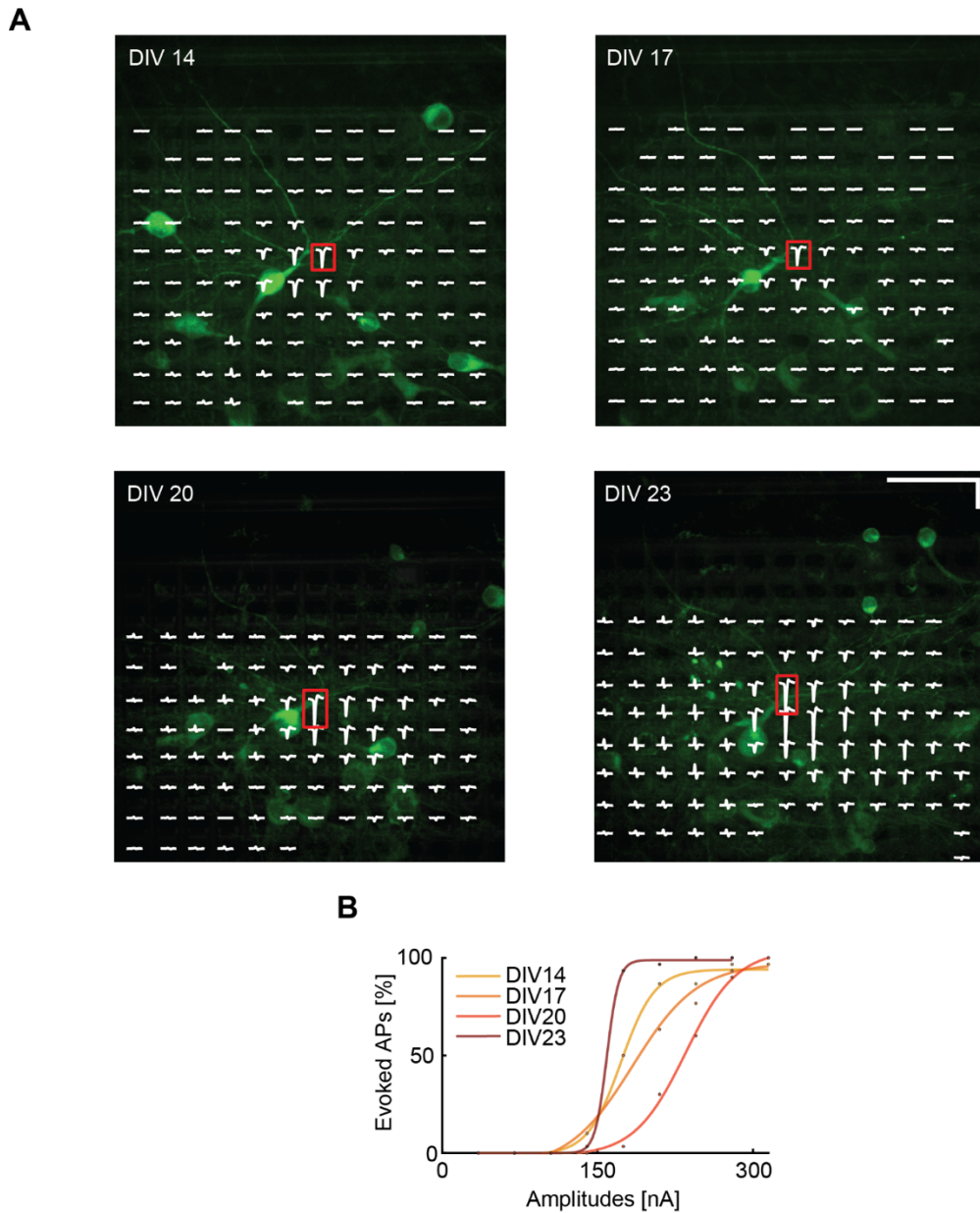
Figure S8. (A) Superimposed fluorescence image and electrical footprint of another neuron at DIVs 14, 17, 20, 23. This neuron significantly moved during the initial measurements between DIVs 14 and 20 so that the stimulation threshold increased. The stimulation electrodes used for the analysis are indicated with a red box. The stimulation electrode remained the same during the whole experiment. The signals recorded on the different electrodes are displayed in white (electrical footprint). Horizontal scale bar: 50 µm, vertical scale bar: 250 µV. **(B)** Current stimulation activation curves of the neuron in A over time (DIVs). The stimulation efficacy varied and increased between DIV 20 and 23. The initial decrease is due to neuron movement.

3 ELECTROPHYSIOLOGICAL PHENOTYPE CHARACTERIZATION OF HUMAN iPSC-DERIVED NEURONAL CELL LINES BY MEANS OF HIGH-DENSITY MICROELECTRODE ARRAYS

Silvia Ronchi[1*], Alessio Paolo Buccino[1], Gustavo Prack[1], Sreedhar Saseendran Kumar[1], Manuel Schröter[1], Michele Fiscella[1,2] and Andreas Hierlemann[1]

[1]Department of Biosystems Science and Engineering, ETH Zürich, Basel, Switzerland
[2]MaxWell Biosystems AG, Zurich, Switzerland

* Correspondence:
Silvia Ronchi
silvia.ronchi@bsse.ethz.ch
Michele Fiscella
michele.fiscella@mxwbio.com

3.1 Abstract

Recent advances in the field of cellular reprogramming have opened a route to studying the fundamental mechanisms underlying common neurological disorders. High-density microelectrode-arrays (HD-MEAs) provide unprecedented means to study neuronal physiology at different scales, ranging from network through single-neuron to subcellular features. In this work, we used HD-MEAs *in vitro* to characterize and compare human induced-pluripotent-stem-cell (iPSC)-derived dopaminergic and motor neurons, including isogenic neuronal lines modeling Parkinson's disease and amyotrophic lateral sclerosis. We established reproducible electrophysiological network, single-cell and subcellular metrics, which were used for phenotype characterization and drug testing. Metrics, such as burst shape and axonal velocity, enabled the distinction of healthy and diseased neurons. The HD-MEA metrics could also be used to detect the effects of dosing the drug retigabine to human motor neurons. Finally, we showed that the ability to detect drug effects and the observed culture-to-culture variability critically depend on the number of available recording electrodes.

3.2 Introduction

The advent of efficient cellular reprogramming protocols has revolutionized stem cell research and enabled access to a large variety of human cell lines[1]. Induced-pluripotent-stem-cell (iPSC)-technology has been used to establish 2D and 3D human cell and tissue models[2] and to study organ genesis for, e.g., liver[3], lungs[4], heart[5] and brain[6]. Today, iPSC technology allows to obtain cells and tissue samples from both, healthy individuals and patients and to develop *in-vitro* disease models[7]. Genetically-defined human iPSC-derived neurons have been generated to investigate physiological aspects and mechanisms underlying common neurological disorders[8] and for usage in *in-vitro* platforms for systematic drug testing[9,10].

Functional phenotype characterization and drug-effect assessment of human neurons can be performed *in vitro* by using optical methods (e.g., calcium imaging[11]), patch-clamp techniques[12], or by using microelectrode arrays (MEAs)[13]. MEAs feature a set of metal electrodes to record electrical activity simultaneously from several hundreds to thousands of cells and have been used to study brain disorders and to detect differences between normal and pathological conditions[14,15].

Passive MEA devices[16–18] without active circuit elements feature 10-100 electrodes per mm^2 and have been used to electrically characterize human neuronal phenotypes[9,10,14]. Complementary-metal-oxide-semiconductor (CMOS)-based high-density microelectrode

arrays (HD-MEAs)[19–24] feature active circuit elements and electrode densities of tens to thousands of electrodes per mm^2 and have been used in first experiments to characterize electrical properties of healthy human iPSC-derived neurons[25]. However, to the best of our knowledge, CMOS-based HD-MEAs have not been yet used to comprehensively characterize and compare electrical phenotypes of human neuronal line across scales including network, single-neuron and subcellular features and to assess the effects of neurological disorders.

Among neurodegenerative disorders, Parkinson's disease and amyotrophic lateral sclerosis have been extensively studied by using iPSC technology in order to understand basic disease mechanisms at molecular and functional levels and for finding new cures[26–30].

Parkinson's disease (PD) is among the most common neurodegenerative diseases, with a prevalence increasing from 2.5 million patients in 1990 to 6.1 million patients in 2016[31], and projections indicating that more than 12 million people will be affected by 2050[31]. PD is characterized by the death of dopaminergic neurons within the *substantia nigra*, which causes progressive motor and cognitive dysfunctions, such as tremor, rigidity and dementia[32]. The distinctive hallmark of PD is the accumulation of intracellular α-synuclein, which forms protein inclusions, known as Lewy bodies and Lewy neurites[32]. Human iPSC-derived neurons modeling PD have been studied *in vitro* and showed compromised neuronal morphology[33], synaptic connectivity[34] and different electrophysiological characteristics including, e.g., the shape of action potential waveforms[35].

Amyotrophic lateral sclerosis (ALS) is a neurodegenerative disease, characterized by a progressive degeneration of upper and lower motor neurons, followed by muscle degeneration, paralysis, and respiratory failure[36]. ALS incidence is reported to be between 0.6 and 3.8 per 100'000 persons/year[37]. Human iPSC-derived neurons, developed to model ALS, featured an intrinsic membrane hyperexcitability phenotype[10], which was used to test compounds that lowered neurons' electrical hyperexcitability. The study of Wainger et al., which relied on 64 microelectrodes, placed at a pitch of 200 mm in a 12-well platform, led to clinical testing of retigabine in human patients[10].

Combining human iPSC-derived neurons with large-scale electrophysiological techniques, such as HD-MEAs, provides a powerful and scalable platform to study neurological disease mechanisms and offers the potential to assess disease-induced phenotypic alterations.

Here, we used CMOS-based high-density microelectrode arrays (HD-MEAs) to characterize and compare the electrical phenotypes of four iPSC-derived neuronal cell lines: human dopaminergic neurons (hDNs), dopaminergic neurons carrying the A53T α-synuclein mutation, linked to PD (hDNs-PD), motor neurons (hMNs), and motor neurons carrying the

TDP-43 Q331K mutation, linked to ALS (hMNs-ALS). We found significant functional phenotype differences across the studied iPSC lines at different spatiotemporal scales, ranging from network level to characteristics of individual axons. We then used HD-MEA-based readouts to quantify the effect of the drug retigabine on motor neurons (hMNs)[10,38] and we showed that high-spatiotemporal-resolution sampling of neuronal activity by means of HD-MEAs provides very reproducible readouts in assessing the effects of neuroactive compounds.

3.3 Results

3.3.1 Human iPSC-derived neurons develop spontaneous activity on HD-MEA chips

Before probing the developing neurons and neuronal networks, we confirmed the presence of characteristic cell-type specific neuronal markers for each iPSC line. Human iPSC-derived and rat primary neuronal cultures, used for benchmarking, showed electrical activity across the entire HD-MEA chip electrode area (**Figure 1a**). The electrically active areas contained mature neurons as confirmed by microscope imaging of MAP2-positive cells (Figure 1b). The presence of astrocytes in the cell cultures was confirmed immunohistochemically by GFAP[39,40] and S100-β[40] staining (Figure 1c). An anti-GFAP antibody was used as a reactive astrocyte marker for rat primary cultures, which underwent the isolation procedure. An anti-S100-β antibody was used as astrocyte marker for human cell lines, as its efficiency was already demonstrated with human lines[41]. Furthermore, we visualized motor and dopaminergic neurons on the HD-MEA chips using the motor-neuron marker SMI-32[39] (Figure 1c, central panel) and the dopaminergic-neuron marker TH[42] (Figure 1c, right panel). Human and rat neurons were all electrically active and showed spontaneous action-potential signals, which systematically crossed the detection threshold (Figure 1d).
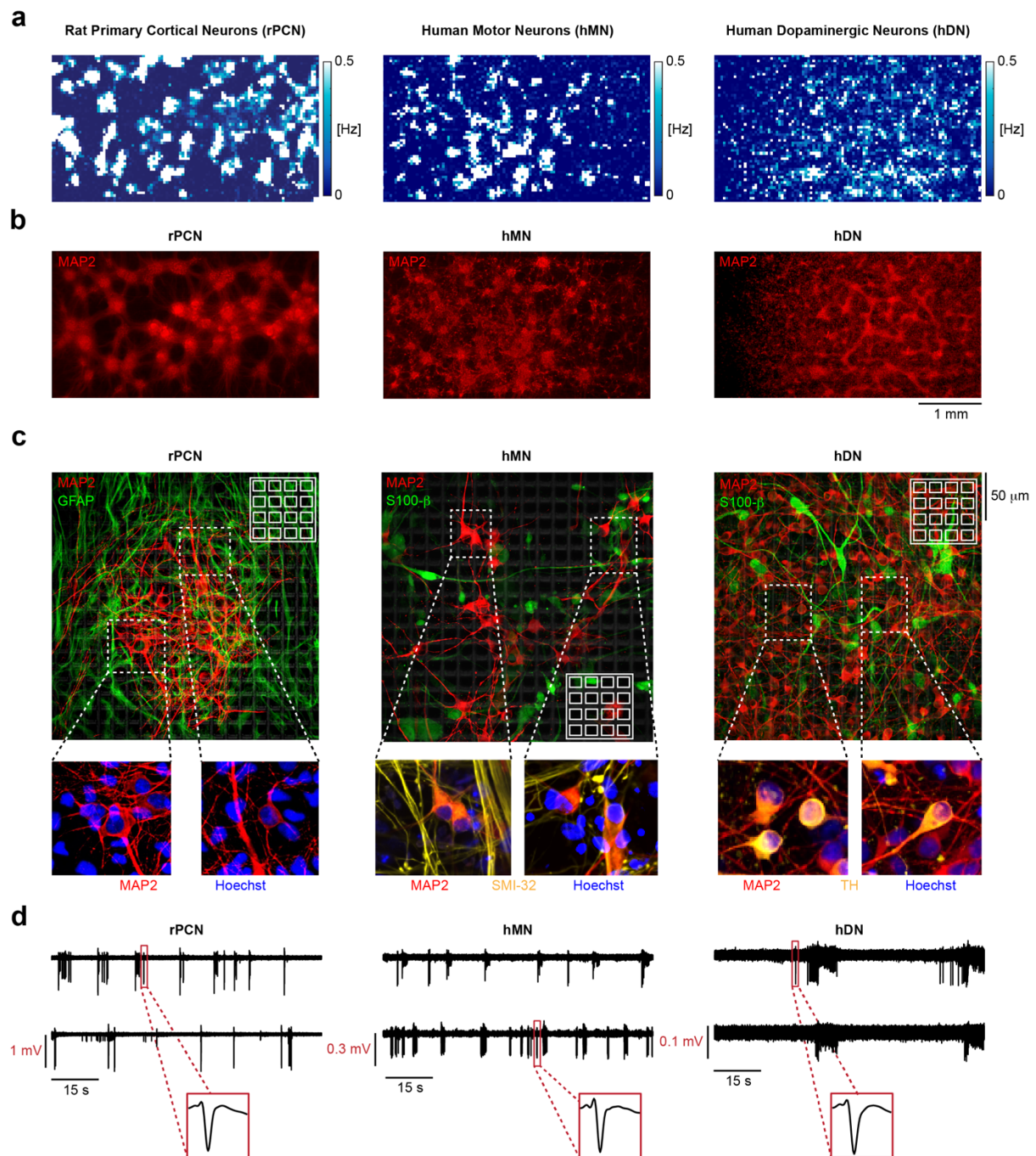
Figure 1. Electrical and optical imaging of neuronal cultures. (a) HD-MEA electrical image showing 2D spatial distribution maps of the electrode firing rate (eFR, see Methods, *HD-MEA Metrics*) as recorded across the entire HD-MEA chip surface from 6'600 electrodes at DIV 21, for rat primary cortical neurons (rPCNs), human motor neurons (hMNs) and human dopaminergic neurons (hDNs). **(b)** Microscope image of MAP-2 positive (red) stained neurons on HD-MEA chips. Cells were fixed and stained on the HD-MEA chips at DIV 21. **(c)** Cell-type specific stainings of cultures on HD-MEA chips shown in Figure 1b. Cell nuclei are shown in blue (Hoechst positive), motor neurons (SMI-32 positive) and dopaminergic neurons (TH positive) in yellow, astrocytes (GFAP, S100-β positive) in green. White insets with rectangles and grids schematically represent electrode sizes and spacing. **(d)** Example voltage traces showing extracellular action potentials (spikes) recorded by two electrodes at DIV 21. The displayed traces are taken from electrodes recording action potentials with comparably large

amplitudes. A close-up of an averaged action potential waveform is displayed in the red rectangles. Left panel: rat primary cortical neurons. Central panel: human motor neurons. Right panel: human dopaminergic neurons.

3.3.2 Electrical phenotype characterization of human iPSC-derived neurons across development

To compare the electrophysiological properties across the four human iPSC-derived neuronal cell lines, we first examined and compared the mean firing rate (MFR), mean spike amplitude (MSA), mean inter-spike interval (ISI) coefficient of variation (ISIcv) and the percentage of active electrodes (pAE). Changes in metrics as the firing rate are hallmarks of neuronal development[10], but they can also be indicative of a specific neuron type[43] or pathology[10]. We also compared the iPSC-derived cell lines electrophysiological properties with the ones of rat primary cortical neurons (rPCNs), the most commonly used neuronal cells in the MEA field and an established *in-vitro* culturing system, across development (for details, see **Figure S1**). Both, motor (hMN) and dopaminergic (hDN) neuronal lines showed a significant increase (7 fold and 1.9 fold) in the mean firing rate from DIV 7 to DIV 21 (**Figure 2a, 2b**), similar to rPCNs (Figure S1c).

hMNs featured a higher mean firing rate, mean spike amplitude and percentage of active electrodes compared to hDNs (Figure 2b). In particular, at DIV 21, the hMN mean firing rate $(1.98 \pm 1.30$ Hz) was 3.5 times higher $(p < 0.001$, Wilcoxon rank-sum test) than the hDN mean firing rate $(0.57 \pm 0.10$ Hz). The hMN mean spike amplitude and percentage of active electrodes were 1.5-fold and 1.7-fold higher than that of the hDN line (Figure 2b). However, the mean ISI coefficient of variation did not vary significantly across development between hMNs and hDNs, which showed a similar behavior in neuron-firing-rate evolution over development.

Both, hMNs and hDNs showed significantly lower mean spike amplitudes in comparison to rPCNs at DIV 21. rPCNs had an average mean spike amplitude of 95.01 ± 8.96 µV, whereas hMNs and hDNs featured mean spike amplitudes of 44.23 ± 14.62 µV and 29.17 ± 2.78 µV, respectively (Figure S1c and Figure 2b). Furthermore, the variation in the mean spike amplitude across development was less in hMNs and hDNs than that of rPCNs (Figure S1c and Figure 2b). Human iPSC-derived neuronal lines were also characterized by an almost constant ISI coefficient of variation across development, in contrast to the increase in rPCNs (Figure S1c and Figure 2b).
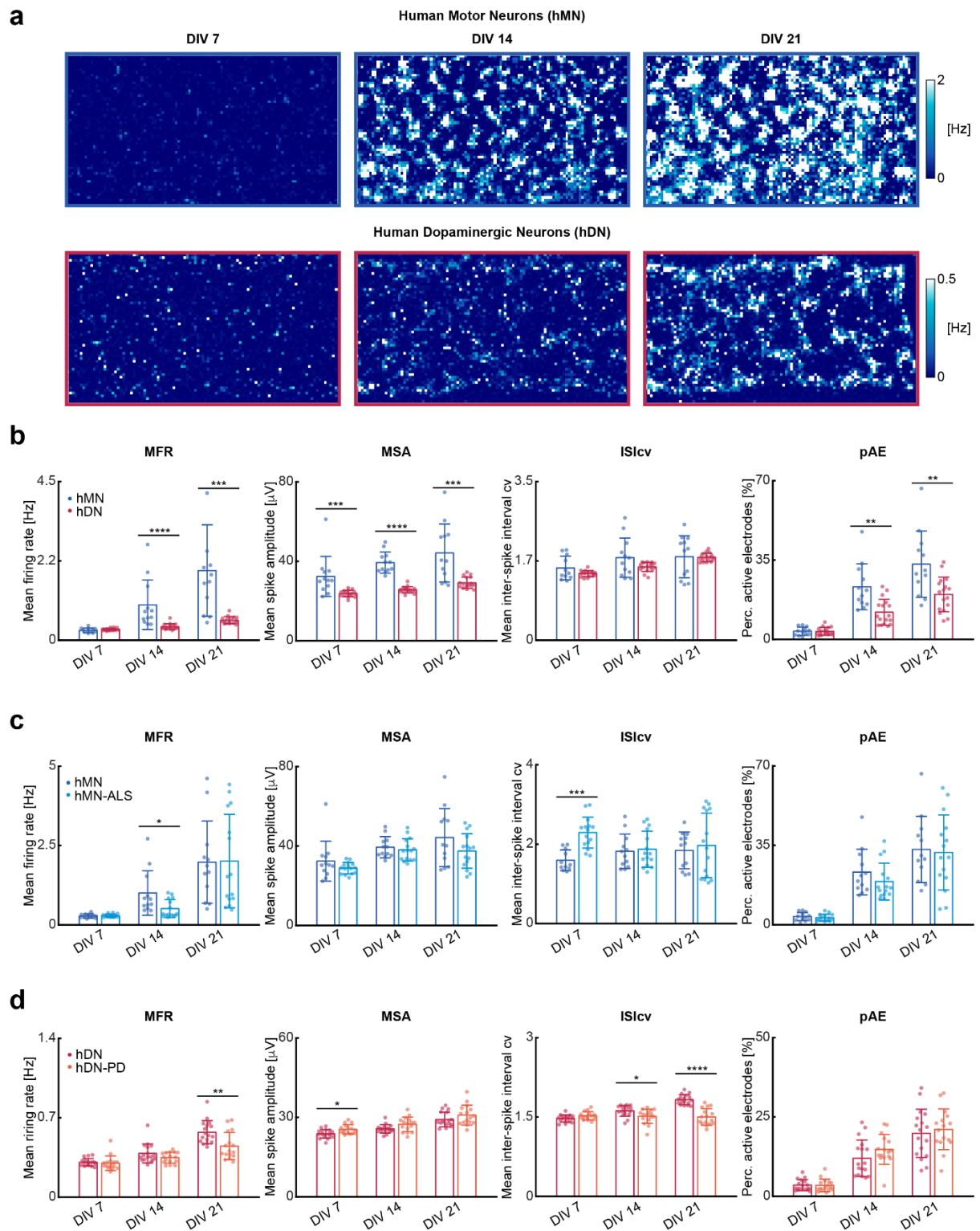
Figure 2. Electrical phenotype characterization of human iPSC-derived neurons across development. (a) Exemplary 2D spatial distribution maps (6'600 electrodes) of electrode firing rates for motor neurons (top) and dopaminergic neurons (bottom), at DIVs 7, 14 and 21, respectively. **(b)** Bar plots comparing the mean firing rate (MFR), mean spike amplitude (MSA), mean ISI coefficient of variation (ISIcv) and percentage of active electrodes (pAE) of 12 hMN cultures (blue) and 17 hDN cultures (red) at DIVs 7, 14 and 21. **(c)** Bar plots comparing the mean firing rate, mean spike amplitude, mean ISI coefficient of variation and percentage of active electrodes of 12 hMN cultures (blue) and 15 hMN-ALS cultures (light

71

blue) at DIVs 7, 14 and 21. **(d)** Bar plots comparing the mean firing rate, mean spike amplitude, mean ISI coefficient of variation and percentage of active electrodes of 17 hDN cultures (red) and 16 hDN-PD cultures (orange) at DIVs 7, 14 and 21. Each dot represents one HD-MEA or well. Bar heights indicate distribution mean values, and error bars indicate standard deviations. Pair-wise comparisons were carried out using the two-tailed Wilcoxon rank-sum test. The black stars indicate p values: * $p < 0.05$, ** $p < 0.01$, *** $p < 0.001$, **** $p < 0.0001$.

Comparing healthy (WT) and diseased (ALS) motor neuron lines, the hMN-ALS neuronal cells featured a 0.5-fold ($p < 0.05$) lower mean firing rate than hMNs at DIV 14 (Figure 2c). Similar results were found by comparing the two dopaminergic neuron lines, which showed a 0.8-fold ($p < 0.01$) lower mean firing rate of hDN-PDs in comparison to hDNs at DIV 21 (Figure 2d). Analysis of the mean spike amplitudes showed no significant differences between hMN and hMN-ALS neurons. In contrast, the two dopaminergic neuron lines, hDN and hDN-PD, showed significant differences in the mean spike amplitude at DIV 7 ($p < 0.05$) (Figure 2c). The mean ISI coefficient of variation evidenced a more regular firing of the hMN line at DIV 7 in comparison to the hMN-ALS line (Figure 2c). Conversely, the disease line hDN-PD featured a more regular firing at DIV 21 in comparison to the healthy hDN line (Figure 2d). Finally, by comparing the percentage of active electrodes across development, we did not find significant differences between hMN and hMN-ALS or hDN and hDN-PD lines; however, pAE data generally were very disperse, suggesting that potential differences in MFR between cell types could also be a consequence of the ability of the specific cell line to form functional neuronal networks (Figure 2b-d).

3.3.3 Network burst characterization of human iPSC-derived neurons across development

Neuronal networks are often characterized by synchronous activity (bursts), which may give rise to network oscillations[44]. These bursts emerge as a result of recurrent synaptic connections that form as neuronal networks mature. In primary cortical neurons, the bursts are often irregular even in mature networks[45,46] (**Figure S2**). The nature and properties of the associated oscillations may vary for different pathological conditions [47] or in co-cultures with different cell types[43].

Here, we assessed the characteristic properties of human healthy and diseased cell lines by using network-burst metrics including mean burst duration (BD), mean inter-burst interval (IBI), mean IBI coefficient of variation (IBIcv), number of bursts per minute (B$_{/min}$) and burst shape (see Methods, *HD-MEA Metrics*).

All human iPSC-derived neuronal cultures showed robust and reproducible network oscillations at DIV 14 and 21 (**Figure 3a**, Figure S2). hMNs and hDNs featured significant differences in IBI, IBIcv and $B_{/min}$ at both DIVs 14 and 21 (Figure 3b). hDNs featured a 2.4-fold increase (p < 0.0001, Wilcoxon rank-sum test) in time between consecutive bursts compared to hMNs at DIV 21 (Figure 3b). hDNs displayed more regular bursts than hMNs, which is shown by a 0.3-fold decrease (p < 0.001) in IBIcv between consecutive bursts at DIV 21 (Figure 3b). Furthermore, at DIV 21 hDNs showed in average 2.2-fold less bursts per minute (p < 0.0001) than hMNs (Figure 3b).

Comparing motor-neuron lines, we found that hMN-ALS neurons featured a longer burst duration of 16.56 ± 5.44 s than hMNs (3.91 ± 2.59 s) at DIV 21 (Figure 3c). Converse results were found for the healthy and isogenic diseased dopaminergic-neuron lines, where hDN-PDs showed a 0.5-fold decrease (p < 0.0001) of the burst duration at DIV 21 compared to hDNs (Figure 3d).

By comparing the inter-burst interval times of healthy and diseased lines at DIV 21, we found that the hMN-ALS line had a 3.2-fold longer IBI (p < 0.0001) than the healthy hMN line (Figure 3c), while the hDN-PD line showed a 0.6-fold shorter IBI (p < 0.0001) than the healthy hDN line (Figure 3d).

An analysis of the IBI coefficients of variation yielded no significant differences between hMN and hMN-ALS lines (Figure 3c). However, the dopaminergic neuron lines showed a small difference at DIV 21 (p < 0.05) (Figure 3d).

Comparing the number of bursts per minute recording ($B_{/min}$) of healthy and diseased lines, we found that hMNs featured a 3-fold higher (p < 0.0001) number of bursts per minute than hMN-ALSs at DIV 21 (Figure 3c). Instead, hDNs featured a 0.62-fold lower (p < 0.0001) number of bursts per minute than the diseased line at DIV 21 (Figure 3d).

Figure 3. Network burst characterization of human iPSC-derived neurons across development. **(a)** Population spike time histograms simultaneously recorded by 1'024 electrodes from hMN (blue), hMN-ALS (light blue), hDN (red) and hDN-PD (orange) neurons at DIV 21. **(b)** Bar plots comparing mean burst duration (BD), mean inter-burst interval (IBI), mean IBI coefficient of variation (IBIcv) and bursts/min ($B_{/min}$) of 9 hMN cultures (blue) and 18 hDN cultures (red) at DIVs 14 and DIV 21. Each dot represents one HD-MEA or well. **(c)** Bar plots comparing mean burst duration, mean IBI, mean IBI coefficient of variation and bursts/min of 9 hMN cultures (blue) and 10 hMN-ALS cultures (light blue) at DIV 14 and DIV 21. Each dot represents one HD-MEA or well. **(d)** Bar plots comparing mean burst duration, mean IBI, mean IBI coefficient of variation and bursts/min of 18 hDN cultures (red) and 16 hDN-PD cultures (orange) at DIV 14 and DIV 21. Each dot represents one HD-MEA or well. Bar heights indicate distribution mean values, and error bar indicate standard deviations. Pairwise comparisons were carried out using the two-tailed Wilcoxon rank-sum test. The black stars indicate p values: * $p < 0.05$, ** $p < 0.01$, *** $p < 0.001$, **** $p < 0.0001$.

3.3.4 Network-burst shape can be used to characterize human iPSC-derived neurons lines

By inspecting the population spike time histograms (**Figure 4a**), we noticed that each human iPSC-derived neuronal line featured a characteristic burst shape across every activity peak (see also Figure S2). Therefore, we assessed the ability to discriminate hMN and hMN-ALS or hDN and hDN-PD neurons by their network burst shape at a given day *in vitro*. For this purpose, we computed the linear correlations between every single recorded network burst and the corresponding *network burst templates* generated by averaging over many electrodes and HD-MEAs or wells harboring the same cell line at the specific DIV (see Methods, *HD-MEA Metrics*). In Figure 4b, we show the network burst template for hMNs at DIV 14 and DIV 21 (see Methods, *HD-MEA Metrics*). When we linearly correlated single recorded hMN bursts at DIV 14 to the DIV14 hMN template, we obtained an average Pearson Correlation Coefficient (PCC) of 0.97 ± 0.01, which indicated a high similarity between the burst template and the single bursts. However, upon correlating single DIV14 hMN-ALS bursts to the DIV14 hMN template, the average PCC decreased to 0.89 ± 0.06 (Figure 4b) and to 0.71 ± 0.12 for correlating DIV21 hMN-ALS bursts to the DIV21 hMN template (Figure 4b).

In Figure 4d, we used the network burst templates of hDNs at DIVs 14 and 21. The DIV 14 hDN template yielded an average Pearson Correlation Coefficient (PCC) of 0.98 ± 0.01 upon application to single hDN recorded bursts at DIV 14. Upon using the DIV14 hDN template for single hDN-PD bursts recorded at DIV 14, the average Pearson Coefficient decreased to 0.96 ± 0.03 ($p < 0.001$, Wilcoxon rank-sum test) (Figure 4d). At DIV 21, the application of the DIV21 hDN template for DIV21 hDN-PD bursts yielded a further decreased PCC of 0.89 ± 0.03 (Figure 4d).

In Figure 4c and 4e, the inverse correlations by using the hMN-ALS and hDN-PD disease line templates are shown. Expectedly, the correlations are stronger between the disease-line templates and the respective disease line bursts at both DIVs as compared to bursts of the healthy lines. As the disease lines featured a somewhat larger burst shape irregularity, the discrimination by using the disease line templates was less efficient in comparison to the healthy line templates.
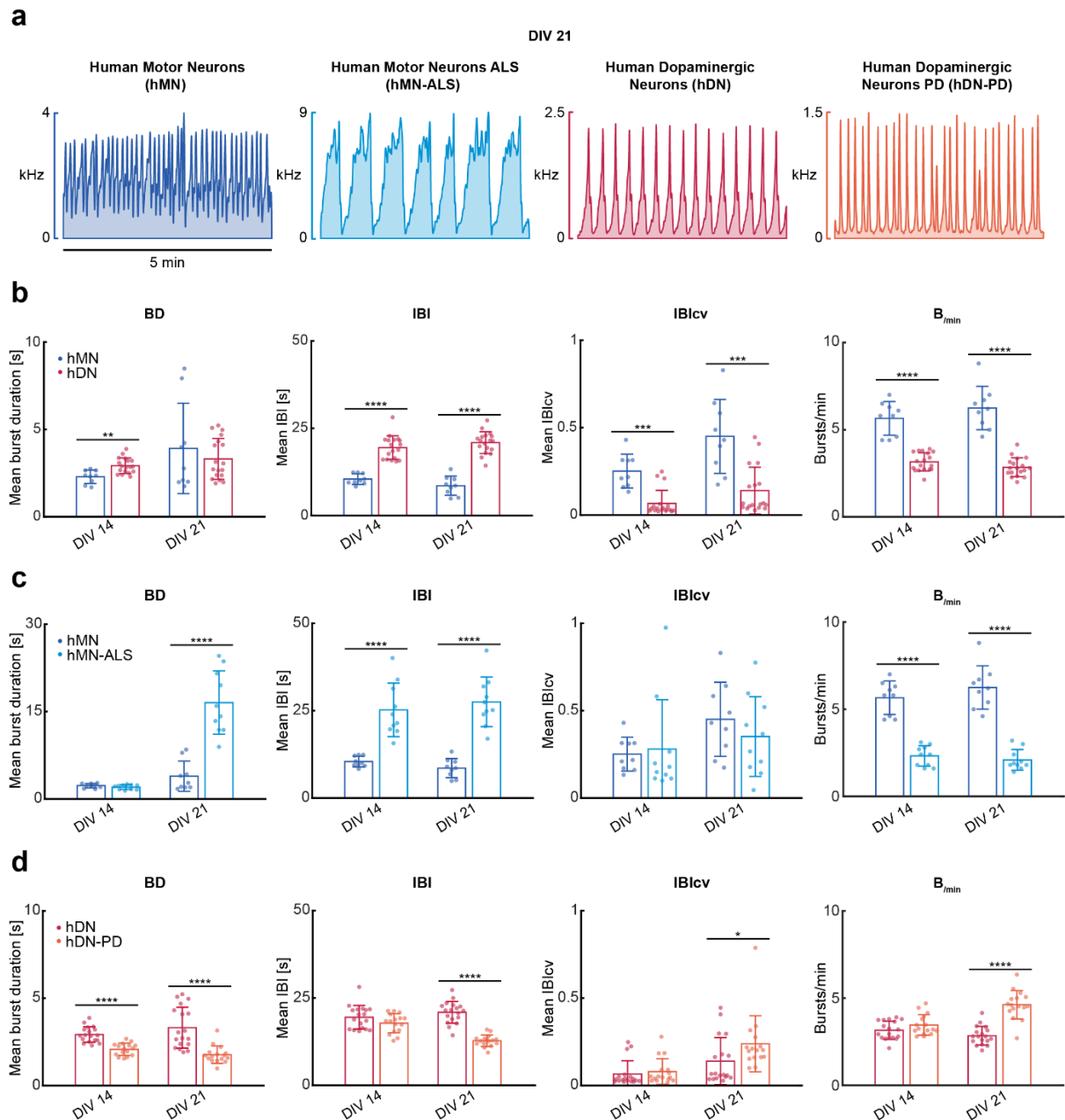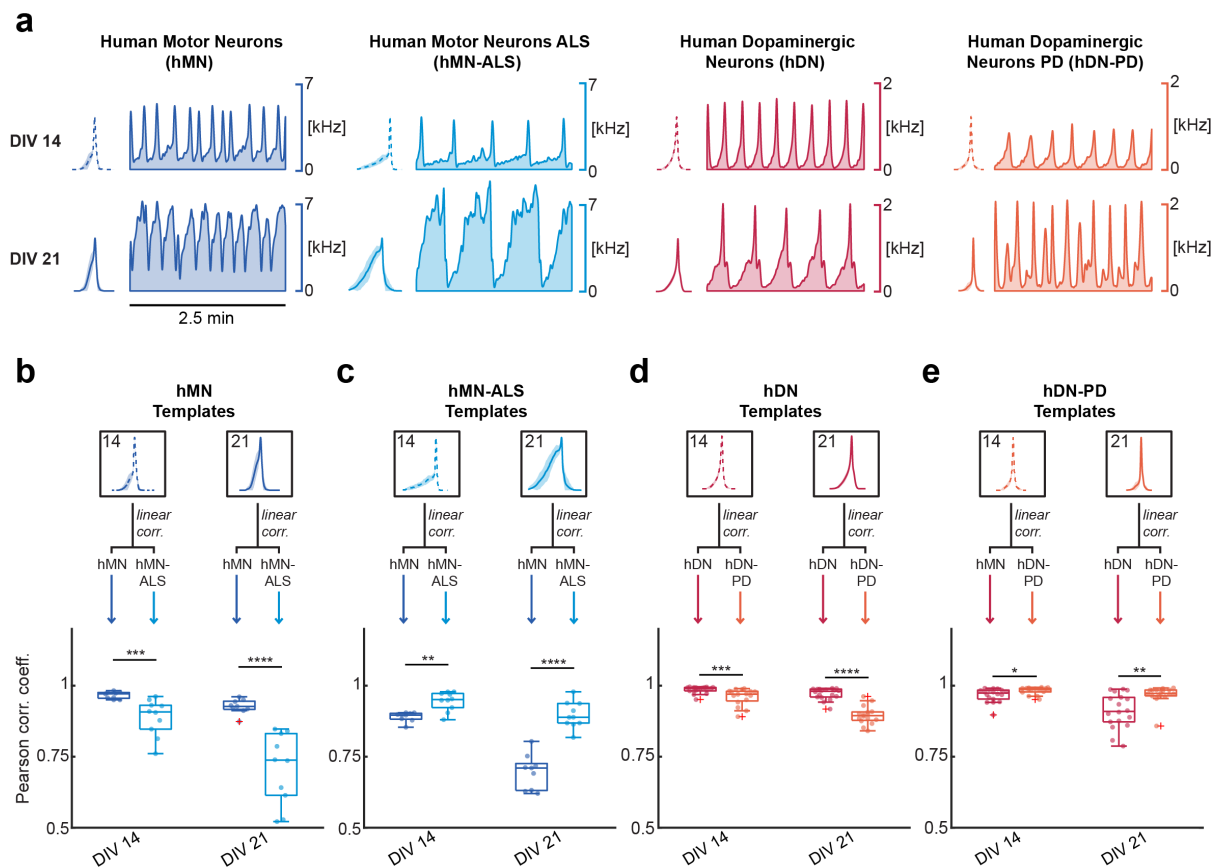
Figure 4. Network burst-shape characterization of human iPSC-derived neurons across development. (a) Population spike time histograms simultaneously recorded by 1'024 electrodes from (from left to right) hMN (blue), hMN-ALS (light blue), hDN (red), hDN-PD (orange) neurons at DIV 14 (top) and DIV 21 (bottom). At the left of each panel, an average network burst template is shown for the specific DIV and related neuronal cell type. **(b)** Bar plots comparing the Pearson Correlation Coefficient (PCC) upon linearly correlating the recorded network bursts to the corresponding average templates represented in the top panel. The graph represents the PCC upon linearly correlating burst of healthy motor neurons (N=9) and ALS motor neurons (N=10) to the template obtained from the healthy motor neurons at DIVs 14 and 21. Each dot represents one HD-MEA or well. Box plots indicate distribution mean value and standard deviation. **(c)** PCCs for correlating the hMN-ALS template to bursts of hMN (N=9) and hMN-ALS (N=10) lines. **(d)** PCCs for correlating the hDN template to burst of hDN (N=18) and hDN-PD (N=16) lines. **(e)** PCCs for correlating the hDN-PD template to bursts of hDN (N=18) and hDN-PD (N=16) lines. Pair-wise comparisons were carried out using the two-tailed Wilcoxon rank-sum test. The black stars indicate p values: * $p < 0.05$, ** $p < 0.01$, *** $p < 0.001$, **** $p < 0.0001$.

3.3.5 Axonal action potential propagation in healthy and diseased human iPSC-derived neurons

The HD-MEA chip used in this work allows for reading out neuronal electrical activity at subcellular resolution[48–50]. Measurements of action potential propagation velocities and potential alterations can be used to functionally differentiate neuronal cell types[51], to study

axonal development[52,53] and to get indications of axon degeneration[54]. Here, exploiting the high spatiotemporal resolution of HD-MEAs, we determined action-potential propagation velocities by tracking the AP propagation in space and time simultaneously across multiple electrodes (**Figure 5a-5c** and **Figure S3**). Action potentials are initiated at the AIS[49], which produces the largest extracellular voltage signal[49], and then propagate along the axon, while AP amplitudes decrease (Figure 5b).

To test if axonal-action-potential-propagation velocities differed between healthy and diseased cell lines, we estimated (see Methods, *Action Potential Propagation Velocity*) the respective velocities of healthy motor neurons and ALS motor neurons and over several DIVs (14, 28 and 42). Results showed differences in velocities during more mature stages, i.e., at DIV 42 (Figure 5d). At DIV 42, hMNs featured an average velocity of 480 ± 190 mm/s, while hMN-ALS neurons featured a significantly higher average axonal AP-propagation velocity of 560 ± 200 mm/s ($p < 0.01$, Wilcoxon rank-sum test).

The same measurements were conducted for healthy dopaminergic neurons and PD dopaminergic neurons. However, in contrast to motor neurons, healthy and diseased dopaminergic neurons did not show any significant difference in axonal propagation velocity (hDNs: 230 ± 80 mm/s, hDN-PDs: 280 ± 120 mm/s at DIV 42). The hDN lines featured comparably small signal amplitudes, which yielded less neurons that could be identified in the recordings. Although the spike sorting parameters were adjusted to also include neurons with smaller amplitudes (see Methods, *Spike Sorting*), only few hDN neurons satisfied the propagation-velocity conditions described in Methods (*Action Potential Propagation Velocity*) and could be used to assess axonal propagation speeds.
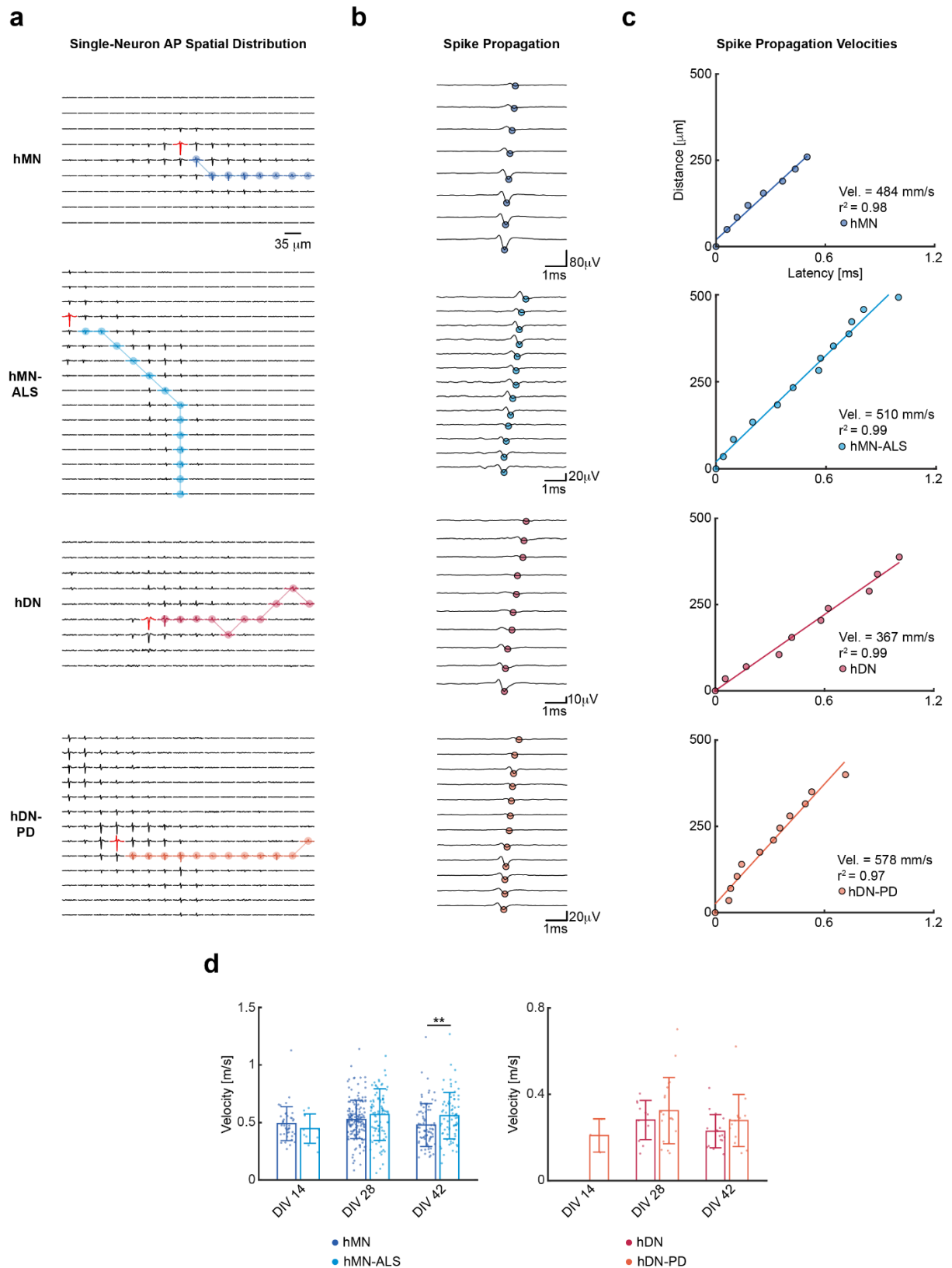
Figure 5. AP propagation velocity computed for different human iPSC-derived neuron lines. (a) Spatial distribution of action potential (AP) waveforms of sample neurons of (top to bottom) hMN, hMN-ALS, hDN, hDN-PD neuronal lines. Each trace represents a cutout of 6 ms of extracellular voltage signal recorded on the respective electrode at DIV 28. The red traces indicate the waveforms on the electrode featuring the largest signal amplitude. The plots are

also displayed in Figure S3 at larger magnification. **(b)** AP propagation in time and space, after temporal alignment of the signals of selected readout electrodes represented in (a). Points indicate the voltage minima of the recorded traces. The traces are ordered with respect to delay from top to bottom with the top trace featuring the longest delay and coming from the electrode that is most distant to the axonal initial segment (AIS). **(c)** Linear regression interpolation to compute the AP propagation velocity for the neurons represented in (a) and (b). **(d)** Bar plots comparing the AP propagation velocity of (left) healthy motor neurons and ALS motor neurons and of (right) healthy and PD dopaminergic neurons, at DIVs 14, 28 and 42. Each dot represents one HD-MEA or well. Bar heights indicate distribution mean values, and error bars indicate standard deviations. Pair-wise comparisons were carried out using the two-tailed Wilcoxon rank-sum test. The stars indicate p values: ** $p < 0.01$. The number (N) of hMNs for which velocities were determined at DIVs 14, 28 and 42 is 40, 165 and 80, respectively. The number (N) of hMN-ALSs for which velocities were determined at DIV 14, 28 and 42 is 11, 92 and 76, respectively. The number (N) of hDNs for which velocities were determined at DIVs 28 and 42 is 11 and 17, respectively. The number (N) of hDN-PDs for which velocities were determined at DIVs 14, 28 and 42 is 3, 19 and 14, respectively.

3.3.6 The effects of retigabine on spontaneous neuronal activity at network, single-cell and subcellular levels

Retigabine is an anticonvulsant drug used for epilepsy treatment. It opens neuronal K(v) 7.2-7.5 (formerly KCNQ2-5) voltage activated K(+) channels that generate the M-current, a subthreshold K(+) current needed to stabilize the membrane potential and control neuronal excitability[55]. The effects of retigabine dosage have been analyzed by monitoring neuron spiking rates using a 64-electrode MEA, which were found to significantly decrease[10,38,56]. Moreover, retigabine was also reported to decrease spontaneous electrical activity in neuronal cortical cultures by decreasing the mean burst rate[57]. Here, we explored the effects of retigabine on the inter-burst interval and number of active electrodes in cultures of healthy motor neurons at DIV14 (**Figure 6**), at DIV 21 (**Figure S4a**) and of diseased motor neurons at DIV 14 (Figure S4b). Additionally, we investigated how the spiking rate estimation may be influenced by the number of readout electrodes.

An analysis over the entire HD-MEA electrode array showed a significant reduction in the fraction of active electrodes one minute after applying concentrations 5 μM ($p < 0.017$, Kruskal-Wallis test, followed by Dunn-Sidák multiple-comparison test) and 10 μM ($p < 0.001$) (Figure 6a, 6b).

Using simultaneously 1'020 electrodes in the active regions, we assessed the number of spikes/min (see Methods, *Drug Administration*), which was reduced to $79 \pm 7\%$ upon applying a concentration of 1 μM, to $19 \pm 9\%$ upon applying concentrations of 5 μM ($p < 0.017$), and to $6 \pm 4\%$ using 10 μM ($p < 0.001$) (Figure 6f, left), compared to the baseline recordings without

retigabine treatment. This activity reduction was expected, as retigabine hyperpolarizes the cell membrane by opening potassium channels.

We also determined the mean inter-burst intervals, which increased 3.5-fold upon administration of 5 μM of retigabine (Figure 6c, 6d). The inter-burst interval also increased upon applying 10 μM retigabine, albeit the effect was more difficult to assess, as some HD-MEAs did not record any burst over the whole recording duration of 5 min.

Although retigabine caused significant changes in network firing properties and network bursting, retigabine doses of 1 μM and 5 μM did not significantly change the velocity of the propagating action potentials along axons (Figure 6e). Retigabine could potentially have altered AP propagation velocity along axons, as KCNQ channels are also present on dendrites and axon[58]. A very small decrease in conduction velocity was reported after retigabine administration in rat sciatic nerves[59,60].

We also studied the effects of retigabine dosage at a different day *in vitro* and conducted the same drug experiment on hMNs at DIV 21. Results are reported in Figure S4a. Dosage of 10 μM retigabine decreased the spikes/min to 30 ± 15 % (p < 0.017) and the pAE to 42 ± 17 % (p < 0.001). Despite a trend similar to the results at DIV 14, retigabine dosage had less effects on the measured metrics, and the data variation was higher.

Moreover, we tested if retigabine also decreased spontaneous electrical activity in the isogenic diseased line hMN-ALS at DIV14. Results are shown in Figure S4b. Dosage of 10 μM retigabine decreased the spikes/min to 12 ± 7 % (p < 0.001) and the pAE to 17 ± 10 % (p < 0.001). The overall decrease in spontaneous activity of the diseased cells, however, was lower than that observed with healthy hMNs.

In a next step, we tested the influence of the number and configuration of used electrodes on the obtained spiking and IBI. In addition to the standard configuration comprising the 1'020 most active electrodes at a minimum pitch of 35 μm, we used configurations of 64 electrodes (grids of 8×8 electrodes at 200 μm pitch) and 16 electrodes (4×4 grid at 200 μm pitch), see also **Figure S5a**. By using the 64-electrode configuration, we found similar relative changes in spikes/min for concentrations of 5 μM (p < 0.017) and 10 μM (p < 0.017), however, we noticed an increased variation of this metric across different cultures, as the number of spikes became very low upon dosage of larger concentrations of retigabine and some electrode configurations could not detect any spike (Figure 6f, center). Using 16-electrode configurations, arranged in a 4×4 grid, we obtained significant differences just between the control sample and 10 μM retigabine dosage (p < 0.017) (Figure 6f, right), as the scattering of

the measured values was comparably large. Also in this case, some electrode configurations could not detect spikes at higher drug concentrations. As can be expected, a larger number of recording electrodes or sampling points provides more reliable results.

To compare the variability in the measurement data and to see in how far local effects may influence the results, we applied 6 different configurations of 8×8 and 4×4 electrodes across 4 HD-MEAs for control and 1 μM concentration and 5 HD-MEAs for 5 μM and 10 μM concentrations (Figure S5b, S5c). For the metric spikes/min, we could confirm a higher well-to-well variability with respect to the configuration with 1'020 electrodes (Figure S5b), while for the metric IBI, we could not find significant differences between vehicle control and any drug concentration for the 64-electrode and the 16-electrode configurations (Figure S5c).
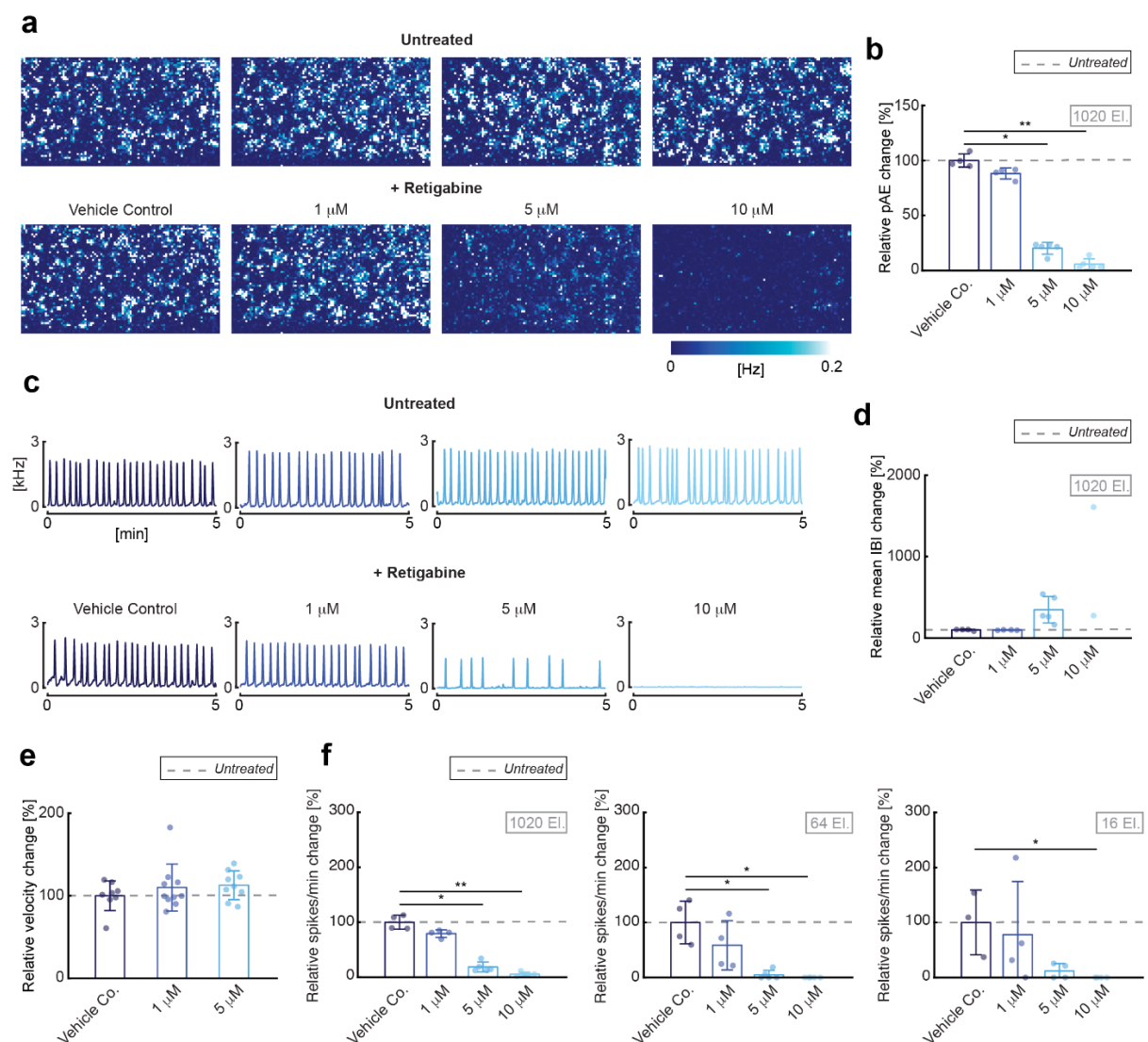

Figure 6. Retigabine effect on motor neurons on spikes/m, IBI and active electrodes. (a) 2D spatial distribution maps of electrode spike rates recorded from four exemplary HD-MEAs at DIV 14. Signals from 6'600 electrodes per HD-MEA were recorded before drug administration (top row) and one minute after drug administration (bottom row) for different

retigabine concentrations. **(b)** Bar plots representing the relative change (percent) in active electrodes for each applied retigabine concentration and for the vehicle control with respect to pre-treatment conditions. Each dot represents one HD-MEA or well. Bar heights indicate distribution mean values and error bars indicate standard deviations. The dashed gray line marks the values (100%) before drug treatment. The number of HD-MEAs or wells included N=4 for vehicle control and 1 µM retigabine concentration and N=5 for 5 µM and 10 µM retigabine concentrations. **(c)** Population spike time histograms of four representative HD-MEAs, recorded before (top row) and after drug administration (bottom row) for different retigabine concentrations. **(d)** Bar plots representing the relative change in the mean IBI for each applied retigabine concentration and for the vehicle control, normalized to pre-treatment conditions. **(e)** Bar plots representing the relative change in axonal velocity upon exposure to the vehicle control (N=8 neurons), 1 µM of retigabine (N=10 neurons) and 5 µM of retigabine (N=9 neurons), normalized to pre-treatment conditions. **(f)** Spikes/min-values computed as relative change with respect to the situation before drug administration. Plots show spikes/min-values for using signals from the 1'020 most active electrodes at a minimum pitch of 35, µm selected from the overall array of 26'400 electrodes (left), and configurations of 64 electrodes (center) and 16 electrodes at 200 µm pitch (right). For more details, see also Figure S5a. To compare multiple groups, we used the Kruskal-Wallis test, followed by the Dunn-Sidák multiple-comparison test. The individual pair-wise test was conducted at the Sidák-corrected α value of 0.017. The black stars indicate p values with respect to vehicle control: * $p < 0.017$, ** $p < 0.001$.

3.4   Discussion and Conclusion

We presented an investigation of the electrical phenotypes of several human iPSC-derived neuronal cell lines using HD-MEAs. We showed that HD-MEA technology - despite the low signal amplitudes of the hiPSC-derived neurons of approx. 30 µV to 45 µV - enables a reliable discrimination of the electrical activity of different neuronal lines at different developmental stages and across several levels, ranging from whole-network activity levels to subcellular structures. As more and more human iPSC-derived neuronal lines become available[61], the possibility to extract and compare a multiparametric set of physiological features across different functional levels will improve (i) the functional characterization of those neuronal lines in healthy and diseased states and (ii) the evaluation of drug effects upon administration *in vitro*.

As a first step, we characterized all cell lines by investigating metrics, such as mean firing rate (MFR), mean inter-spike interval (ISIcv), mean spike amplitude (MSA) and percentage of active electrodes (pAE) (Figure S1 and Figure 2). In a next step, we extracted features from network bursts of neuron cultures on MEAs, including burst structure, oscillatory behavior and synchronicity[62] (Figure 3 and 4). Finally, we characterized neuronal lines by investigating axonal propagation velocities (Figure 5). In contrast to passive MEA devices that feature fixed electrode configurations, CMOS-based HD-MEAs offer the possibility to extract all

aforementioned metrics from several active regions within a culture[23,63]. This feature enabled a reliable distinction of rPCNs from hDNs and hMNs based on the MFR, ISIcv, MSA, and pAE. (Figure S1 and Figure 2). Electrophysiological differences between rat primary cultures and human cell lines, especially for their firing rate, can possibly be explained by (i) the different neuronal maturation status[13], (ii) the different astrocyte maturation status[64], or/and (iii) the different astrocyte concentration[64], as has been reported by other authors.

As for healthy and diseased motor neurons, hyperexcitability was reported in iPSC-derived motor neurons harboring A4V SOD1 mutations[10] and C9ORF72 repeat expansions[65]. In studies with motor-neuron-like cell lines, transfected with mutant Q331K TDP-43, the authors found that the TDP-43 mutation increased the firing frequency of action potentials[66,67]. In our characterization of motor neuron electrical activity, we did not find a higher mean firing rate or mean spike amplitude in hMN-ALS neurons as compared to control hMNs (Figure 2). In contrast, we found that the hMN-ALS burst duration was 4.2-fold longer (16 sec) than that of control hMNs at DIV 21 (Figure 3).

As for healthy and diseased dopaminergic neurons, a higher network-bursting activity of A53T α-synuclein PD neurons, in comparison to a human control line, was reported by Zygogianni et al.[68], while other studies of network properties of PD neurons with mutations in the LRRK2 gene found that diseased neurons lacked synchronous network bursting activity[69]. Here, we found an increased frequency in synchronized population bursting activity for PD neurons, which is in agreement with the findings of Zygogianni et al.[68] (Figure 3). Furthermore, we found that PD neurons featured shorter burst duration and more variable inter-burst intervals compared to healthy dopaminergic neurons (Figure 3), which, again, is in agreement with the findings of Zygogianni [68].

Comparing the healthy and diseased lines by their AP propagation velocity, we found an increased axonal AP-conduction velocity in Q331K TDP-43 neurons (Figure 5), which could be correlated with altered axonal excitability properties reported in previous ALS studies[70,71]. Human motor-neuron lines feature larger AP spike amplitudes than dopaminergic-neuron lines, so that a more reliable extraction of axonal signals and differences in axonal propagation velocity between cell lines at different DIVs was possible. However, it is important to notice that the commercially available human iPSC-derived lines, used in this study, do not contain 100% motor neurons or 100% dopaminergic neurons (see Methods, *Cell Lines*) (Figure 1), so that caution is advised in the interpretation of the data. Moreover, it is important to mention that only one line of h-iPSC derived neurons was used in each study group and that donor-to-

donor differences, somatic mutations and experimental conditions greatly affect the electrophysiological properties of h-iPSC-derived neurons.

For a reliable comparison of subcellular features of genetically defined cell lines it is necessary to make sure that only neurons of the specified genetic type are characterized, which can be achieved by using the following experimental techniques or combinations thereof: (1) purification of neuronal lines by FACS sorting and subsequent plating[10]; (2) activation and identification of genetically-defined neurons in a mixed population by expression of opto- and chemogenetic markers, driven by cell-type-specific promoters[72]; (3) identification of cell types by extraction and classification of extracellular AP waveform features[73,74].

In a prototype drug dosage experiment, we evaluated the drug effects upon administration *in vitro* (Figure 6). We used retigabine, a potassium channel opener, which decreases neural activity. As expected, retigabine significantly decreased the percentage of active electrodes, the number of spikes per minute, and increased the inter-burst interval with increasing concentration (Figure 6). Experiments were performed at DIV 14, as cultures were stable and characterized by network synchronous activity. Additionally, we investigated the effect of retigabine at DIV 21 and recorded similar compound effects. However, retigabine dosage had less effects on the measured metrics at DIV 21, and the data variation was larger than at DIV 14.

We did not find significant changes in AP propagation velocity across axonal arbors upon increasing drug dose (Figure 6). Nevertheless, owing to the high spatial resolution of the HD-MEA, we could reliably monitor the same neurons and their axonal arbors before and after drug treatment, so that we propose to include this new metric in the assessment of compound effects. We found that the number and density of used electrodes strongly influence the nature and number of metrics that can be used to assess drug effects (Figure 6). In particular, the availability of a comparably large number of electrodes (1'020 electrodes simultaneously) enabled to capture the dynamics of multiple neurons, which increases the reliability of extracted metrics, such as recorded spikes/min. Additionally, our results showed that the use of a large number of flexible recording sites entailed a significantly lower intra-culture and culture-to-culture fluctuation as compared to applying fixed electrode configurations. By selecting readout electrodes, we could target areas, where active neurons were located, while fixed-grid arrangements do not offer this possibility. However, the results reported on here cannot be used to directly conclude on the performance of commercially available MEAs featuring less electrodes, as the electrode size also plays a role (averaging effect, see, e.g., reference[75]), which was not taken into account here.

In conclusion, HD-MEA technology enables to conduct non-invasive assays and to extract highly reproducible metrics, such as mean firing rate, mean spike amplitude and burst shape, for studying disease mechanisms at a functional level for a multitude of human neuronal lines[76]. In addition, HD-MEA technology provides accurate readouts at single-cell and subcellular levels, which can be used as complementary metrics for assessment of drug effects in human neuronal cultures[77].

3.5 Methods

3.5.1 High-Density Microelectrode Arrays

CMOS-based HD-MEAs[23,63] were used to record the extracellular signals of human iPSC-derived and rat primary neurons. The HD-MEA features 26'400 electrodes organized in a 120 $\times$ 220 grid within a total sensing area of 3.85×2.10 mm^2. The electrode area is 9.3×5.45 μm^2, and the center-to-center electrode distance (pitch) is 17.5 μm, which allows for recording of cell electrical activity at subcellular resolution. A user-selected configuration of 1'024 electrodes can be simultaneously recorded from (see also Methods, *HD-MEA Recordings*). The HD-MEA features noise values of 2.4 μV$_{rms}$ in the action potential band of 0.3 - 10 kHz and has a programmable gain of up to 78 dB. The sampling frequency is 20 kHz. We used the MaxOne HD-MEA produced by MaxWell Biosystems AG (www.mxwbio.com) and the laboratory version of the same HD-MEA[63], which only differs in the design of the printed circuit board (PCB).

3.5.2 Cell Lines

Human iPSC-derived neurons and astrocytes (iCell® DopaNeurons, iCell® Motor Neurons, iCell® DopaNeurons A53T, iCell® Motor Neurons Q331K, iCell® Astrocytes) were purchased from FCDI (FUJIFILM Cellular Dynamics International, Madison, USA). We used two dopaminergic-neuron cell lines: a mixed population of healthy A9 and A10 subtype human dopaminergic neurons (hDNs), which have been demonstrated to express relevant midbrain dopamine neuronal markers (see also Figure 1), and an isogenic variant harboring the early-onset mutation A53T α-synuclein (hDN-PD) as a disease line. The A53T α-synuclein mutation renders α-synuclein susceptible to aggregation, which has been proposed as contributor to PD pathology[78].

We used healthy human spinal motor neurons (hMNs) with expression of characteristic motor neuron markers (e.g. SMI-32), and an isogenic diseased motor neuron cell line carrying the TDP-43 Q331K mutation (hMN-ALS). Dominant mutations in the RNA/DNA-binding protein TDP-43 have been linked to amyotrophic lateral sclerosis (ALS)[79].

We used co-cultures of human motor neurons (hMN: 93% Tuj$^+$ / Nes^{--}, 93% Isl1/2^{+1} at 14dPT by flow cytometry) and astrocytes (98% CD44$^+$/S100β$^+$, 74% GFAP$^+$, 2% Tau$^+$, by flow cytometry) and co-cultures of human dopaminergic neurons (hDN: 92% Map2$^+$ / Nes, 81% FoxA2$^+$, 89% TH$^+$ by flow cytometry) and astrocytes at a ratio of 5:1. Astrocytes were added, as they support neuronal functioning in cultures, enhance the culture development[80] and mediate network synchronicity[81]. In particular, healthy astrocytes, co-cultured with healthy and diseased cell lines, help to achieve stable cultures and enable to correlate observed electrophysiological phenotypes to specific neuronal types.

Rat primary neurons were obtained from dissociated cortices of Wistar rats at embryonic day 18, using the protocol described in Ronchi et al., 2019[82]. All animal experimental protocols were approved by the Basel-Stadt veterinary office according to Swiss federal laws on animal welfare and were carried out in accordance with the approved guidelines.

3.5.3 Cell Plating

Prior to cell plating, HD-MEA chips were sterilized using 70% ethanol for 30 minutes. Ethanol was then removed, and the chips were rinsed three times with sterile tissue-culture-grade water. The HD-MEA chips were coated with chemicals to render the surface more hydrophilic. We adopted two different coating protocols suggested by the FCDI guidelines, depending on the cell type: for the motor-neuron plating, we treated the surface poly-D-lysine (PDL, 20 μL, 0.1 mg/mL) (A3890401, Gibco, ThermoFisher Scientific, Waltham, USA) for 1 hour at room temperature; for the dopaminergic-neuron plating, we used poly-L-ornithine (PLO, 20 μL, 0.05 mg/mL) solution (A-004-C, Sigma-Aldrich, St. Louis, USA) for 2 hours in a 5% CO_2 cell culture incubator at 37 °C. The PDL and PLO solutions were then aspirated, and the electrode surfaces were rinsed three times with sterile water.

On the plating day, extracellular-matrix-protein solutions were added to promote cell adhesion. Before plating the motor neurons, Geltrex extracellular-matrix solution (10 μL, 0.16 mg/mL) (A1569601, Gibco) was pipetted onto the array and left for 1 hour at room temperature. Before plating the dopaminergic neurons, Laminin solution (10 μL, 80 μg/mL) (L2020-1MG, Sigma-Aldrich) was pipetted onto the array for 30 minutes at 37 °C.

Frozen neuron and astrocyte vials were thawed for 3 minutes at 37 °C in a water bath, thereafter, 7 mL of medium was added to dilute the dimethyl sulfoxide (DMSO). The vials were then centrifuged for 5 minutes at 1600 rpm. Neurons and astrocytes were resuspended in medium to the desired ratio of 100'000 neurons and 20'000 astrocytes and then plated onto the HD-MEA chips in a 10 μL medium drop. The cells on the HD-MEA chips were incubated in a 5% CO_2 cell-culture incubator at 37°C for 1 hour. After cell adherence to the HD-MEA-chip surface, each well was filled with 0.6 mL of maintenance medium (see below). A 50% medium exchange was performed one day after plating, followed by 33% medium exchanges twice a week.

Maintenance medium consisted of Brainphys (05790, STEMCELL Technologies, Vancouver, Canada), supplemented with 2% iCell neural supplement (type B for dopaminergic neurons, type A for motor neurons) (FCDI), 1% iCell nervous-system supplement (FCDI), 1% of 100X N-2 supplement (17502048, Gibco), 0.1% laminin (L2020-1MG, Sigma-Aldrich) and 1% of 100X penicillin-streptomycin (15140122, Gibco).

During the first week *in vitro*, motor-neuron medium was supplemented with 5 μM DAPT (D5942, Sigma-Aldrich) to prevent outgrowth of proliferative cells.

E18 rat primary cortical neurons were isolated, plated and maintained according to protocols described previously[82].

3.5.4 HD-MEA Recordings

Recordings were performed weekly, starting from DIV 7. The recording setup was placed inside a 5% CO_2 cell-culture incubator at 37 °C, which entailed a stable pH-value of the cell culture medium. We used the "Activity Scan Assay" and "Network Assay" modules, featured in the MaxLab Live software (MaxWell Biosystems AG, Zurich, Switzerland), to monitor and record neuronal electrical activity. Seven electrode configurations, including a total of 6'600 electrodes at a pitch of 35 μm (every second electrode in x and y), were used to map spontaneous neuronal electrical activity across the entire HD-MEA chip. Each electrode configuration was recorded during 120 seconds ("Activity Scan Assay"). After scanning the entire HD-MEA, we selected 1'024 electrodes from the identified *active* electrodes and recorded network electrical activity for 300 seconds ("Network Assay"). Active electrodes were identified based on their firing rate, and among those the 1'024 electrodes featuring the highest firing rates were selected. The number of used HD-MEAs per condition (N) is always indicated in the figures in the Results section.

3.5.5 Data Analysis

Data analysis was performed using custom-written codes in MATLAB R2019a and Python 3.6.10.

HD-MEA Metrics

To characterize and compare the neuronal cultures, we used two categories of metrics: *electrode* metrics and *well* metrics. Metrics were first computed at electrode level. Then, the electrode metrics were averaged to represent a single HD-MEA chip or well. A *spike* was defined as a negative voltage deflection, whose amplitude exceeded 5 times the standard deviation of the baseline noise. Metrics indicated with asterisks (*) were adapted from Tukker et al., 2018[43] and Cotterill et al., 2016[46]. The following parameters and metrics were used to assess neuronal characteristics.

1. *Electrode firing rate (eFR)* was defined as the number of spikes n_i^{sp} observed in a pre-defined time interval *T*, recorded on a single electrode *i*:

$$eFR_i = \frac{n_i^{sp}}{T} \tag{1}$$

2. *Well mean firing rate* (MFR)* was defined as the mean of the eFR computed over the most active (electrodes with highest eFR) 1'024 electrodes ($N = 1'024$), simultaneously recorded:

$$MFR = \frac{1}{N} \sum_{i=1}^{N} eFR_i \tag{2}$$

3. *Electrode spike amplitude (eSA)* was defined as the 90th percentile of the recorded spike amplitudes on a single electrode *i*:

$$eSA_i = \frac{90}{100} \times M_i \tag{3}$$

where M_i is the length of the corresponding spike-amplitude vector, with amplitudes sorted from the smallest to the largest value.

4. *Well mean spike amplitude (MSA)* was defined as the mean of the eSA, computed over the most active 1'024 electrodes ($N = 1'024$), simultaneously recorded:

$$MSA = \frac{1}{N} \sum_{i=1}^{N} eSA_i \tag{4}$$

5. *Electrode inter-spike interval coefficient of variation (eISIcv)* was defined as the inter-spike interval (ISI) standard deviation, divided by the ISI mean (μISI), where the ISI is the time difference between two consecutive spikes times t_j, recorded on a single electrode *i*:

$$\mu ISI_i = \frac{1}{N_{sp}-1} \sum_{j=1}^{N_{sp}-1} \left(t_{j+1} - t_j \right) \tag{6}$$

$$eISIcv_i = \frac{\sqrt{\frac{1}{N_{sp}-1} \times \Sigma_{j=1}^{N_{sp}-1} \left| \left(t_{j+1} - t_j \right) - \mu ISI_i \right|^2}}{\mu ISI_i} \tag{7}$$

6. *Well inter-spike interval coefficient of variation* (ISIcv)* was defined as the mean of the *eISIcv*, computed over the most active 1'024 electrodes (N = 1'024), simultaneously recorded:

$$ISIcv = \frac{1}{N} \sum_{i=1}^{N} eISIcv_i \tag{8}$$

7. *Well percentage of active electrodes (pAE)* was defined as the percentage of electrodes with eFR > 0.1 Hz and eSA < −15 µV, per well. All electrode metrics described above (1-6) and all well metrics described below (8-11) were only computed for electrodes satisfying these two conditions for *active* electrodes (eFR > 0.1 Hz and eSA < −15 µV).

8. *Well mean burst duration* (BD)* was defined as the average duration of the network oscillations (bursts), recorded in a well:

$$BD = \frac{1}{N_b} \sum_{k=1}^{N_b} \left(t_{e,k} - t_{s,k} \right) \tag{9}$$

where N_b is the number of bursts, t_e represents the burst end point and t_s the burst starting point as illustrated in **Figure S6**. The fast Fourier transform (FFT) was used to compute the main oscillation frequency and to correct for false positives as a consequence of high oscillation frequencies within each burst.

9. *Well mean inter-burst interval* (IBI)* was defined as the average time between the starting points of consecutive network bursts per well:

$$IBI = \frac{1}{N_b-1} \sum_{k=1}^{N_b-1} \left(t_{s,k+1} - t_{s,k} \right) \tag{10}$$

10. *Well mean inter-burst interval coefficient of variation* (IBIcv)* was defined as the inter-burst interval standard deviation, divided by the inter-burst interval mean (*IBI*) per well:

$$IBIcv = \frac{\sqrt{\frac{1}{N_b-1} \times \Sigma_{k=1}^{N_b-1} \left| \left(t_{s,k+1} - t_{s,k} \right) - IBI \right|^2}}{IBI} \tag{11}$$

11. Well bursts/min* (B$_{/min}$) was defined as the average number of bursts per one-minute time interval:

$$B_{/min} = \frac{N_b}{t_m} \tag{12}$$

where t_m represents the total recording time in minutes.

12. *Well Pearson correlation coefficient (PCC)* was defined as the average linear correlation between the network bursts of a well and a network burst template representing a specific cell type:

$$PCC_k = \frac{1}{N_q - 1} \sum_{q=1}^{N_q} \left(\overline{\frac{b_q - \mu_b}{\sigma_b}} \right) \left(\frac{temp_q - \mu_{temp}}{\sigma_{temp}} \right) \tag{13}$$

$$PCC = \frac{1}{N_b - 1} \sum_{k=1}^{N_b - 1} PCC_k \tag{14}$$

where PCC_k represents the PCC between a single burst b (of mean μ_b and standard deviation σ_b) and a template *temp*, N_q the number of observations in the burst and *PCC* the mean of all PCC_k values computed in a specific well.

To characterize cell types according to their burst shape, eight templates were created, covering all cell types (hMN, hMN-ALS, hDN, hDN-PD) and each recorded DIV (14 and 21). The templates (*temp*) were obtained by averaging all recorded bursts in a well ($temp_w$) and across wells of the same cell type and DIV[83]:

$$temp_w = \frac{1}{N_b} \sum_{k=1}^{N_b} b_k, \quad temp = \frac{1}{N_w} \sum_{w=1}^{N_w} temp_w \tag{15}$$

where N_b is the number of bursts per well, b_k denotes a single burst in a well, and N_w is the total number of wells featuring a specific cell type and DIV.

Spike Sorting

Spike sorting was performed to identify single units in the extracellular recordings. We ran spike sorting on the recordings, with which we covered the entire chip area ("Activity Scan Assay") by using seven configurations of 960 electrodes (35 μm electrode pitch). We used the Kilosort2[84] software within the SpikeInterface[85] framework and the corresponding default parameters. Due to the large number of recordings, we automatically curated the spike sorting output according to the following criteria: for motor neurons, we removed clusters with less than 100 spikes, an ISI violation rate[86] above 0.3, and a signal-to-noise ratio (SNR) below 5; for dopaminergic neurons featuring less activity and lower signal amplitudes (Figure 3b), we

removed clusters with less than 50 spikes and an SNR below 3 (the threshold on ISI violation rate was the same). Automatic curation was performed using the SpikeInterface package[87].

Action Potential Propagation Velocity

Spike sorted and curated units were used to estimate the propagation velocity of action potentials. We discarded units with a *small spatial extension* template (averaged extracellular waveforms), and only kept units whose template covered at least 10 electrodes with an amplitude of more 10% of the maximum amplitude of the given unit. With these templates, we used a graph-based approach to find distinct neuronal branches. For each template, we considered the electrodes featuring a signal with an amplitude of at least 5% of the maximum amplitude and with a kurtosis value above 0.3 to filter out channels without a distinct signal peak. We then sorted the selected electrodes according to the time difference of the signal peak occurrence on that electrode with respect to the signal peak occurrence on the electrode showing the maximum signal amplitude, which most likely was close to the axon initial segment[49]. We then built a graph with the selected electrodes as *nodes* (**Figure S7**). Starting from the nodes with latest peak occurrence times (largest time difference)[88], each node was connected with *edges* to the three nearest electrodes with an earlier peak time. These three electrodes then formed the next set of nodes from which the procedure continued. Once the graph with all edges and nodes was built, we looked for the shortest paths along the nodes from each node to the electrode where the initial signal occurred, again starting from the electrodes with latest peak times or largest time differences. If an electrode formed already part of a path, it could not be used for another path. Finally, we removed duplicate paths by discarding the paths, where 50% of the nodes were in close proximity (<50 μm) to nodes of other paths. For the selected branches, distances were computed as the cumulative distance of all nodes between the initial electrode and the end of the path, while the peak times at the nodes included the differences between the peak time at the respective electrode and that at the initial electrode. Velocities were then estimated using a linear regression on the peak time differences and cumulative distances. We discarded branches with an $r^2<0.9$, and in cases that the algorithm found more than one branch for a template, we kept only the one with the highest r^2.

3.5.6 Statistical Analysis

Statistical comparisons between two populations were performed by using the non-parametric Wilcoxon rank sum test. Given two populations, the null hypothesis states that for randomly selected values A and B, drawn from each population, the probability of A being larger than B

is equal to the probability of B being larger than A. To compare samples from more than two populations, we used the Kruskal-Wallis H test. Its null hypothesis is that the distribution of the dependent variables is the same across the considered populations. In case the null hypothesis was rejected, we performed a post-hoc Dunn test with Sidák correction for multiple comparisons (Dunn-Sidák multiple-comparison test).

Statistical analysis was performed in MATLAB R2019a. Sample sizes and data presentation methods are indicated in the legends of each figure.

3.5.7 Drug Administration

Retigabine (90221, Sigma-Aldrich), dissolved in DMSO (D2650, Sigma-Aldrich) was applied at concentrations of 1 µM, 5 µM and 10 µM to a co-culture of healthy human motor neurons and astrocytes, similar to the experimental procedures reported by Wainger et al., 2014[10]. The vehicle control consisted of culture medium and DMSO (D2650, Sigma-Aldrich).

We performed recordings of motor neurons on each HD-MEA immediately before retigabine administration. We then conducted measurements one minute after drug administration. Data recorded after drug administration were normalized to data recorded before drug administration as (Parameter$_{exposure}$ / Parameter$_{baseline}$) $\times 100$[89]. Hereafter, the ratio was normalized in reference to the values obtained with vehicle control[89].

Drug effects were quantified about one minute after dosage by using the following metrics: spikes/min ($S_{/min}$), percentage of active electrodes (pAE) and mean inter-burst intervals ($IBIs$) (see Methods, *HD-MEA Metrics*).

The metric *spikes/min* (Figure 6b) for 1'024, 64 and 16 electrodes was computed as:

$$S_{/min} = \frac{n^{sp}}{t} \tag{16}$$

Where n^{sp} is the total number of spikes recorded from all the recording electrodes during the recording time t in minutes. The resulting metric value, obtained from a drug-treated HD-MEA chip, was then normalized to the corresponding metric value, obtained from an untreated HD-MEA chip, in order to obtain a relative metric change (percent change) induced by the addition of the compound.

3.5.8 Microscopy and Staining

Neurons on HD-MEAs were fixed using a 4% paraformaldehyde solution (FB001, ThermoFisher Scientific). Fixation prevented cell necrosis and autolysis and preserved the

cellular constituents. Samples were then permeabilized and blocked using a BPS 10× (AM9625, ThermoFisher Scientific) solution containing 10% normal donkey serum (NDS) (017-000-001, Jackson ImmunoResearch, West Grove, USA), 1% bovine serum albumin (BSA) (05482, Sigma-Aldrich), 0.02% Na-Az (S2002, Sigma-Aldrich) and 0.5% Triton X (93443, Sigma-Aldrich). Permeabilization facilitated antigen access to the cell, while blocking prevented non-specific binding of antibodies to the tissue. Primary and secondary antibodies were diluted in a PBS solution containing 3% NDS, 1% bovine serum albumin (BSA), 0.02% Na-Az and 0.5% Triton X[82]. The used antibodies are listed in Table 1.

We imaged cells on the HD-MEA chip with a Nikon NiE upright confocal microscope, with a Yokogawa W1 spinning-disk scan head.

Table 1. Antibodies. The table describes primary and secondary antibodies used in this work.

Antibody	Supplier	Ratio	Binds to	Catalogue #
Anti MAP2	EnCor	1:500	Microtubules	CPCA-MAP2
Anti TH	Pel Freeze	1:1000	Tyrosine hydroxylase enzyme	P60101-150
Anti GFAP	Abcam	1:500	GFAP	Ab7260
Anti S-100	Abcam	1:200	Zn	Ab52642
Anti Smi-32	Abcam	1:500	Neurofilaments	Ab7795
Hoechst	Thermofisher Scientific	1:500	DNA	H3570

3.6   Acknowledgements

3.7   Author contributions

S.R. contributed to the work design, performed and planned the experiments, analyzed and interpreted data, wrote the manuscript. A.P.B contributed to spike sorting data and velocity computation. G.P. contributed to perform experiments and to velocity computation. S.S.K. contributed to statistical analysis. M.S. contributed to writing the manuscript. M.F. coordinated and conceived the project, contributed to work design and data interpretation and wrote the manuscript. A.H. coordinated and conceived the project and contributed to writing the manuscript. All the authors have approved the submitted version and revised it.

3.8   Competing financial interests

The authors S.R., A.P.B., G.P, S.S.K., M.S. and A.H. declare no competing financial interests. M.F. is co-founder of MaxWell Biosystems AG, which commercializes HD-MEA technology.

3.9   References

[1]   K. Takahashi, S. Yamanaka, *Cell* **2006**, *126*, 663.

[2]   C. Liu, A. Oikonomopoulos, N. Sayed, J. C. Wu, *Development* **2018**, *145*, dev156166.

[3]   K. Si-Tayeb, F. K. Noto, M. Nagaoka, J. Li, M. A. Battle, C. Duris, P. E. North, S. Dalton, S. A. Duncan, *Hepatology* **2010**, *51*, 297.

[4]   H. Mou, R. Zhao, R. Sherwood, T. Ahfeldt, A. Lapey, J. Wain, L. Sicilian, K. Izvolsky, F. H. Lau, K. Musunuru, C. Cowan, J. Rajagopal, *Cell Stem Cell* **2012**, *10*, 385.

[5]   W.-Z. Zhu, B. Van Biber, M. A. Laflamme, **2011**, pp. 419–431.

[6]   I. Theka, M. Caiazzo, E. Dvoretskova, D. Leo, F. Ungaro, S. Curreli, F. Managò, M. T. Dell'Anno, G. Pezzoli, R. R. Gainetdinov, A. Dityatev, V. Broccoli, *Stem Cells Transl. Med.* **2013**, *2*, 473.

[7]   I.-H. Park, N. Arora, H. Huo, N. Maherali, T. Ahfeldt, A. Shimamura, M. W. Lensch, C. Cowan, K. Hochedlinger, G. Q. Daley, *Cell* **2008**, *134*, 877.

[8]   J. T. Dimos, K. T. Rodolfa, K. K. Niakan, L. M. Weisenthal, H. Mitsumoto, W. Chung, G. F. Croft, G. Saphier, R. Leibel, R. Goland, H. Wichterle, C. E. Henderson, K. Eggan, *Science (80-.).* **2008**, *321*, 1218.

[9]   A. H. Laperle, S. Sances, N. Yucer, V. J. Dardov, V. J. Garcia, R. Ho, A. N. Fulton, M. R. Jones, K. M. Roxas, P. Avalos, D. West, M. G. Banuelos, Z. Shu, R. Murali, N. T. Maidment, J. E. Van Eyk, M. Tagliati, C. N. Svendsen, *Nat. Med.* **2020**, *26*, 289.

[10]   B. J. Wainger, E. Kiskinis, C. Mellin, O. Wiskow, S. S. W. Han, J. Sandoe, N. P. Perez, L. A. Williams, S. Lee, G. Boulting, J. D. Berry, R. H. Brown, M. E. Cudkowicz, B. P. Bean, K. Eggan, C. J. Woolf, *Cell Rep.* **2014**, *7*, 1.

[11]   A. J. Schwab, A. D. Ebert, *Stem Cell Reports* **2015**, *5*, 1039.

[12]   C. Bardy, M. van den Hurk, B. Kakaradov, J. A. Erwin, B. N. Jaeger, R. V Hernandez, T. Eames, A. A. Paucar, M. Gorris, C. Marchand, R. Jappelli, J. Barron, A. K. Bryant, M. Kellogg, R. S. Lasken, B. P. F. Rutten, H. W. M. Steinbusch, G. W. Yeo, F. H. Gage, *Mol. Psychiatry* **2016**, *21*, 1573.

[13]   A. Odawara, H. Katoh, N. Matsuda, I. Suzuki, *Sci. Rep.* **2016**, *6*, 26181.

[14]   E. Flaherty, S. Zhu, N. Barretto, E. Cheng, P. J. M. Deans, M. B. Fernando, N. Schrode, N. Francoeur, A. Antoine, K. Alganem, M. Halpern, G. Deikus, H. Shah, M. Fitzgerald, I. Ladran, P. Gochman, J. Rapoport, N. M. Tsankova, R. McCullumsmith, G. E. Hoffman, R. Sebra, G. Fang, K. J. Brennand, *Nat. Genet.* **2019**, *51*, 1679.

[15]   C. M. Woodard, B. A. Campos, S.-H. Kuo, M. J. Nirenberg, M. W. Nestor, M. Zimmer, E. V. Mosharov, D. Sulzer, H. Zhou, D. Paull, L. Clark, E. E. Schadt, S. P. Sardi, L. Rubin, K. Eggan, M. Brock, S. Lipnick, M. Rao, S. Chang, A. Li, S. A. Noggle, *Cell Rep.* **2014**, *9*, 1173.

[16]   J. Pine, *J. Neurosci. Methods* **1980**, *2*, 19.

[17]   C. A. Thomas Jr, P. A. Springer, G. E. Loeb, Y. Berwald-Netter, L. M. Okun, *Exp. Cell Res.* **1972**, *74*, 61.

[18]   G. W. Gross, E. Rieske, G. W. Kreutzberg, A. Meyer, *Neurosci. Lett.* **1977**, *6*, 101.

[19]   B. Eversmann, M. Jenkner, F. Hofmann, C. Paulus, R. Brederlow, B. Holzapfl, P. Fromherz, M. Merz, M. Brenner, M. Schreiter, R. Gabl, K. Plehnert, M. Steinhauser, G. Eckstein, D. Schmitt-Landsiedel, R. Thewes, *IEEE J. Solid-State Circuits* **2003**, *38*, 2306.

[20]   L. Berdondini, K. Imfeld, A. Maccione, M. Tedesco, S. Neukom, M. Koudelka-Hep, S. Martinoia, *Lab Chip* **2009**, *9*, 2644.

[21]   G. Bertotti, D. Velychko, N. Dodel, S. Keil, D. Wolansky, B. Tillak, M. Schreiter, A.

Grall, P. Jesinger, S. Rohler, M. Eickenscheidt, A. Stett, A. Moller, K.-H. Boven, G. Zeck, R. Thewes, in *2014 IEEE Biomed. Circuits Syst. Conf. Proc.*, IEEE, **2014**, pp. 304–307.

[22] U. Frey, J. Sedivy, F. Heer, R. Pedron, M. Ballini, J. Mueller, D. Bakkum, S. Hafizovic, F. D. Faraci, F. Greve, K.-U. Kirstein, A. Hierlemann, *IEEE J. Solid-State Circuits* **2010**, *45*, 467.

[23] M. Ballini, J. Muller, P. Livi, Yihui Chen, U. Frey, A. Stettler, A. Shadmani, V. Viswam, I. Lloyd Jones, D. Jackel, M. Radivojevic, M. K. Lewandowska, Wei Gong, M. Fiscella, D. J. Bakkum, F. Heer, A. Hierlemann, *IEEE J. Solid-State Circuits* **2014**, *49*, 2705.

[24] V. Viswam, J. Dragas, A. Shadmani, Y. Chen, A. Stettler, J. Muller, A. Hierlemann, in *2016 IEEE Int. Solid-State Circuits Conf.*, IEEE, **2016**, pp. 394–396.

[25] H. Amin, A. Maccione, F. Marinaro, S. Zordan, T. Nieus, L. Berdondini, *Front. Neurosci.* **2016**, *10*, DOI 10.3389/fnins.2016.00121.

[26] H. Okano, D. Yasuda, K. Fujimori, S. Morimoto, S. Takahashi, *Trends Pharmacol. Sci.* **2020**, *41*, 99.

[27] K. Fujimori, M. Ishikawa, A. Otomo, N. Atsuta, R. Nakamura, T. Akiyama, S. Hadano, M. Aoki, H. Saya, G. Sobue, H. Okano, *Nat. Med.* **2018**, *24*, 1579.

[28] K. Imamura, Y. Izumi, A. Watanabe, K. Tsukita, K. Woltjen, T. Yamamoto, A. Hotta, T. Kondo, S. Kitaoka, A. Ohta, A. Tanaka, D. Watanabe, M. Morita, H. Takuma, A. Tamaoka, T. Kunath, S. Wray, H. Furuya, T. Era, K. Makioka, K. Okamoto, T. Fujisawa, H. Nishitoh, K. Homma, H. Ichijo, J.-P. Julien, N. Obata, M. Hosokawa, H. Akiyama, S. Kaneko, T. Ayaki, H. Ito, R. Kaji, R. Takahashi, S. Yamanaka, H. Inoue, *Sci. Transl. Med.* **2017**, *9*, eaaf3962.

[29] C. M. Woodard, B. A. Campos, S.-H. Kuo, M. J. Nirenberg, M. W. Nestor, M. Zimmer, E. V. Mosharov, D. Sulzer, H. Zhou, D. Paull, L. Clark, E. E. Schadt, S. P. Sardi, L. Rubin, K. Eggan, M. Brock, S. Lipnick, M. Rao, S. Chang, A. Li, S. A. Noggle, *Cell Rep.* **2014**, *9*, 1173.

[30] J. Benkert, S. Hess, S. Roy, D. Beccano-Kelly, N. Wiederspohn, J. Duda, C. Simons, K. Patil, A. Gaifullina, N. Mannal, E. Dragicevic, D. Spaich, S. Müller, J. Nemeth, H. Hollmann, N. Deuter, Y. Mousba, C. Kubisch, C. Poetschke, J. Striessnig, O. Pongs, T. Schneider, R. Wade-Martins, S. Patel, R. Parlato, T. Frank, P. Kloppenburg, B. Liss, *Nat. Commun.* **2019**, *10*, 5094.

[31] W. A. Rocca, *Lancet Neurol.* **2018**, *17*, 928.

[32] W. Poewe, K. Seppi, C. M. Tanner, G. M. Halliday, P. Brundin, J. Volkmann, A.-E. Schrag, A. E. Lang, *Nat. Rev. Dis. Prim.* **2017**, *3*, 17013.

[33] I. Prots, J. Grosch, R.-M. Brazdis, K. Simmnacher, V. Veber, S. Havlicek, C. Hannappel, F. Krach, M. Krumbiegel, O. Schütz, A. Reis, W. Wrasidlo, D. R. Galasko, T. W. Groemer, E. Masliah, U. Schlötzer-Schrehardt, W. Xiang, J. Winkler, B. Winner, *Proc. Natl. Acad. Sci.* **2018**, *115*, 7813.

[34] G. Kouroupi, E. Taoufik, I. S. Vlachos, K. Tsioras, N. Antoniou, F. Papastefanaki, D. Chroni-Tzartou, W. Wrasidlo, D. Bohl, D. Stellas, P. K. Politis, K. Vekrellis, D. Papadimitriou, L. Stefanis, P. Bregestovski, A. G. Hatzigeorgiou, E. Masliah, R. Matsas, *Proc. Natl. Acad. Sci.* **2017**, *114*, E3679.

[35] L. M. A. Oliveira, L. J. Falomir-Lockhart, M. G. Botelho, K.-H. Lin, P. Wales, J. C. Koch, E. Gerhardt, H. Taschenberger, T. F. Outeiro, P. Lingor, B. Schüle, D. J. Arndt-Jovin, T. M. Jovin, *Cell Death Dis.* **2015**, *6*, e1994.

[36] R. Mejzini, L. L. Flynn, I. L. Pitout, S. Fletcher, S. D. Wilton, P. A. Akkari, *Front. Neurosci.* **2019**, *13*, DOI 10.3389/fnins.2019.01310.

[37] E. Longinetti, F. Fang, *Curr. Opin. Neurol.* **2019**, *32*, 771.

[38] J. Lombardo, M. A. Harrington, *J. Neurophysiol.* **2016**, *116*, 2114.

[39] N. Egawa, S. Kitaoka, K. Tsukita, M. Naitoh, K. Takahashi, T. Yamamoto, F. Adachi, T. Kondo, K. Okita, I. Asaka, T. Aoi, A. Watanabe, Y. Yamada, A. Morizane, J. Takahashi, T. Ayaki, H. Ito, K. Yoshikawa, S. Yamawaki, S. Suzuki, D. Watanabe, H. Hioki, T. Kaneko, K. Makioka, K. Okamoto, H. Takuma, A. Tamaoka, K. Hasegawa, T. Nonaka, M. Hasegawa, A. Kawata, M. Yoshida, T. Nakahata, R. Takahashi, M. C. N. Marchetto, F. H. Gage, S. Yamanaka, H. Inoue, *Sci. Transl. Med.* **2012**, *4*, 145ra104.

[40] Z. Zhang, Z. Ma, W. Zou, H. Guo, M. Liu, Y. Ma, L. Zhang, *Biomed Res. Int.* **2019**, *2019*, 1.

[41] T. Hyvärinen, A. Hyysalo, F. E. Kapucu, L. Aarnos, A. Vinogradov, S. J. Eglen, L. Ylä-Outinen, S. Narkilahti, *Sci. Rep.* **2019**, *9*, 17125.

[42] P. J. Hallett, M. Deleidi, A. Astradsson, G. A. Smith, O. Cooper, T. M. Osborn, M. Sundberg, M. A. Moore, E. Perez-Torres, A.-L. Brownell, J. M. Schumacher, R. D. Spealman, O. Isacson, *Cell Stem Cell* **2015**, *16*, 269.

[43] A. M. Tukker, F. M. J. Wijnolts, A. de Groot, R. H. S. Westerink, *Neurotoxicology* **2018**, *67*, 215.

[44] D. J. Bakkum, M. Radivojevic, U. Frey, F. Franke, A. Hierlemann, H. Takahashi,

Front. Comput. Neurosci. **2014**, *7*, DOI 10.3389/fncom.2013.00193.

[45] M. Chiappalone, M. Bove, A. Vato, M. Tedesco, S. Martinoia, *Brain Res.* **2006**, *1093*, 41.

[46] E. Cotterill, D. Hall, K. Wallace, W. R. Mundy, S. J. Eglen, T. J. Shafer, *J. Biomol. Screen.* **2016**, *21*, 510.

[47] P. Görtz, M. Siebler, R. Ihl, U. Henning, C. Luckhaus, T. Supprian, C. Lange-Asschenfeldt, *Biochem. Biophys. Res. Commun.* **2013**, *434*, 293.

[48] D. J. Bakkum, U. Frey, M. Radivojevic, T. L. Russell, J. Müller, M. Fiscella, H. Takahashi, A. Hierlemann, *Nat. Commun.* **2013**, *4*, 2181.

[49] D. J. Bakkum, M. E. J. Obien, M. Radivojevic, D. Jäckel, U. Frey, H. Takahashi, A. Hierlemann, *Adv. Biosyst.* **2019**, *3*, 1800308.

[50] M. Radivojevic, F. Franke, M. Altermatt, J. Müller, A. Hierlemann, D. J. Bakkum, *Elife* **2017**, *6*, DOI 10.7554/eLife.30198.

[51] A. D. Sharma, L. McCoy, E. Jacobs, H. Willey, J. Q. Behn, H. Nguyen, B. Bolon, J. L. Curley, M. J. Moore, *Sci. Rep.* **2019**, *9*, 8921.

[52] B. J. Dworak, B. C. Wheeler, *Lab Chip* **2009**, *9*, 404.

[53] K. Shimba, K. Sakai, T. Isomura, K. Kotani, Y. Jimbo, *Integr. Biol.* **2015**, *7*, 64.

[54] M.-L. Campanari, A.-R. Bourefis, E. Kabashi, *Front. Neurol.* **2019**, *10,* DOI 10.3389/fneur.2019.00068.

[55] G. Blackburn-Munro, W. Dalby-Brown, N. R. Mirza, J. D. Mikkelsen, R. E. Blackburn-Munro, *CNS Drug Rev.* **2006**, *11*, 1.

[56] D. Moakley, J. Koh, J. D. Pereira, D. M. DuBreuil, A.-C. Devlin, E. Berezovski, K. Zhu, B. J. Wainger, *Sci. Rep.* **2019**, *9*, 10835.

[57] C. Wu, K. V. Gopal, T. J. Lukas, G. W. Gross, E. J. Moore, *Eur. J. Pharmacol.* **2014**, *732*, 68.

[58] M. J. Gunthorpe, C. H. Large, R. Sankar, *Epilepsia* **2012**, *53*, 412.

[59] J. J. Devaux, *J. Neurosci.* **2004**, *24*, 1236.

[60] C. Roza, J. A. Lopez-Garcia, *Pain* **2008**, *138*, 537.

[61] Y. Avior, I. Sagi, N. Benvenisty, *Nat. Rev. Mol. Cell Biol.* **2016**, *17*, 170.

[62] B. M. Bader, A. Steder, A. B. Klein, B. Frølund, O. H. U. Schroeder, A. A. Jensen, *PLoS One* **2017**, *12*, e0186147.

[63] J. Müller, M. Ballini, P. Livi, Y. Chen, M. Radivojevic, A. Shadmani, V. Viswam, I. L. Jones, M. Fiscella, R. Diggelmann, A. Stettler, U. Frey, D. J. Bakkum, A. Hierlemann, *Lab Chip* **2015**, *15*, 2767.

[64] A. Taga, R. Dastgheyb, C. Habela, J. Joseph, J. Richard, S. K. Gross, G. Lauria, G. Lee, N. Haughey, N. J. Maragakis, *Stem Cells Transl. Med.* **2019**, *8*, 1272.

[65] A.-C. Devlin, K. Burr, S. Borooah, J. D. Foster, E. M. Cleary, I. Geti, L. Vallier, C. E. Shaw, S. Chandran, G. B. Miles, *Nat. Commun.* **2015**, *6*, 5999.

[66] H. Dong, L. Xu, L. Wu, X. Wang, W. Duan, H. Li, C. Li, *Neuroscience* **2014**, *272*, 141.

[67] E. Buratti, **2015**, pp. 1–53.

[68] O. Zygogianni, N. Antoniou, M. Kalomoiri, G. Kouroupi, E. Taoufik, R. Matsas, *Neurochem. Res.* **2019**, *44*, 1475.

[69] L. Lin, J. Göke, E. Cukuroglu, M. R. Dranias, A. M. J. VanDongen, L. W. Stanton, *Cell Rep.* **2016**, *15*, 2411.

[70] K. Kanai, S. Kuwabara, S. Misawa, N. Tamura, K. Ogawara, M. Nakata, S. Sawai, T. Hattori, H. Bostock, *Brain* **2006**, *129*, 953.

[71] S. Vucic, M. C. Kiernan, *Clin. Neurophysiol.* **2006**, *117*, 1458.

[72] K. Berglund, J. K. Tung, B. Higashikubo, R. E. Gross, C. I. Moore, U. Hochgeschwender, **2016**, pp. 207–225.

[73] K. Weir, O. Blanquie, W. Kilb, H. J. Luhmann, A. Sinning, *Front. Cell. Neurosci.* **2015**, *8*, DOI 10.3389/fncel.2014.00460.

[74] A. P. Buccino, M. Kordovan, T. V. Ness, B. Merkt, P. D. Häfliger, M. Fyhn, G. Cauwenberghs, S. Rotter, G. T. Einevoll, *J. Neurophysiol.* **2018**, *120*, 1212.

[75] V. Viswam, M. E. J. Obien, F. Franke, U. Frey, A. Hierlemann, *Front. Neurosci.* **2019**, *13*, DOI 10.3389/fnins.2019.00385.

[76] C.-Y. Huang, C.-L. Liu, C.-Y. Ting, Y.-T. Chiu, Y.-C. Cheng, M. W. Nicholson, P. C. H. Hsieh, *J. Biomed. Sci.* **2019**, *26*, 87.

[77] L. Kramer, *ALTEX* **2020**, DOI 10.14573/altex.2001181.

[78] B. I. Giasson, J. E. Duda, S. M. Quinn, B. Zhang, J. Q. Trojanowski, V. M.-Y. Lee, *Neuron* **2002**, *34*, 521.

[79] J. Mitra, E. N. Guerrero, P. M. Hegde, N. F. Liachko, H. Wang, V. Vasquez, J. Gao, A. Pandey, J. P. Taylor, B. C. Kraemer, P. Wu, I. Boldogh, R. M. Garruto, S. Mitra, K. S. Rao, M. L. Hegde, *Proc. Natl. Acad. Sci.* **2019**, *116*, 4696.

[80] X. Tang, L. Zhou, A. M. Wagner, M. C. N. Marchetto, A. R. Muotri, F. H. Gage, G. Chen, *Stem Cell Res.* **2013**, *11*, 743.

[81] M. Amiri, N. Hosseinmardi, F. Bahrami, M. Janahmadi, *J. Comput. Neurosci.* **2013**, *34*, 489.

[82] S. Ronchi, M. Fiscella, C. Marchetti, V. Viswam, J. Müller, U. Frey, A. Hierlemann, *Front. Neurosci.* **2019**, *13*, DOI 10.3389/fnins.2019.00208.

[83] C. Orphanidou, T. Bonnici, P. Charlton, D. Clifton, D. Vallance, L. Tarassenko, *IEEE J. Biomed. Heal. Informatics* **2014**, *19*, 1.

[84] K. D. Pachitariu, M., Steinmetz, N., Kadir, S., Carandini, M. and Harris, *BioRxiv* **2016**.

[85] A. P. Buccino, C. L. Hurwitz, S. Garcia, J. Magland, J. H. Siegle, R. Hurwitz, M. H. Hennig, *Elife* **2020**, *9*, DOI 10.7554/eLife.61834.

[86] D. N. Hill, S. B. Mehta, D. Kleinfeld, *J. Neurosci.* **2011**, *31*, 8699.

[87] M. H. Buccino, A.P., Hurwitz, C.L., Magland, J., Garcia, S., Siegle, J.H., Hurwitz, R. and Hennig, *BioRxiv* **2019**.

[88] X. Yuan, M. Schröter, M. E. J. Obien, M. Fiscella, W. Gong, T. Kikuchi, A. Odawara, S. Noji, I. Suzuki, J. Takahashi, A. Hierlemann, U. Frey, *Nat. Commun.* **2020**, *11*, 4854.

[89] A. M. Tukker, L. M. S. Bouwman, R. G. D. M. van Kleef, H. S. Hendriks, J. Legler, R. H. S. Westerink, *Sci. Rep.* **2020**, *10*, 5311.

3.10 Supporting Information

Figure S1. Characterization of rat primary cortical neurons across development

To have a comparison for the electrical activity patterns of the human iPSC-derived neuronal lines, the developmental stage of which may greatly vary, and for the metrics described in the Methods section, we measured the electrical activity of rat primary cortical neurons (rPCNs), the most commonly used neuronal cells in the microelectrode-array field and an established *in-vitro* culturing system, across development. We plated rPCNs on 5 HD-MEAs, and we followed their development from DIV 7 to DIV 21.

The electrical activity of the rPCNs was assessed by recording spontaneous neuronal action potentials across the whole HD-MEA-chip active area and by then computing the following metrics: (1) mean firing rate (MFR), (2) mean spike amplitude (MSA), (3) mean inter-spike interval (ISI) coefficient of variation (ISIcv) and (4) percentage of active electrodes (pAE) (see Figure S1a, S1b and Methods, *HD-MEA Metrics*). rPCN cultures showed a 3.8-fold increase in the mean firing rate ($p < 0.025$, Kruskal-Wallis test, followed by Dunn-Sidák multiple-comparison test) from DIV 7 (0.54 ± 0.07 Hz) to DIV 21 (2.07 ± 0.99 Hz), as well as a 5.6-fold increase in the percentage of active electrodes ($p < 0.025$) from DIV 7 (8.6 ± 2.0 %) to DIV 21 (48.6 ± 15.7 %) (Figure S1c). The mean spike amplitude increased 1.5 fold from DIV 7 (64.9 ± 7.6 µV) to DIV 14 (95.7 ± 7.7 µV) and then stabilized between DIV 14 and DIV 21 (95.0 ± 9.0 µV) (Figure S1c). The mean ISI coefficient of variation increased 2.16 fold ($p < 0.025$) during culture development, with values of 1.53 ± 0.08 at DIV 7 and 3.31 ± 0.26 at DIV 21, which indicated that the firing rate in rat neurons became less regular during development (Figure S1c). Overall, rPCNs showed an increase in mean firing rate and percentage of active electrodes across development, as well as an increase in mean spike amplitude and irregularity of neuronal spiking (Figure S1c), as has been reported in other studies characterizing the electrical activity of neocortex neurons by MEA technology[46,73].
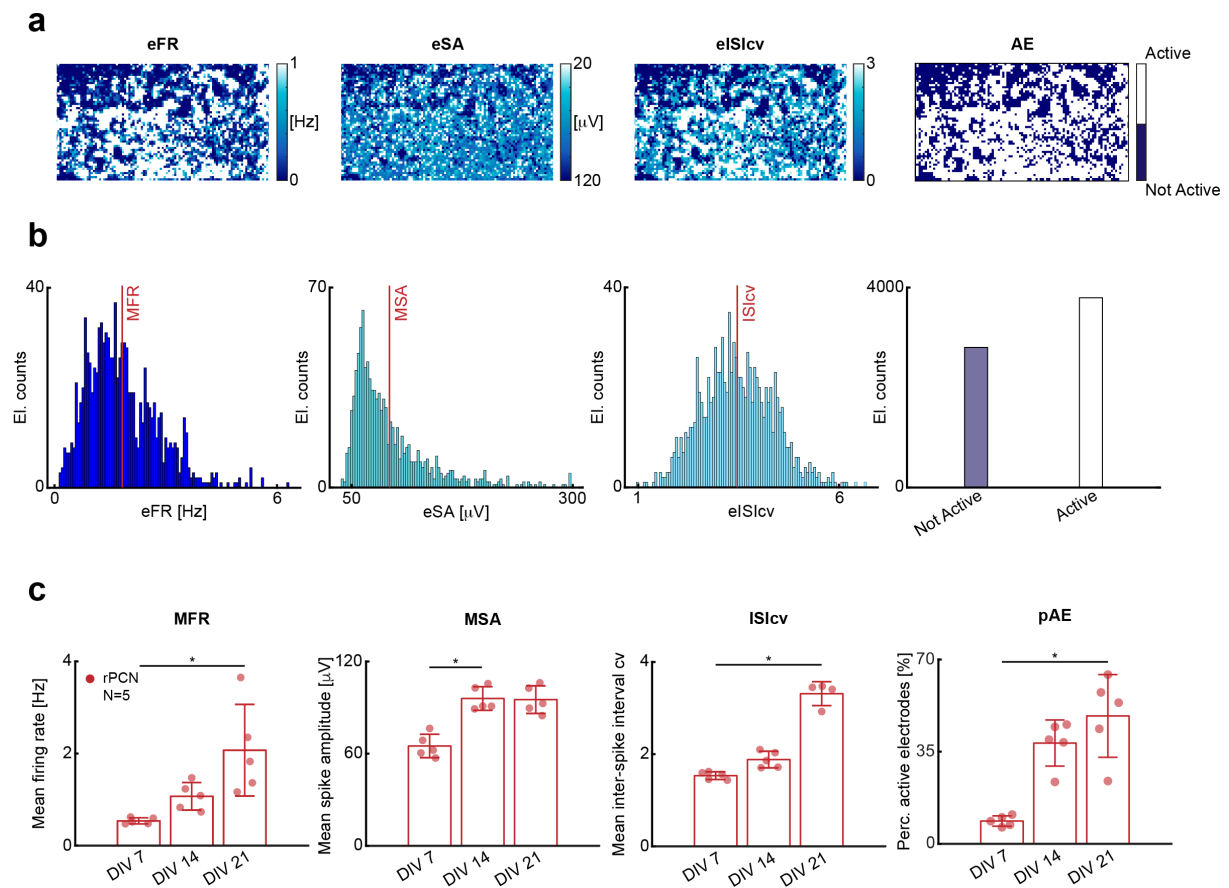
Figure S1. Electrical phenotype characterization of rat primary cortical neurons across development.

(a) Exemplary 2D spatial distribution maps of electrode firing rates (eFR), electrode spike amplitudes (eSA), electrode ISI coefficients of variation (eISIcv) and active electrodes across a total of 6'600 electrodes (see Methods, *HD-MEA Metrics*). The colors in each map represent the measured value of the given metric. The four maps have been acquired from one rPCN HD-MEA chip at DIV 21. **(b)** Exemplary distributions of metrics for one rPCN HD-MEA chip at DIV 21: first panel: distribution of eFRs; second panel, distribution of eSAs; third panel, distribution of eISIcvs; fourth panel, distribution of pAEs. Distribution means are indicated by red vertical lines. **(c)** Bar plots comparing mean firing rate (MFR), mean spike amplitude (MSA), mean ISI coefficient of variation (ISIcv) and percentage of active electrodes (pAE) of 5 different rPCN HD-MEAs (N = 5) at DIVs 7, 14 and 21 (see Methods, *HD-MEA Metrics*). Each red dot represents one HD-MEA or one well. The bar heights indicate the distribution mean values, and error bars indicate standard deviations. To compare multiple groups, we used the Kruskal-Wallis test, followed by the Dunn-Sidák multiple-comparison test. Data of DIV 7 were compared to those of DIV 14 and DIV 21. The individual pair-wise test was conducted at the Sidák-corrected a value of 0.025. The black stars indicate p values: * p < 0.025.
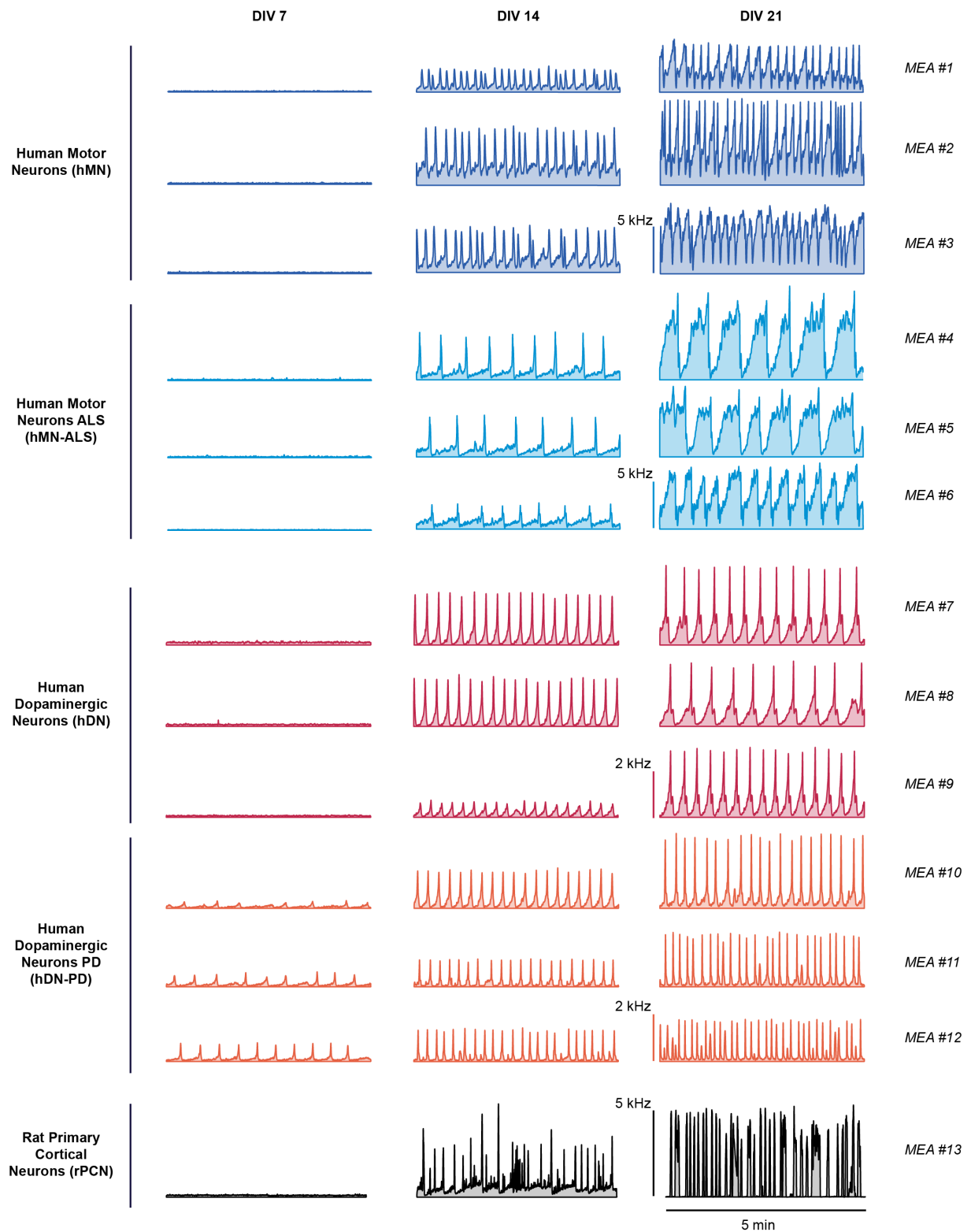
Figure S2. Burst reproducibility across samples and HD-MEAs.
Population spike time histograms simultaneously recorded from 1'024 electrodes of hMN (blue), hMN-ALS (light blue), hDN (red), hDN-PD (orange) and rPCN (black) cultures at DIVs 7 (first column), 14 (second column), 21 (third column). Bars at the left of the graphs in the third column indicate the spiking frequency.
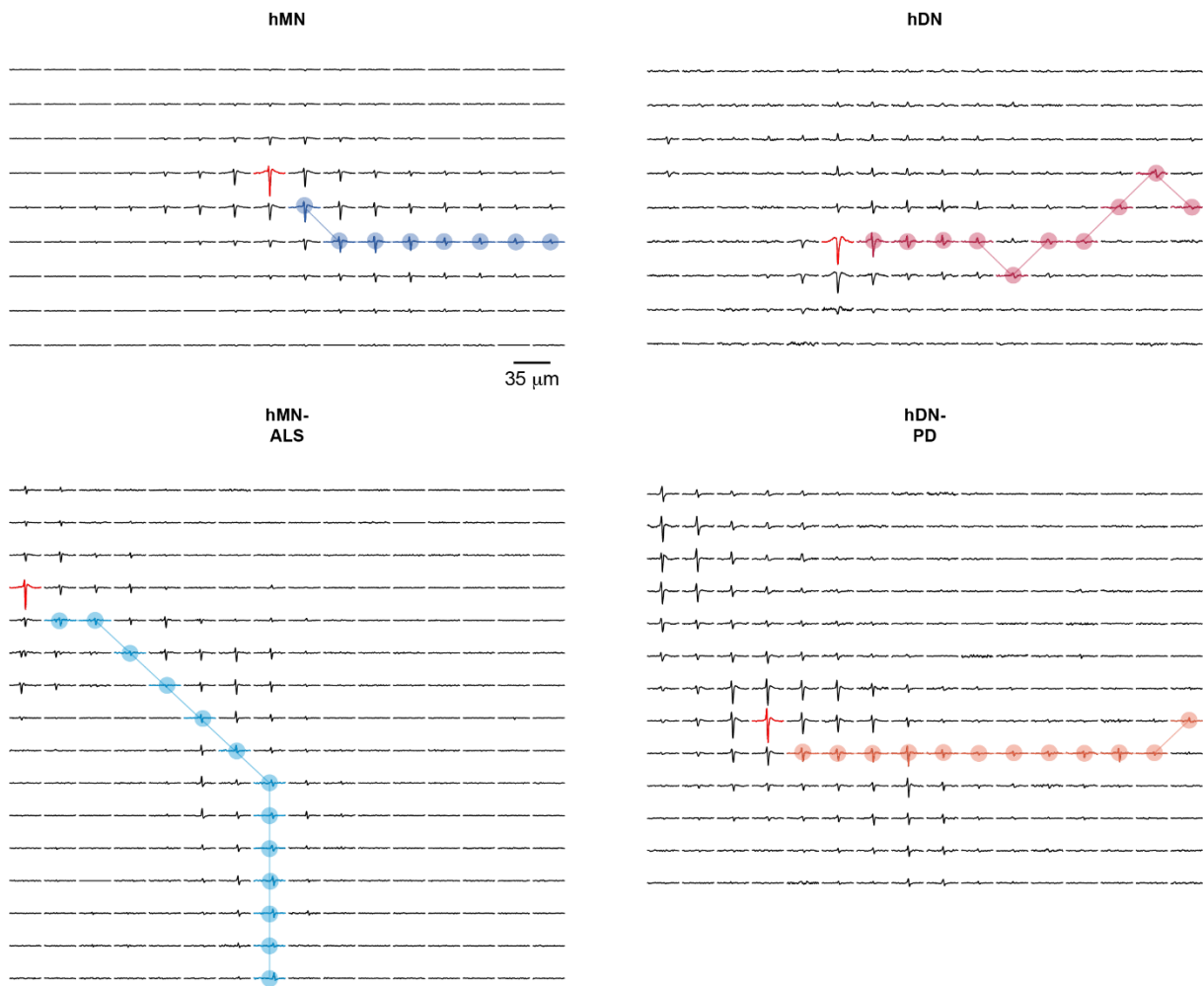
Figure S3. Single-neuron action potential spatial distributions.
Spatial distribution of action potential (AP) waveforms of sample neurons of hMN (top left), hMN-ALS (bottom left), hDN (top right), hDN-PD (bottom right) neuronal lines. Each trace represents a cutout of 6 ms of extracellular voltage signal, recorded on the respective electrode at DIV 28. The red traces indicate the waveforms on the electrode featuring the largest signal amplitude. The plots are identical with those in Figure 6a and are enlarged for better visibility.
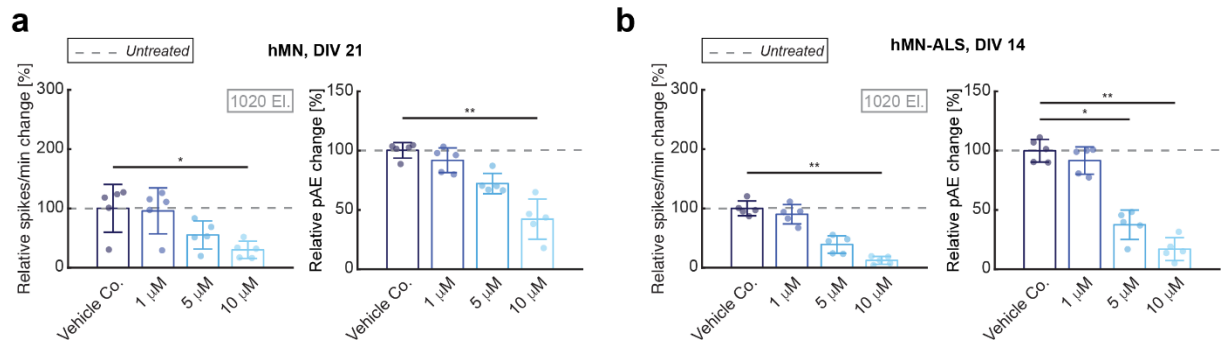
Figure S4. Retigabine dosage at different DIVs to healthy and diseased hMN lines. .
(**a**) Results of drug dosage to hMNs at DIV 21. Metrics Spikes/min (left) and pAE were used to assess the effects of retigabine upon dosage of concentrations of 1 μM, 5 μM and 10 μM. (**b**) Results of drug dosage to hMN-ALSs at DIV 14. Metrics Spikes/min (left) and pAE were used to assess the effects of retigabine upon dosage of concentrations of 1 μM, 5 μM and 10 μM. To compare multiple groups, we used the Kruskal-Wallis test, followed by the Dunne-Sidák multiple-comparison test. The individual pair-wise test was conducted at the Sidák-corrected a value of 0.017. The black stars indicate p values with respect to vehicle control: * p < 0.017, ** p < 0.001.
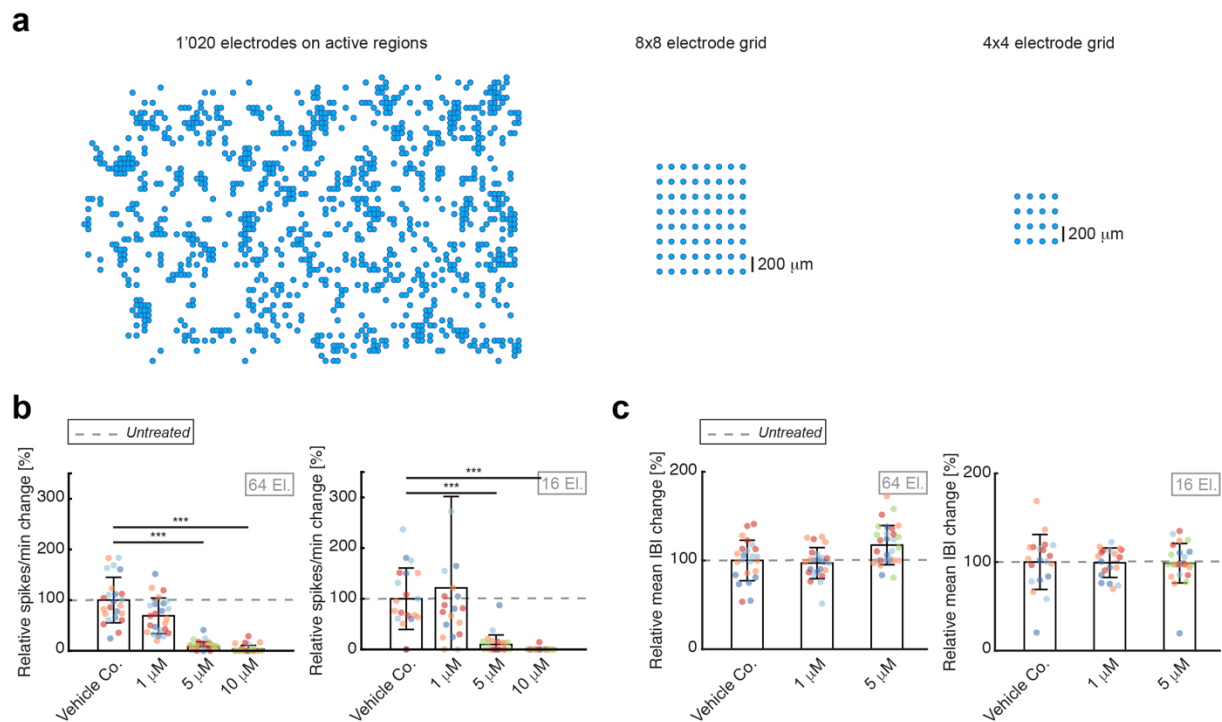
Figure S5. Retigabine well-to-well variability as a function of recording electrodes.
(a) Electrode configurations to assess retigabine effects described in Figure 6d and 6f. For the first configuration (left), 1'020 electrodes at a minimum pitch of 35 mm were selected from the active regions across the whole HD-MEA, i.e., the 1'020 electrodes recording the highest firing rates. We also used 8×8 (center) and 4×4 (right) electrode grid configurations with 200 mm electrode pitch. Each electrode configuration was measured before and after retigabine dosage to assess the drug effects. **(b)** Six different configurations of 8×8 and 4×4 electrodes were selected for each HD-MEA used for the drug dosage experiments (N = 4 HD-MEAs for vehicle control and 1 mM concentration, N = 5 HD-MEAs for 5 mM and 10 mM concentrations) and were used to assess variability of the spikes/min results, obtained with the fixed electrode configurations across a culture, with respect to variations from culture to culture and to see in how far local effects may influence the results obtained with those low-density configurations. The measurement points originating from low-density electrode configurations in the same culture are indicated in the same color. Bar plots represent the relative change in spikes/min upon exposure to vehicle control, 1 μM, 5 μM and 10 μM of retigabine, normalized to pre-treatment conditions. Bars indicate distribution mean values, and error bars indicate standard deviations. The dashed gray line marks the values (100%) before drug treatment. **(c)** The configurations displayed in panel (b) were used to assess variability of the IBI results obtained with the fixed electrode configurations across a culture with respect to variations from culture to culture. The measurement points originating from low-density electrode configurations in the same culture are indicated in the same color. Bar plots represent the relative change in mean IBI upon exposure to the vehicle control, 1 μM and 5 μM of retigabine, normalized to pre-treatment conditions.
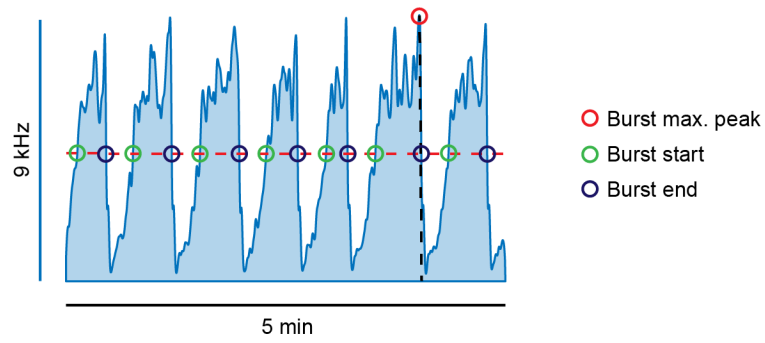
Figure S6. Burst duration computation.
Representative spike time histogram recorded by 1'020 electrodes. The burst duration was computed by fixing a threshold (dashed line) at 50% of the maximum burst amplitude (red). Start (green) and end points (blue) were placed at the intersection of spike time histogram and threshold.
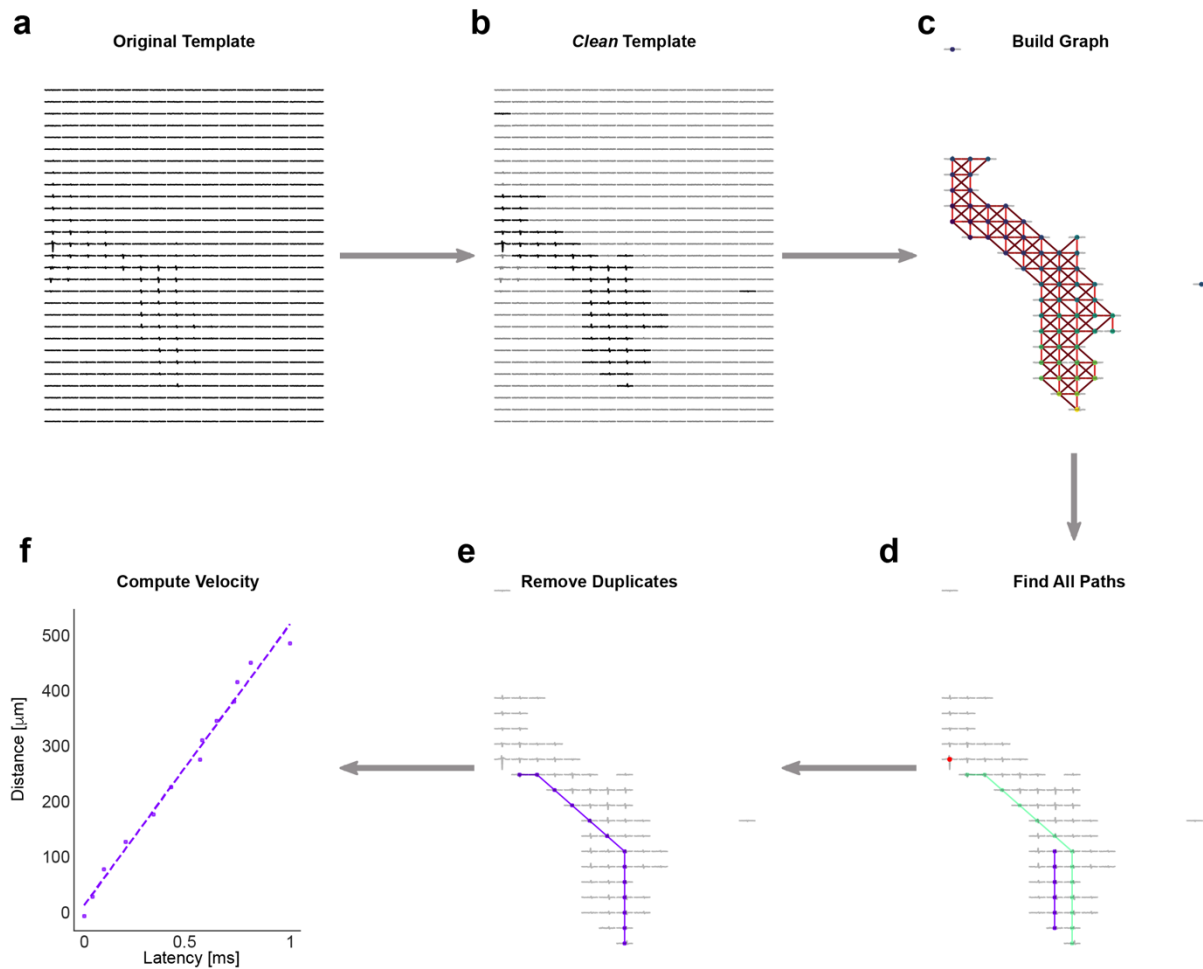
Figure S7. Axonal propagation velocity algorithm.
(a) Original template of a neuron obtained after spike sorting. **(b)** Selection of a subset of electrodes to obtain a "clean" template based on 3 criteria: (i) spike amplitude on a selected electrode > 5% of the maximum signal amplitude of the respective neuron; (ii) the signal kurtosis on a selected electrode > 0.3 (in order to filter out electrodes without a clear peak); and (iii) the peak time point of a selected electrode must occur after the peak time of the electrode with the highest amplitude (*initial electrode*). **(c)** The nodes of the graph correspond to the electrodes selected according to the procedure in (b). Starting from the nodes with latest peak occurrence times (largest time difference), each node was connected with edges to the three nearest electrodes with an earlier peak time within a distance of 50 μm. These three electrodes then formed the next set of nodes from which the procedure continued. If an electrode formed already part of a path, it could not be used for another path **(d-e)**. Duplicate paths removal by discarding the paths, where 50% of the nodes were in close proximity (<50 μm) to nodes of other paths. **(f)** Velocity estimation using a linear regression on the peak time differences and cumulative distances. Branches with an $r^2 < 0.9$ were discarded, and in cases that the algorithm found more than one branch for a template, only the one with the highest r^2 was kept.

4 TDP-43 PROTEINOPATHY IN HUMAN NEURAL NETWORKS EXPLORED AT THE SINGLE-CELL LEVEL

Manuscript in preparation in collaboration with the Polymenidou group of University of Zurich (UZH).

4.1 Introduction

Amyotrophic lateral sclerosis (ALS) is a progressive neurological disorder, characterized by the degeneration of both upper and lower motor neurons[1–3]. ALS is predominantly sporadic with approx. 90% to 95% of individuals developing a form of the disease with unknown causative mutations [4]. The other 5-10% of cases are caused by a mutation in one of the many ALS-associated genes and, thus, have a familial history with the disease[4]. ALS is characterized by a fast clinical progression, it starts with muscular degeneration, which results in paralysis and ultimately leads to death within 3-5 years since onset, most commonly due to respiratory problems[4]. TAR DNA-binding protein 43 (TDP-43) is a predominantly nuclear protein that plays an important role in RNA biogenesis, including pre-mRNA splicing, RNA transport and miRNA biogenesis[5]. While many mutations in TARDBP itself lead to familial ALS, cytoplasmic mislocalization, post-translational modification[3] (hyperphosphorylation, ubiquitination) and subsequent aggregation of TDP-43 in affected neurons have been identified as important features of both sporadic and familial ALS[5–9]. This results in the so-called TDP-43 proteinopathy, which can be found in approx. 97% of all ALS cases and other neurodegenerative diseases, such as frontotemporal dementia, LATE (late-predominant age-related TDP-43 encephalopathy) or as a concomitant pathology in Alzheimer's disease.

Human induced-pluripotent-stem-cell[10,11] (iPSC)-derived neurons and astrocytes have been used in the past years to evaluate ALS genetic factors[12] and exposure to compounds[4,13]. iPSC technology offers unprecedented possibilities to study neurodegenerative diseases *in vitro*, recapitulating aspects of the disease that are present in humans, but not in animal models.

Electrophysiology techniques have been employed to study iPSC maturation[14] and to characterize disease phenotypes. Recent studies on human iPSC-derived motor neurons[15] explored the electrophysiological effects of a mutation in the gene TARDBP, which encodes for the protein TDP-43. Results from voltage and current clamp analysis showed an initial neuronal hyperexcitability, followed by a loss in synaptic activity and generation of action potentials.

Similarly, all-optical electrophysiology studies on the ALS SOD1 mutation showed an increase in neuronal spontaneous activity[16]. Other researchers, making use of microelectrode arrays and patch clamp, demonstrated the hyperexcitability of motor neurons in the ALS SOD1 mutation and reduced it by dosing the potassium channel opener retigabine.

However, to the best of our knowledge, there is no precedent electrophysiology study, aimed at following the disease *in vitro* over time, which explores network, single-cell and subcellular electrophysiological parameters.

In this study, we used high-density microelectrode arrays (HD-MEAs)[17], *in-vitro* long-term and non-invasive platforms for high-resolution and high-content electrophysiology. We used HD-MEAs that feature 26'400 electrodes, placed at a center-to-center distance of 17.5 µm, and that allow for monitoring of entire neuronal networks as well as for recording electrophysiological features at subcellular resolution. We first characterized the maturation of neural-stem-cell (NSC)-derived neuronal networks, comparing the electrophysiology of NSCs differentiated during 2, 4 and 7 months at multiple time points. Using HD-MEAs, we detected differences between the different maturation stages at 2, 4 and 7 months, at network and subcellular levels.

To model TDP-43 pathology in our human neural networks, we transduced 2-months-old cultures with lentiviral vectors coding for inducible expression of human wild-type TDP-43 C-terminally tagged with an HA-tag (TDP-43-HA). TDP-43-HA expression was then induced, so that it would be expressed for 2 or 4 weeks when the transduced networks were 3 months old. At this point, the networks were dissociated into a single-cell suspension and processed for a) HD-MEA plating; b) single cell RNA sequencing (scRNAseq) and c) plated onto imaging plates for immunofluorescence assays. Our scRNAseq data demonstrated very high reproducibility with our previous single-cell sequencing of wild-type human neural networks, with cells clustering into neuronal and glial clusters. However, the mildly TDP-43-HA overexpressing neurons (total TDP-43 levels at 1.7x when compared to the non-transduced cells) ended up in a new and specific cluster (consisting of approx. 2% of total neurons), which allowed us to both, confirm the TDP-43-specific pathology, and to identify novel associated genes (data not shown). Both scRNAseq and IF showed that TDP43-HA+ neurons die over time and that this decay is associated with a spread of the pathology within the entire network as demonstrated by increasing number of TDP-43 p403+ neurons (data not shown). Using HD-MEAs, we functionally characterized the 2- and 4-weeks-transduced cultures (data not shown).

4.2   Methods

4.2.1 High-Density Microelectrode Arrays

CMOS-based HD-MEAs[17,18] were used to record the extracellular action potentials of human-derived neuronal networks and single neurons differentiated from neural stem cells. The HD-

MEA features 26'400 electrodes, organized in a 120×220 grid within a total sensing area of 3.85×2.10 mm^2. The electrode area is 9.3×5.45 μm^2, and the center-to-center electrode distance (pitch) is 17.5 μm, which allows for recording of cell electrical activity at subcellular resolution. Up to 1'024 electrodes can be simultaneously recorded from in user-selected configurations. The HD-MEA features noise values of 2.4 μV$_{rms}$ in the action-potential band of 0.3 - 10 kHz and has a programmable gain of up to 78 dB. The sampling frequency is 20 kHz.

4.2.2 Neural Stem Cell Differentiation

75000 cells/cm^2 NSCs were plated in NSC medium (see below) on 0.15 mg/ml Matrigel-coated (354234, Corning Inc., New York, USA) 6 well plates and left to recover and proliferate to reach ~95% confluency. NSC medium was switched to differentiation medium (see below), supplemented with 5 μM Forskolin (AG-CN2-0089-M050, Adipogen AG, Liestal, Switzerland), 1 μM synthetic retinoid Ec23 (AMS.SRP002-2, AMS Biotechnology Ltd, Abingdon, UK) and 500 nM Smoothened agonist SAG (5666600, Millipore, Merck, Darmstadt, Germany) for the first 5 days. On the days 6-10, Ec23 was increased to 2 μM. On days 11-25, Ec23 was decreased to 10ng/ml, SAG to 50nM and BDNF (450-02, PeproTech, London, UK), GDNF (450-10, PeproTech) and CNTF (C-240, Alomone labs, Jerusalem, Israel) were added at 20 ng/ml. From day 26 on, only BDNF, GDNF and CNTF were added. Medium was changed daily and completely for the first 10 days. Afterwards, only 2/3 of medium was changed 3 times a week.

NSC medium consisted of DMEM/F12 (21331046, Gibco, Thermo Fisher Scientific, Waltham, USA), supplemented with 0.5X B-27 supplement (12587-010, Gibco), 0.5X N-2 supplement (17502-048, Gibco), 1X GlutaMAX (35050-061, Gibco), 20 ng/ml bFGF (PHG0261, Gibco). Differentiation medium consisted of DMEM/F12 (11330032, Gibco), 0.5X B-27 supplement (17504-044, Gibco), 1X N-2 supplement (17502-048, Gibco), 1X GlutaMAX (35050-061, Gibco) and 1X Penicillin/Streptomycin (P4333-100ML, Sigma-Aldrich, Merck, Darmstadt, Germany).

4.2.3 HD-MEA Plating

HD-MEAs were sterilized for 40 minutes in 70% ethanol. HD-MEAs were washed three times with sterile deionized water (dH$_2$O) and then dried. After sterilization, HD-MEAs were coated with 20 μL of poly-D-lysine (P6407, Sigma-Aldrich) (diluted to 50 mg/mL in dH$_2$O) for 1 hour

at room temperature to render the surface more hydrophilic; each HD-MEA was then washed three times with sterile dH$_2$O and dried. Thereafter, HD-MEAs were coated with 10 μL Matrigel (354234, Corning Inc.), previously diluted in plating medium (see below) in a 1:10 ratio and incubated at 37°C for 2 hours.

Cells were centrifuged at 188 G-Force for 5 min, supernatant was aspirated, and plating medium was added to the cell pellet to reach the desired cell density (200'000 cells/HD-MEA). Matrigel was aspirated from HD-MEAs, and cells were plated in a 10 μL drop on the HD-MEAs. 0.9 mL of medium were added after 2-hour incubation at 37°C.

50% of plating medium was exchanged one day post plating and subsequently twice a week. Plating medium consisted of BrainPhys (05790, Stem Cell Technologies, Vancouver, Canada), supplemented with 2% B-27 Supplement (12587-010, Gibco), 1% N-2 Supplement (17502-048, Gibco), 1% Penicillin/Streptomycin (P4333-100ML, Sigma-Aldrich), 0.25% Glutamax (35050-061, Gibco), 20 ng/mL BNDF (450-02, PeproTech), 20 ng/mL GDNF (450-10, PeproTech), 20 ng/mL CNTF (C-240, Alomone labs), 20 ng/mL NT-3 (450-03, PeproTech), 10 μM cAMP (D0260, Sigma Aldrich), 20 ng/mL IGF-1 (78022, Stem Cell Technologies), 5 μM Forskolin (AG-CN2-0089-M050, Adipogen AG).

4.2.4 HD-MEA Recordings

The recording setup was placed inside a 5% CO$_2$ cell-culture incubator at 37 °C. Recordings were performed using the "Activity Scan Assay" and "Network Assay" modules, featured in the MaxLab Live software (MaxWell Biosystems AG, Zurich, Switzerland), as previously described[19]. The spontaneous neuronal activity across the whole HD-MEA was recorded using 6'600 electrodes in 7 electrode configurations at a pitch of 35 μm for 120 seconds. The most "active" 1'024 electrodes were then used to record network electrical activity for 300 seconds. Active electrodes were identified based on their firing rate, and, among those, the 1'024 electrodes featuring the highest firing rates were selected.

4.2.5 HD-MEA Metrics

We used metrics similar to those described in Section 3.5.5, *HD-MEA Metrics*, to characterize and compare the neuronal cultures; we used network, single-cell and subcellular-resolution metrics. As network metrics we used the burst duration (BD), inter-burst interval (IBI), inter-burst interval coefficient of variation (IBIcv), described in Ronchi et al., 2021[19]. As single-cell metrics we used the mean firing rate (MFR), mean spike amplitude (MSA), inter-spike

interval coefficient of variation (ISIcv)[19]. Additionally, we included the following extracellular waveform metrics, extracted from SpikeInterface[20], an open-source Python-based framework to enclose all the spike sorting steps:

1. Half width half maximum (HWHM), half width of trough of AP wave at half amplitude.
2. Peak trough ratio (PTr), ration of peak amplitude with respect to amplitude of trough.
3. Peak to valley (PtV), time interval between peak and valley.
4. Repolarization slope (RepS), slope between trough and return to baseline.
5. Recovery slope (RecS), slope after peak towards recovery to baseline.

As subcellular-resolution metrics, we extracted the action potential velocity (Vel), as described in Section 3.5.5, *Action potential propagation velocity*, and the branch length (BL).

The percentage of active electrodes (pAE) was also computed to measure the overall number of electrodes that could detect action potentials[19].

4.2.6 HD-MEA Data Analysis

Data analysis was performed using custom-written codes in MATLAB R2019a and Python 3.6.10.

Spike sorting was performed to identify single units in the extracellular recordings. We used the Kilosort2[21] software within the SpikeInterface[20] framework and the corresponding default parameters. We automatically curated the spike sorting output using the following parameters ([link](#)):

1. Inter-spike interval violation threshold (ISIt) = 0.5

The ISIt takes into account the refractory period, which follows every AP. The assumption is that if two APs occurs too close in time, they come from two different neurons.

2. Firing rate threshold (FRt) = 0.05

The FRt sets the minimum firing rate for a neuron to be considered as "good" unit.

3. Signal-to-noise ratio threshold (SNRt) = 5

The SNRt takes into account the ratio between the maximum amplitude of the mean AP waveform and the noise characteristics of the specific channel.

4. Amplitude cutoff (ACt) = 0.1

The ACt takes into account the false-negative rate, thus the fraction of spikes per unit with an amplitude below the detection threshold.

5. Nearest neighbors hit rate (NNt) = 0.9

After computing the principal component for a unit, the NNt is used to check on the fraction of the nearest neighbors that fall into the same cluster.

4.2.7 HD-MEA Statistical Analysis

Statistical comparisons to compare samples from more than two populations were performed using the Kruskal-Wallis H test. In case the null hypothesis was rejected, we performed a post-hoc Dunn test with Sidák correction for multiple comparisons (Dunn-Sidák multiple-comparison test).

Statistical analysis was performed in MATLAB R2019a.

4.3 Results

Several studies reported the use of human iPSC-derived neurons to analyze and model neurodegenerative diseases *in vitro*[15,22–25]. One of the major challenges of differentiating iPSCs into neurons is their maturation stage, as iPSC-derived neurons often resemble fetal neurons and lack mature synaptic markers[26]. Here, we used HD-MEAs to characterize the electrophysiology of NSCs, differentiated into mature neuronal networks for 2 (2mD), 4 (4mD) and 7 (7mD) months, respectively (**Figure 1a** and 1b). One month before recordings, we plated the differentiated neurons onto the HD-MEAs. Recordings were performed on the same day *in vitro* (DIV) for all conditions. At first, we compared the three different maturation stages by looking at the network properties. We analyzed the metrics burst duration (BD), inter-burst interval (IBI), IBI coefficient of variation (IBIcv) and bursts per minute (Bu/min). Results showed a significant decrease in BD between 2mD and 4mD (p=0.014) months and between 4mD and 7mD months (p=0.001) (Figure 1d and 1e). Interestingly, the IBIcv at 2 months was 1.5-fold more irregular than at 4 months. Some 2mD HD-MEAs could not be used for network analysis, as bursts were not detectable (Figure 1c-e). The percentage of active electrode (pAE) increased 2.25-fold between 4mD and 7mD (Figure 1d and 1e). Next, we compared the single-cell properties of the three different maturation stages after spike sorting of the data using the software Kilosort2 (see Methods 4.2.6). Results showed a lower firing rate (MFR) at 2mD with respect to 4mD and significant differences in the neuron branch length (BL) between 2mD and 4mD (p=0.02), suggesting a different maturation stage of the two conditions (Figure 1f-h).

After analyzing 15 HD-MEA metrics across scales, we have first evidence that the burst duration, the higher irregularity of inter-bust interval, the mean firing rate and the shorter branching may constitute potential indicators of the maturation stage.

a

— 4 mm

b

plating on HD-MEAs   recordings on HD-MEAs

7mD   4mD   2mD

differentiation time [months from plating]

-6   -3   -1   0   1

mature neuronal networks

c

2mD   4mD   7mD

firing rate [kHz]

channels

time [s]

d

Differentiation time

	2mD	7mD
BD	123.2	139.7
IBI	116.6	106.7
IBI cv	156.3	125.8
Bu/min	80.53	87.35
pAE	92.9	225.7

200
100 [%]
0

e

burst duration [s]

2mD   4mD   7mD

percentage active electrodes [%]

2mD   4mD   7mD

2mD
4mD
7mD

f

Differentiation time

	2mD	7mD
MSA	90.63	84.37
ISI cv	104.7	89.79
MFR	73.81	110.5
HWHM	100.7	106.7
PTr	103	109.1
PtV	94.19	98.34
RepS	91.56	85.47
RecS	96.52	91.88
Vel	93.41	97.14
BL	85.43	108.8

150
100 [%]
50

g

firing rate [Hz]

2mD   4mD   7mD

branch length [μm]

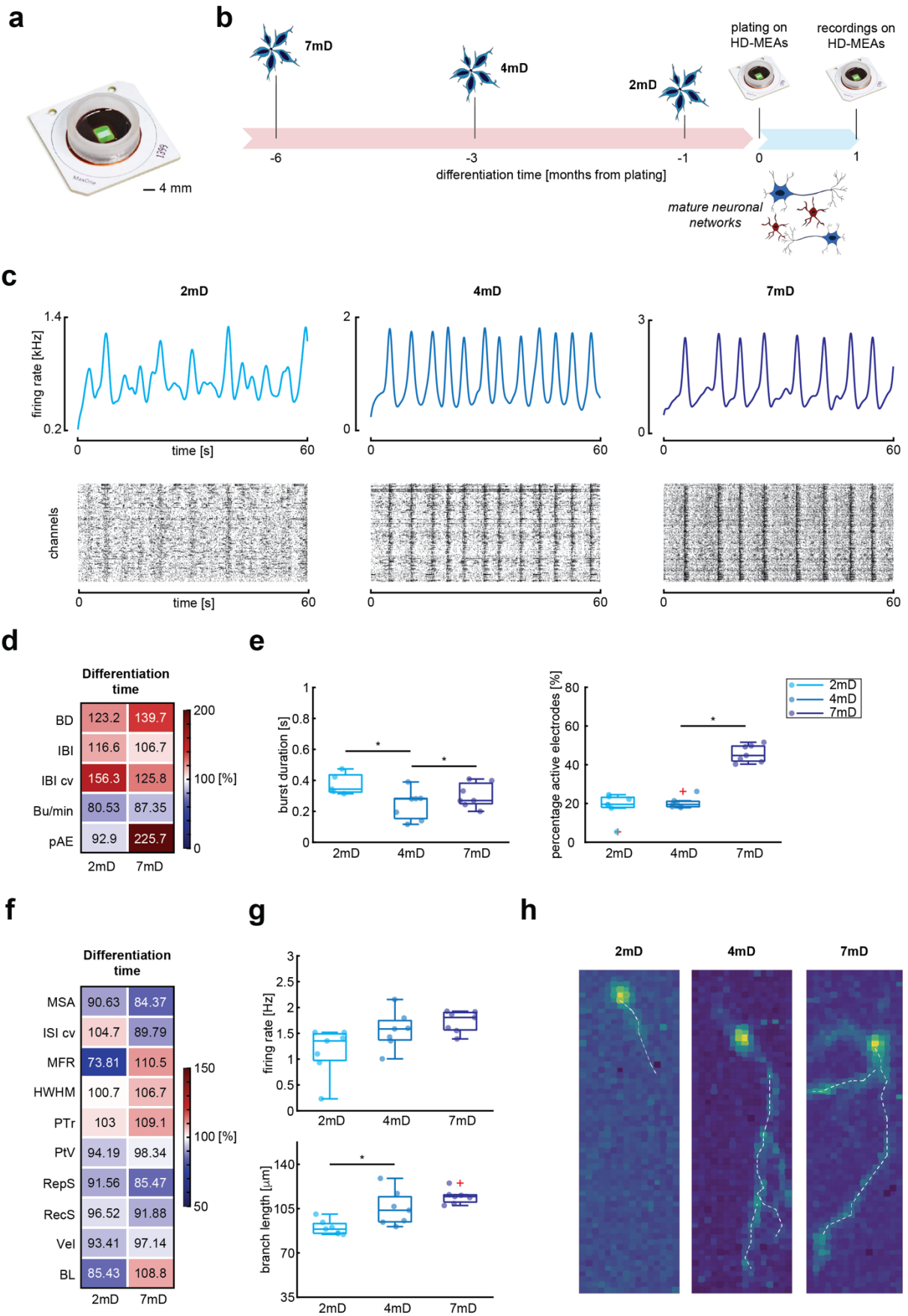2mD   4mD   7mD

h

2mD   4mD   7mD

Figure 1. Electrophysiological characterization of NSCs maturation stages. (a) HD-MEA used for electrophysiology recordings, with cell-culture chamber and electrode array in the center. **(b)** Timeline of experimental procedures. NSC were differentiated for 7, 4 and 2 months before recordings with HD-MEAs were conducted. Plating on HD-MEAs was performed 1 month before recordings. **(c)** (top) Population spike-time histograms simultaneously recorded by ~1000 electrodes from 2mD (left), 4mD (center) and 7mD (right) cultures. (Bottom) Raster plots represent the APs recorded from ~1000 electrodes simultaneously (y-axis) during one-minute recordings (x-axis) from 2mD (left), 4mD (center) and 7mD (right) cultures. Every black dot represents an AP. Vertical darker lines indicate a burst, which represents neuronal network synchronous activity. **(d)** Heatmap representing the % change of network metrics of 2mD and 7mD cultures with respect to metrics of 4mD cultures. **(e)** Box plots representing the burst duration (left) and % of active electrodes (right) of 2mD (left, N=5 for undetected BD and N=7 for pAE), 4mD (center, N=7) and 7mD (right, N=7) cultures. Each dot represents one HD-MEA. **(f)** Heat map representing the % change of single-cell and subcellular metrics of 2mD and 7mD cultures with respect to metrics of 4mD cultures. **(g)** Box plots representing the firing rate (top) and branch length (bottom) of 2mD (left, N=7), 4mD (center, N=7) and 7mD (right, N=7) cultures. Each dot represents one HD-MEA. **(h)** HD-MEA electrical image or «footprint» showing the 2D spatial distribution maps of the electrical activity of three neurons of 2mD (left), 4mD (center) and 7mD (right) cultures. To compare multiple groups, we used the Kruskal-Wallis test, followed by the Dunn-Sidák multiple-comparison test. The individual pair-wise test was conducted at the Sidák-corrected a value of 0.02. The black stars indicate p values with respect to 4mD: * $p < 0.02$.

4.4   References

[1]   E. B. Moloney, F. de Winter, J. Verhaagen, *Front. Neurosci.* **2014**, *8*, DOI 10.3389/fnins.2014.00252.

[2]   J. P. Taylor, R. H. Brown, D. W. Cleveland, *Nature* **2016**, *539*, 197.

[3]   R. H. Brown, A. Al-Chalabi, *N. Engl. J. Med.* **2017**, *377*, 162.

[4]   P. Clerc, S. Lipnick, C. Willett, *Drug Discov. Today* **2016**, *21*, 939.

[5]   E. L. Scotter, H.-J. Chen, C. E. Shaw, *Neurotherapeutics* **2015**, *12*, 352.

[6]   R. M. Liscic, L. T. Grinberg, J. Zidar, M. A. Gitcho, N. J. Cairns, *Eur. J. Neurol.* **2008**, *15*, 772.

[7]   L. K. Kwong, M. Neumann, D. M. Sampathu, V. M.-Y. Lee, J. Q. Trojanowski, *Acta Neuropathol.* **2007**, *114*, 63.

[8]   M. Neumann, L. K. Kwong, D. M. Sampathu, J. Q. Trojanowski, V. M.-Y. Lee, *Arch. Neurol.* **2007**, *64*, 1388.

[9]   A. C. McKee, B. E. Gavett, R. A. Stern, C. J. Nowinski, R. C. Cantu, N. W. Kowall, D. P. Perl, E. T. Hedley-Whyte, B. Price, C. Sullivan, P. Morin, H.-S. Lee, C. A. Kubilus, D. H. Daneshvar, M. Wulff, A. E. Budson, *J. Neuropathol. Exp. Neurol.* **2010**, *69*, 918.

[10]   K. Takahashi, S. Yamanaka, *Cell* **2006**, *126*, 663.

[11] Y. Shi, H. Inoue, J. C. Wu, S. Yamanaka, *Nat. Rev. Drug Discov.* **2017**, *16*, 115.

[12] W. Guo, L. Fumagalli, R. Prior, L. Van Den Bosch, *Front. Neurosci.* **2017**, *11*, DOI 10.3389/fnins.2017.00671.

[13] N. Egawa, S. Kitaoka, K. Tsukita, M. Naitoh, K. Takahashi, T. Yamamoto, F. Adachi, T. Kondo, K. Okita, I. Asaka, T. Aoi, A. Watanabe, Y. Yamada, A. Morizane, J. Takahashi, T. Ayaki, H. Ito, K. Yoshikawa, S. Yamawaki, S. Suzuki, D. Watanabe, H. Hioki, T. Kaneko, K. Makioka, K. Okamoto, H. Takuma, A. Tamaoka, K. Hasegawa, T. Nonaka, M. Hasegawa, A. Kawata, M. Yoshida, T. Nakahata, R. Takahashi, M. C. N. Marchetto, F. H. Gage, S. Yamanaka, H. Inoue, *Sci. Transl. Med.* **2012**, *4*, 145ra104.

[14] D. Prè, M. W. Nestor, A. A. Sproul, S. Jacob, P. Koppensteiner, V. Chinchalongporn, M. Zimmer, A. Yamamoto, S. A. Noggle, O. Arancio, *PLoS One* **2014**, *9*, e103418.

[15] A.-C. Devlin, K. Burr, S. Borooah, J. D. Foster, E. M. Cleary, I. Geti, L. Vallier, C. E. Shaw, S. Chandran, G. B. Miles, *Nat. Commun.* **2015**, *6*, 5999.

[16] E. Kiskinis, J. M. Kralj, P. Zou, E. N. Weinstein, H. Zhang, K. Tsioras, O. Wiskow, J. A. Ortega, K. Eggan, A. E. Cohen, *Stem Cell Reports* **2018**, *10*, 1991.

[17] M. Ballini, J. Muller, P. Livi, Yihui Chen, U. Frey, A. Stettler, A. Shadmani, V. Viswam, I. Lloyd Jones, D. Jackel, M. Radivojevic, M. K. Lewandowska, Wei Gong, M. Fiscella, D. J. Bakkum, F. Heer, A. Hierlemann, *IEEE J. Solid-State Circuits* **2014**, *49*, 2705.

[18] J. Müller, M. Ballini, P. Livi, Y. Chen, M. Radivojevic, A. Shadmani, V. Viswam, I. L. Jones, M. Fiscella, R. Diggelmann, A. Stettler, U. Frey, D. J. Bakkum, A. Hierlemann, *Lab Chip* **2015**, *15*, 2767.

[19] S. Ronchi, A. P. Buccino, G. Prack, S. S. Kumar, M. Schröter, M. Fiscella, A. Hierlemann, *Adv. Biol.* **2021**, 2000223.

[20] A. P. Buccino, C. L. Hurwitz, S. Garcia, J. Magland, J. H. Siegle, R. Hurwitz, M. H. Hennig, *Elife* **2020**, *9*, DOI 10.7554/eLife.61834.

[21] K. D. Pachitariu, M., Steinmetz, N., Kadir, S., Carandini, M. and Harris, *BioRxiv* **2016**.

[22] T. Kondo, M. Asai, K. Tsukita, Y. Kutoku, Y. Ohsawa, Y. Sunada, K. Imamura, N. Egawa, N. Yahata, K. Okita, K. Takahashi, I. Asaka, T. Aoi, A. Watanabe, K. Watanabe, C. Kadoya, R. Nakano, D. Watanabe, K. Maruyama, O. Hori, S. Hibino, T. Choshi, T. Nakahata, H. Hioki, T. Kaneko, M. Naitoh, K. Yoshikawa, S. Yamawaki, S. Suzuki, R. Hata, S. Ueno, T. Seki, K. Kobayashi, T. Toda, K. Murakami, K. Irie, W. L. Klein, H. Mori, T. Asada, R. Takahashi, N. Iwata, S. Yamanaka, H. Inoue, *Cell*

Stem Cell **2013**, *12*, 487.

[23] M. F. Burkhardt, F. J. Martinez, S. Wright, C. Ramos, D. Volfson, M. Mason, J. Garnes, V. Dang, J. Lievers, U. Shoukat-Mumtaz, R. Martinez, H. Gai, R. Blake, E. Vaisberg, M. Grskovic, C. Johnson, S. Irion, J. Bright, B. Cooper, L. Nguyen, I. Griswold-Prenner, A. Javaherian, *Mol. Cell. Neurosci.* **2013**, *56*, 355.

[24] A. di Domenico, G. Carola, C. Calatayud, M. Pons-Espinal, J. P. Muñoz, Y. Richaud-Patin, I. Fernandez-Carasa, M. Gut, A. Faella, J. Parameswaran, J. Soriano, I. Ferrer, E. Tolosa, A. Zorzano, A. M. Cuervo, A. Raya, A. Consiglio, *Stem Cell Reports* **2019**, *12*, 213.

[25] B. J. Wainger, E. Kiskinis, C. Mellin, O. Wiskow, S. S. W. Han, J. Sandoe, N. P. Perez, L. A. Williams, S. Lee, G. Boulting, J. D. Berry, R. H. Brown, M. E. Cudkowicz, B. P. Bean, K. Eggan, C. J. Woolf, *Cell Rep.* **2014**, *7*, 1.

[26] L. Qian, J. TCW, *Int. J. Mol. Sci.* **2021**, *22*, 1203.

5 CONCLUSIONS AND OUTLOOK

5.1 Conclusions

High-density microelectrode arrays enable to record the spontaneous activity of single neurons and entire neuronal network at high spatiotemporal resolution and for extended time periods. In this thesis we presented applications, which exploited the high resolution of the HD-MEAs to develop new high-content functional readouts.

5.1.1 Precise single-neuron electrical stimulation

Electrical stimulation[1,2] in voltage and current modes is typically used to modulate neuronal activity. For many *in-vivo* applications, like retina[3–8] or deep brain stimulation[9,10], stimulation precision is key to avoid unwanted side effects. A confined and precise electrical stimulation can be achieved by using the most efficient stimulation waveforms in terms of amplitude, waveform and overall stimulation time. Previous studies[5,11,12] included comparisons between stimulation waveforms in current and voltage mode to optimize stimulation efficacy and avoid the stimulation of neighboring neurons or nearby axon bundles. However, the used electrode arrays did not allow for subcellular-resolution stimulation and readouts.

In Chapter 2 we proposed stimulation protocols in both, current and voltage mode and explored multiple waveforms, durations and amplitudes; we targeted the AIS to ensure the highest stimulation efficacy. In voltage mode, we found that the monophasic cathodic and the biphasic anodic-cathodic waveforms were most efficient. In current mode, we found that the triphasic waveform was the most efficient one. Targeting of the AIS [13,14] allowed us to reach stimulation at unprecedented low injection of charges of a few picoCoulombs and with short pulses of few microseconds. Additionally, we could reliably read evoked APs through electrodes that were only a few micrometers away from the stimulation electrodes.

Furthermore, we tested the hypothesis that neuron stimulability is dependent on the AIS maturation and growth. Following single neurons across development, using optical microscopy techniques and HD-MEAs, we found a correlation between the AIS maturation and necessary stimulation amplitudes.

We showed that the selection of optimal stimulation parameters and locations is an effective means to ensure single-neuron stimulation and to reduce stimulation artifacts. *Ex vivo* applications (e.g., retinal preparations or brain slices) or *in vivo* applications (e.g., epiretinal

implants) will also benefit from parameter optimization and small electrode dimensions that help to reduce unwanted stimulation effects and enhance stimulation precision.

5.1.2 Functional phenotype characterization of healthy and diseased iPSC-derived neurons

Electrophysiology has been used to characterize iPSC-derived neurons[15], their maturation[16] and their phenotypes[17]. Differently from other electrophysiology techniques, HD-MEA technology allows for long-term, non-invasive and high-resolution recordings of spontaneous neuronal activity[18,19]. Using HD-MEAs, subcellular-resolution, single-cell, as well as neuronal-network metrics can be extracted, with the potential of improving functional characterization of healthy and diseased iPSC-derived neuronal lines.

In Chapter 3 we characterized and compared electrophysiological properties and functional phenotypes of human iPSC-derived neuronal lines (motor neurons and dopaminergic neurons) and related disease-model lines (Parkinson's disease and amyotrophic lateral sclerosis). Targeting the "highly active" regions within the cultures on the HD-MEAs, we could reliably find differences between healthy and diseased motor neurons with respect to metrics such as burst duration, inter-burst interval and axon velocity; this finding can be caused by an altered neuronal excitability of the diseased cell line[20,21]. Healthy and diseased dopaminergic neurons differed in metrics, such as mean firing rate, inter-burst interval and burst duration. Newly developed metrics for burst-shape and axon-velocity analysis were reliably used to distinguish the phenotypes of the cell lines.

We also exploited the HD-MEA high resolution to evaluate drug effects on human iPSC-derived neurons (Chapter 3). We used retigabine, which is a potassium channel opener and is known to decrease neural activity[17]. Retigabine decreased the percentage of active electrodes, the number of spikes per minute and increased the inter-burst interval, while it did not alter AP-propagation velocity. A last finding in Chapter 3 included that the number and density of recording electrodes may have a considerable influence on the reproducibility of the results when performing a drug experiment.

In Chapter 4, additional HD-MEAs metrics (e.g., branch length, repolarization slope, peak-trough ratio) were used to analyze different maturation stages of NSC-derived neuronal networks. We found that longer burst duration, higher irregularity of inter-bust interval, lower mean firing rage and shorter branch length are typical of cultures which are 2 months in

differentiation, with respect to cultures that are 4 months in differentiation. These metrics represent potential hallmarks of early maturation stages.

Chapter 3 and 4 show that HD-MEA technology provides reliable and reproducible results and can be used to perform high-content electrophysiology. Phenotyping and drug screening applications could benefit from previously inaccessible new metrics (e.g., axon velocity) or from the simultaneous characterization of network and single-cell features.

5.2   Outlook

Robust phenotypic and drug assays comprise of suitable (i) cell models, (ii) screening platforms and (iii) data analysis strategies. In this thesis, we mainly used human iPSC-derived neurons as a cell model. iPSCs have been proposed as a powerful system for drug discovery on different phenotypes[22] and they allow for discriminating between effective and non-effective drug treatments for different patients and pathologies. Using iPSC, neurological diseases are modelled using the patient's genetic background, which increases patient stratification and allows for studying sporadic occurrences of diseases and the disease development[22,23]. However, 2D culturing may affects many cellular functions in comparison to 3D systems. 3D culture systems, such as brain organoids, may represent a better model to recapitulate cellular interactions and microenvironments.

We used HD-MEAs as screening platform. HD-MEAs can be used to reliably detect small changes in neuron electrophysiology. Additionally, they allow for long-term and non-invasive monitoring of entire neuronal networks, which is different from imaging-based approaches that entail phototoxic effects. HD-MEAs also provide neuron-morphology and subcellular-electrophysiology information. However, the use of single wells strongly limits phenotypic or drug screening applications, where hundreds of wells are typically used simultaneously. The combination of HD-MEAs and multi-well approaches holds great potential for prediction of drug efficacy and toxicity, as it features all advantages offered by high-resolution techniques, while allowing for parallel screenings and decreased experimental times.

HD-MEA experiments have the drawback that they yield a large volume of data that are complex to analyze, which makes the interpretation of the results difficult. In this thesis, we performed large-scale data analysis using custom-made MATLAB and Python scripts. Machine-learning algorithms, instead, will introduce relationships between the collected data and possible predictions[24], which may simplify data analysis methodologies. Supervised machine learning makes use of *a priori* knowledge to train algorithms to recognize patterns in

unexplored datasets. Unsupervised machine learning, instead, can be used to create models based on patterns in recorded data, when the *a priori* knowledge is not available (e.g., screening of a new compound).

We envision that multi-well HD-MEAs hold the potential for reliable predictions of drug efficacy and toxicity, which, along with a suitable cell model system with broad patient stratification and machine-learning algorithms for fast data interpretation, could facilitate the development of drugs for neurological disorders and help the understanding of the corresponding mechanisms of action.

5.3   References

[1]   F. Rattay, *Neuroscience* **1999**, *89*, 335.

[2]   D. R. Merrill, M. Bikson, J. G. R. Jefferys, *J. Neurosci. Methods* **2005**, *141*, 171.

[3]   G. Dagnelie, *Curr. Opin. Neurol.* **2012**, *25*, 67.

[4]   D. Tsai, S. Chen, D. A. Protti, J. W. Morley, G. J. Suaning, N. H. Lovell, *PLoS One* **2012**, *7*, e53357.

[5]   L. E. Grosberg, K. Ganesan, G. A. Goetz, S. S. Madugula, N. Bhaskhar, V. Fan, P. Li, P. Hottowy, W. Dabrowski, A. Sher, A. M. Litke, S. Mitra, E. J. Chichilnisky, *J. Neurophysiol.* **2017**, *118*, 1457.

[6]   C. Sekirnjak, P. Hottowy, A. Sher, W. Dabrowski, A. M. Litke, E. J. Chichilnisky, *J. Neurosci.* **2008**, *28*, 4446.

[7]   V. H. Fan, L. E. Grosberg, S. S. Madugula, P. Hottowy, W. Dabrowski, A. Sher, A. M. Litke, E. Chichilnisky, *J. Neural Eng.* **2019**, *16*, 025001.

[8]   G. S. Brindley, W. S. Lewin, *J. Physiol.* **1968**, *196*, 479.

[9]   J. S. Perlmutter, J. W. Mink, *Annu. Rev. Neurosci.* **2006**, *29*, 229.

[10] A. L. Benabid, S. Chabardes, J. Mitrofanis, P. Pollak, *Lancet Neurol.* **2009**, *8*, 67.

[11] D. A. Wagenaar, J. Pine, S. M. Potter, *J. Neurosci. Methods* **2004**, *138*, 27.

[12] Y. Ahmadian, A. M. Packer, R. Yuste, L. Paninski, *J. Neurophysiol.* **2011**, *106*, 1038.

[13] M. Radivojevic, D. Jäckel, M. Altermatt, J. Müller, V. Viswam, A. Hierlemann, D. J. Bakkum, *Sci. Rep.* **2016**, *6*, 31332.

[14] D. J. Bakkum, M. E. J. Obien, M. Radivojevic, D. Jäckel, U. Frey, H. Takahashi, A. Hierlemann, *Adv. Biosyst.* **2018**, *1800308*, 1800308.

[15] H. Amin, A. Maccione, F. Marinaro, S. Zordan, T. Nieus, L. Berdondini, *Front. Neurosci.* **2016**, *10*, DOI 10.3389/fnins.2016.00121.

[16] D. Prè, M. W. Nestor, A. A. Sproul, S. Jacob, P. Koppensteiner, V. Chinchalongporn, M. Zimmer, A. Yamamoto, S. A. Noggle, O. Arancio, *PLoS One* **2014**, *9*, e103418.

[17] B. J. Wainger, E. Kiskinis, C. Mellin, O. Wiskow, S. S. W. Han, J. Sandoe, N. P. Perez, L. A. Williams, S. Lee, G. Boulting, J. D. Berry, R. H. Brown, M. E. Cudkowicz, B. P. Bean, K. Eggan, C. J. Woolf, *Cell Rep.* **2014**, *7*, 1.

[18] M. E. J. Obien, K. Deligkaris, T. Bullmann, D. J. Bakkum, U. Frey, *Front. Neurosci.* **2015**, *8*, 423.

[19] V. Emmenegger, M. E. J. Obien, F. Franke, A. Hierlemann, *Front. Cell. Neurosci.* **2019**, *13*, 1.

[20] K. Kanai, S. Kuwabara, S. Misawa, N. Tamura, K. Ogawara, M. Nakata, S. Sawai, T. Hattori, H. Bostock, *Brain* **2006**, *129*, 953.

[21] S. Vucic, M. C. Kiernan, *Clin. Neurophysiol.* **2006**, *117*, 1458.

[22] A. Farkhondeh, R. Li, K. Gorshkov, K. G. Chen, M. Might, S. Rodems, D. C. Lo, W. Zheng, *Drug Discov. Today* **2019**, *24*, 992.

[23] S. Pasteuning-Vuhman, R. de Jongh, A. Timmers, R. J. Pasterkamp, *Trends Mol. Med.* **2020**, DOI 10.1016/j.molmed.2020.09.013.

[24] S. Malandraki-Miller, P. R. Riley, *Drug Discov. Today* **2021**, DOI 10.1016/j.drudis.2021.01.013.